Doctoral Dissertations   Graduate School

12-2013

Processing, Structure, and Properties of Nanoparticle Reinforced Nonwoven Sandwich Composites

Josh Griffith Fogle
University of Tennessee - Knoxville, jfogle@utk.edu

Follow this and additional works at: https://trace.tennessee.edu/utk_graddiss

Part of the Polymer and Organic Materials Commons

Recommended Citation

To the Graduate Council:

I am submitting herewith a dissertation written by Josh Griffith Fogle entitled "Processing, Structure, and Properties of Nanoparticle Reinforced Nonwoven Sandwich Composites." I have examined the final electronic copy of this dissertation for form and content and recommend that it be accepted in partial fulfillment of the requirements for the degree of Doctor of Philosophy, with a major in Polymer Engineering.

Gajanan S. Bhat, Major Professor

We have read this dissertation and recommend its acceptance:

Roberto S. Benson, Kevin M. Kit, Jimmy W. Mays

Accepted for the Council:

<u>Carolyn R. Hodges</u>

Vice Provost and Dean of the Graduate School

(Original signatures are on file with official student records.)

Processing, Structure, and Properties of Nanoparticle Reinforced Nonwoven Sandwich Composites

A Dissertation Presented for the
Doctor of Philosophy
Degree
The University of Tennessee, Knoxville

Josh Griffith Fogle

December 2013

ACKNOWLEDGEMENTS

ABSTRACT

Shockwaves produced from ballistic impacts and improvised explosive devices are capable of causing severe internal trauma to soldiers. Current antiballistic materials give adequate protection to soldiers from high velocity impacts, however they are insufficient at absorbing and dissipating shockwave energy generated by these impacts and explosive blasts. The goal of this research was to develop shockwave absorbing protective materials which can be used as liners in conjunction with current antiballistic materials by reinforcing thermoplastic polyurethane nonwovens with high modulus nanoparticles.

To determine the appropriate TPU for the application, a series of TPUs of shore hardness ranging from 60D to 85A were melt blown to investigate processability, web structure, mechanical, and thermal properties. It was determined that a TPU of 90A shore hardness was most suitable and possessed a glass transition in the ideal range to exploit the transition from rubber to glass phase upon high velocity impact to allow for large amounts of energy dissipation. Nanoparticles investigated for reinforcement include: nanoclay, graphite, C60, POSS, and inorganic disulfide nanotubes. Methods used to incorporate the nanoparticles into the nonwoven web were: dip coating, ultrasonic spray coating, and melt blowing with compounded mixtures of polymer and nanoparticle blends. The loaded webs were fabricated into sandwiched nanocomposites to investigate the performance by dynamic, and high frequency testing.

The ultra-sonic spray coating method produced the most uniform dispersion of nanoparticles and greatest improvement in the dynamic mechanical properties of the reinforcement methods investigated. Of the multiple nanoparticles used for reinforcement, C60 provided the greatest improvement in damping ability. With optimized spray coating parameters, the storage and loss moduli of the C60 reinforced sandwich composite at 0.2% by weight loading were increased by 15 times over the control sample. The study showed that by proper selection of materials and processing, it is possible to develop materials for energy absorption at high strain rates.

TABLE OF CONTENTS

LIST OF TABLES

LIST OF FIGURES

CHAPTER 1: INTRODUCTION

1.1: Scope

The rise of fundamentalism in certain pockets of the world has been accompanied by an increase in encounters involving asymmetric threats. Defined as extended and unanticipated operations conducted by individuals, organizations, and nations specifically targeting weak and vulnerable sections within the enemy countries, the prevalence of asymmetric threats continues to rise. In the words of former Secretary of Defense William Cohen, asymmetric threats are a major component in warfare [1]. Vulnerable sections at risk during these threats often include logistics, maintenance, communication and supply units, health care professionals, etc., and any individuals involved in all of these areas are at high risks during a conflict [2]. An important consequence of the large number of improvised explosive devices (IEDs) soldiers are being confronted with is the subsequent increase in traumatic brain injuries. While personal protection gear has been greatly improved over the years, protection from shockwaves generated by IED explosions has never been a priority. However, with the increasing number of soldiers experiencing TBIs, it is clear much work must be done to understand the nature of the injury, how it occurs, and what can be done to prevent them [3].

Considering the United States' manpower, advanced weaponry, and modern technological capabilities, many weaker organizations and nations utilize asymmetric threats against the USA as their preferred form of combat. However, the threats of asymmetric weapons can be deterred through the implementation of a multifaceted strategy, which includes intelligence, data acquisition and analysis, and disruption of the asymmetric threat chain and technology through the utilization of protective gear, armored military vehicles, and hand held shields, etc. There are certain necessary requirements for protective gear in such situations. For example, usable materials must be light-weight, balanced, durable, cost-effective, and compatible with other equipment, comfortable, reusable, water repellent, moisture-vapor permeable, fire resistant, and

camouflage capable. The gear should also have a low heat stress, contain the ability to defeat projectiles, and have a longer service life.

Only a composite material can fulfill a multitude of properties. Currently, much of the military protective gear is fabricated from composite materials based off very strong yet stiff and brittle fibers [4]. These materials perform well at preventing penetration of projectiles, however they are inefficient at absorbing and dissipating the remaining projectile energy and shockwaves generated from explosions. A different material is required to absorb and dissipate this type of energy. Thermoplastic elastomeric composites are a rapidly growing field of advanced materials. Composites comprised of reinforcing nanofillers embedded in a matrix of thermoplastic elastic polymers offer high specific strength, stiffness and low density. Reinforced composite materials can play an important role in military applications and provide materials with very high strength, impact resistance, and energy dissipation. To achieve diverse properties in the gear, a prudent selection of nanofillers, polymers for the matrix, and soft and hard laminates have to be selected, and the construction has to be engineered based on the level of hazard that is critical. This proposed research will address several of these aspects.

1.2: Description of Threats and Shockwaves

1.2.1: Ballistic Impacts

A ballistic impact is generally described as a low-mass high velocity impact by a projectile propelled by a source onto a target. The high velocity impact may be initiated from handguns, rifles, and fragments or debris from explosive devices. During the ballistic impact, energy transfer takes place from the projectile to the target. The nature of the impact strongly depends on the properties of the projectile and target. Aspects of the two include the shape, size, velocity, and constitute material properties of the projectile and the material properties and makeup of the target. For impacts

corresponding to typical velocities from defense related terminal ballistics (~ 0.3 - 2 km/s), the peak strain rates generated are of the order of 10^5 to 10^6 s^{-1} [4]. All strain rates below the peak strain rate are likely to also be developed during the event at sufficiently long times and substantial deformation may occur as these lower strain rates as well as they are sustained for longer periods of time. Upon impact, a series of physical phenomena takes place in a very short period of time: elastic and plastic wave propagation, fracture and fragmentation, perforation, and spallation [5]. Unfortunately, these phenomena are yet to be fully understood and controlled. This is mainly due to the very quick time scales in which these phenomena occur, making observation and data collection difficult.
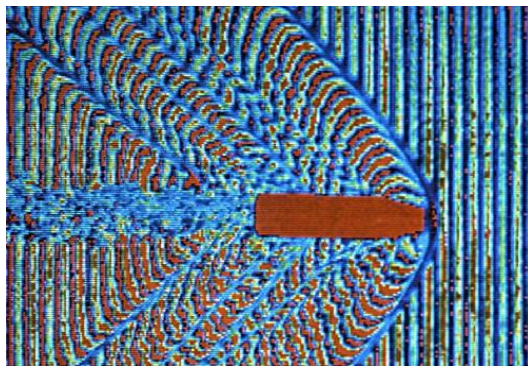
Figure 1. Bullet shockwaves. [6]

1.2.2: Explosive Devices

An explosive device is device that relies on the exothermic reactions of an explosive material to provide an extremely sudden and violent release of energy [6]. In the scope of this research, this includes devices such as grenades, missiles, bombs, mortars, and the so called improvised explosive device (IED). The Department of Defense describes an IED as:

3

"*A device placed or fabricated in an improvised manner incorporating destructive, lethal, noxious, pyrotechnic, or incendiary chemicals and designed to destroy, incapacitate, harass, or distract. It may incorporate military stores, but is normally devised from nonmilitary components [9]."*

The use of IEDs has risen significantly in the last few years with the US wars in the Middle East and the more frequent terrorist's attacks. In fact, in 2003, it was estimated that there were approximately 10 million IEDs planted underground in Iraq [7]. It has also been estimated that approximately 75% of deaths in Afghanistan were due to IEDs which is an increase from 40 to 60% of deaths in the Iraqi war attributed to IEDs [7]. The increase in use of IEDs is likely due to the ease in which IEDs may be produced from ordinary household items at low cost coupled with the magnitude of destruction they are capable of. A diagram of a typical homemade IED and its components is shown in Figure 2.
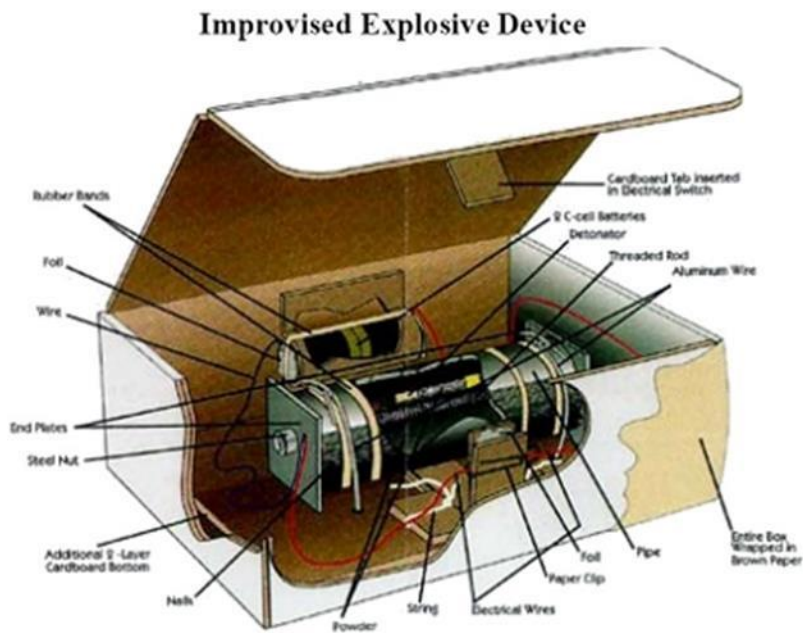
Figure 2. Schematic of IED. [7]

Currently, IEDs are the biggest threat to soldiers located in both Iraq and Afghanistan [8]. One reason for this is due to the very nature of IEDs as they are produced in low technology, makeshift methods with random items. This makes them hard to locate prior to detonation. IEDs can be detonated either remotely, by disturbance, or by suicide bombers. Injury can occur by either infringement of projectiles or fragments incorporated in the device or debris from surrounding structures disturbed by the blast. Also generated in the blasts are shockwaves which propagate at high rates from the detonation site and are capable of causing great destruction to surrounding structures and severe bodily harm to individuals in its proximity.

1.2.3: Shockwaves

Shockwaves are high speed, large-amplitude mechanical transients generated by violent impacts and explosions. They are caused by an extreme increase in pressure in a short amount of time which spreads out over a large area at high speeds [9, 10]. To be defined as a shockwave, the wave must be moving faster than the speed of sound, 340 m/s at sea level. It has been estimated that shockwaves may reach speeds of at least 1,600 ft/s (490 m/s) from the detonation point [10].

A blast or explosion results when solids or liquids are rapidly converted into a gas. In this state, the gas molecules become heated and highly pressurized. The heated gas expands into the surrounding air at speeds higher than that at which sound travels, compressing the air and creating a peak of overpressure wave or shockwave radiating from the point of detonation. Closely following the shockwave is a blast wind that also radiates from the point of detonation. As the gas expands, the pressure drops and creates a vacuum or negative pressure wave. The effects of the primary overpressure wave are nonlinear and very complex. The damage produced by the overpressure wave typically decreases exponentially from the blast epicenter. If the explosion is detonated within an enclosed space or if the blast waves travel inside an enclosed space, then the effects of

the blast waves become additive nonlinearly as the waves reflect off walls, floors, and ceilings. The discontinuous waves cause abrupt changes in density and pressure which can reach the range of giga Pascals (GPa) [11]. A diagram of a typical shockwave action is shown in Figure 3.

P_o = Peak Overpressure
t_p = Rise Time of Overpressure
t_r = Overpressure Duration Used in Approximations
t_i = Overpressure Duration or Length of Impulse
$t_s - t_i$ = Length of Suction Phase
Red = Impulse (area under positive portion
         of pressure-time curve)
Blue = Negative Pressure

Type of Curves Often Used in Approximations
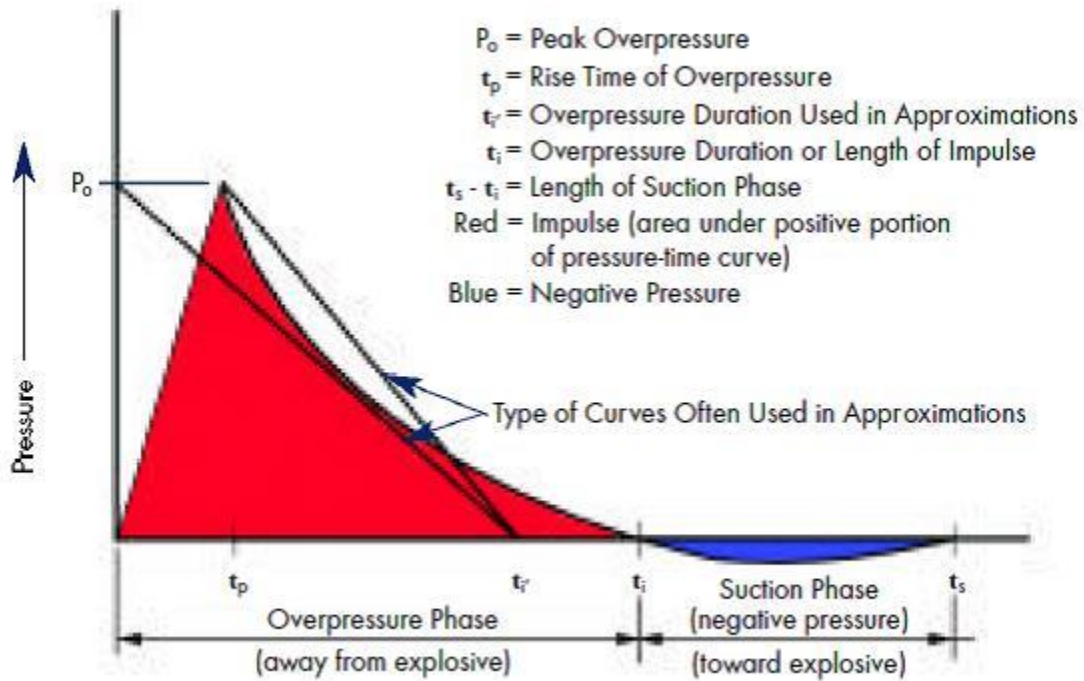
Figure 3. Blast wave parameters. [12]

In ballistic impacts, the kinetic energy of the projectile is transferred to the material at impact. Depending on the type of material impacted, some of the kinetic energy is dissipated through deformation and material failure at and near the impact zone. The remaining energy is then transferred to the impacted object and dispersed throughout the impacted material, being reflected and amplified at edges and junction points in a manner similar to shockwaves generated by explosions. Figure 4 depicts the dispersion of energy

6

from the projectile over the material.
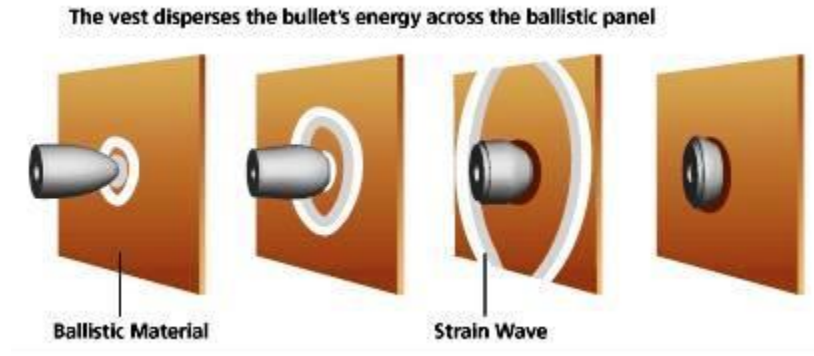
Figure 4. Mechanism of ballistic protection and stress dispersion. [12]

1.3: Injuries

The primary and ultimate function of anti-ballistic protection materials is to prevent fatality of individuals. While fatality may not occur if the armor is fully penetrated, the resulting types of injuries are not relevant to this application and will not be discussed here. The type injury of concern occurs when the armor performs its primary function of stopping projectiles. When the projectile is stopped however, a high strain wave or shockwave may still be spread to the underlying individual. As stated previously, this type shockwave is similar to those generated by explosions and both are capable of inflicting serious and sometimes fatal injuries. It is interesting to note that as advanced body armor and head protection gear have greatly reduced soldier fatalities from explosion and ballistic attacks, the problem of brain and internal organ injuries in the attack survivors has become more prevalent [14]. These blast and impact induced injuries which are typically not accompanied by visible, external bodily injuries have become a serious problem.

7

1.3.1: Blunt Trauma

When a projectile strikes body armor, although it may not fully penetrate said armor, injury can still be caused by two distinct mechanisms: localized deformation behind the armor due to out-of-plane displacement of the armor into the body and also via the shockwave created due to the rapid deceleration and transfer of energy from the projectile to the armor which propagates through the body.   Injuries due to the localized deformation are classified as "behind armor blunt trauma" (BABT) and in some cases result in fatality. In this situation, the armor distributes the impact energy over a large area causing global deformation to the chest. Localized deformation of the body armor can cause "back-face signature" in the armor, potentially causing lacerations to the individual. (Figure 5) Although the vest is successful in stopping the projectile, it is not effectively dissipating enough energy to stop large deformation on the back face of the armor in the impact area. The back-face signature of body armor is classified as the distance between the original plane of the back face of the armor and the point of maximum displacement of the projectile line of flight.
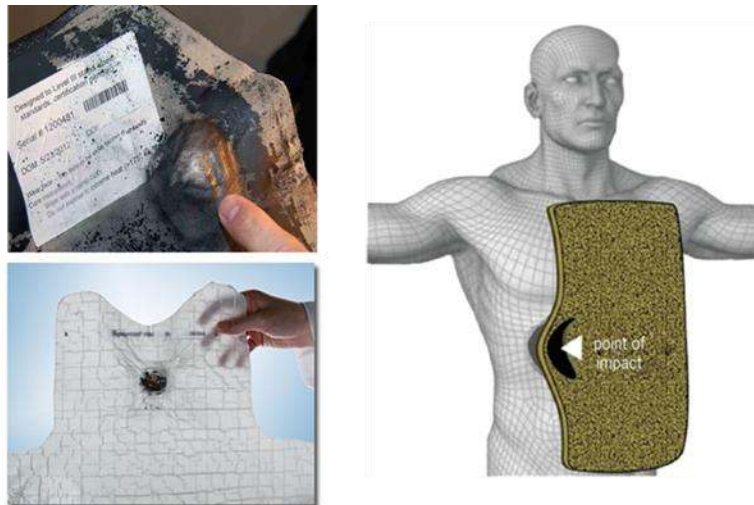
Figure 5. Back-face deformation. [6]

8

1.3.2: Traumatic Brain Injuries (TBI)

Traumatic Brain Injuries (TBI) resulting from impact and blast induced shockwaves are the most widely diagnosed injuries among the soldiers who returned from recent military conflicts. It has been dubbed "the signature injury of the Iraq and Afghanistan wars" [2]. As modern armor has substantially reduced fatalities, the lower mortality rates have also revealed the high prevalence of TBI. The increased use of IEDs has also led to more soldiers experiencing TBIs.

Brain injuries can be divided into two separate groups: blast-induced traumatic brain injuries (bTBI) and impact-induced traumatic brain injuries (iTBI). The mechanism by which a TBI occurs has been researched heavily in recent years due to lack of understanding of the injury. Research has brought forth different possible traumas which could be occurring inside the head during and following exposure. The most common explanation attributes the injury to the rapid compression of organs in the body due to the high pressure and high velocity shockwave [15]. Also, the sudden acceleration and deceleration forces often result in contusions of the frontal and temporal lobes which are located at the interface between soft tissues of the brain and the skull bones [16]. In addition, they often generate shear forces within different parts of the brain which displace at different rates, damaging brain white matter and the central nervous system (CNS).

Blast waves can also impose a complicated series of mechanical and physical reactions involving local bending, fracturing of the skull and density changes to the intracranial contents inducing strains and stresses in the brain tissues. This mechanism is known as coup-countercoup injury and is depicted in Figure 6 [18]. Coup contusions are produced by the impact of the brain at the loading location while counter-coup contusions follow from the bouncing of the brain against the inner posterior surface of the skull. Some of the common symptoms of a mild TBI include headaches, fatigue, difficulty sleeping, and vision problems while symptoms of a moderate TBI include forgetfulness, speech

problems, and decision-making issues [17]. Rehabilitation can include treatment at a trauma center where a course of action is specific to the patient and their situation.
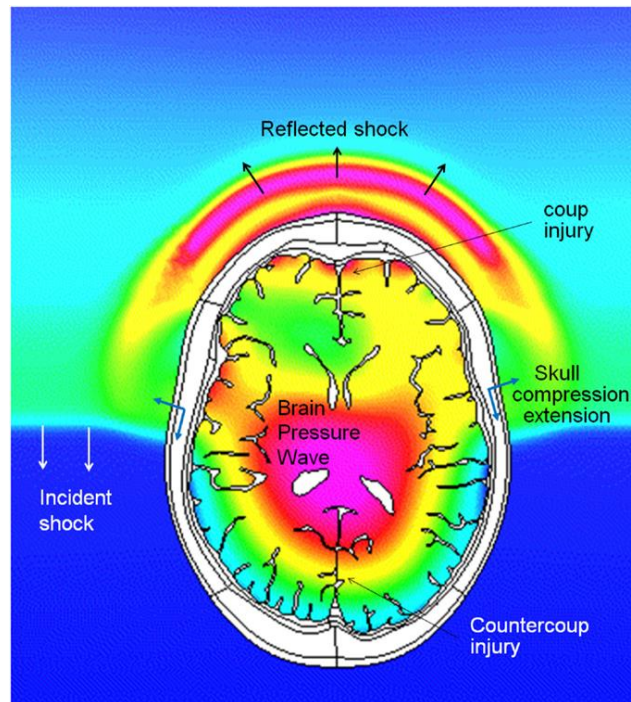
Figure 6. Pressure profiles in the air and in the brain during intracranial pressure wave penetration. Note that the intracranial pressure wave is faster than the incident shock wave in the air. [18]

1.4: Anti-Ballistic Protection Gear

The primary requirement of anti-ballistic protection gear is to limit penetration of the bullet, projectile, or fragment and prevent fatality. The secondary function is to dissipate kinetic energy of the projectile so that only a small fraction of it is transmitted to the underlying body. Modern armor systems are divided into two main categories: hard and soft body armor. The hard armor consists of hard metal or ceramic plates and generally hard armor offers greater protection than soft armor but is much heavier. Utilization of

soft fabric armor in certain ballistic applications is increasingly preferred over conventional rigid hard armor systems because of its superior strength-to-weight ratio and flexibility which allows the wearer mobility and comfort.

1.4.1: Personal Protection Gear

Bullet Resistant Vest

Since the emergence of the high performance aramids and ultra-high molecular weight polyethylene fibers in the 1960s, a significant improvement in comfort and ballistic efficiency has been observed [19]. These synthetic fibers possess high strength and moduli due to high degrees of polymer chain orientation in the fibers. With the advent of these fibers, personal protection gear was able to be fashioned at weights and flexibility which was comfortable to the wearer and had minimal effect on mobility. Today, bullet-resistant vests are quite literally a vital component of the uniform for many of the men and women serving our country, either in law enforcement or in the military, and have been directly attributed with saving thousands of lives. The impact resistance of a soft armor depends on its capability to absorb energy locally at the impact zone and disperse energy rapidly out of the impact zone. These characteristics are determined by a number of factors: fiber intrinsic properties, fabric structure characteristics (ie. woven pattern, nonwoven), number of layers, amount and type of binder if used, projectile shape, mass, and intrinsic material properties of the projectile, impact velocity, and interfacial friction characteristics within the impact zone [20, 21] .

The principal factor that dictates the design of body armors is the type(s) of threat(s) for which protection is required that is, ballistic, fragment, blast, stab, slash, chemical, fire, etc. Armors optimized for protection against one threat type may not, however, be suitable for other threat types. For example, textiles designed for ballistic protection

require sufficient yarn mobility within the weave to avoid premature failures and typically these materials will not perform well for stab protection. Textiles designed for stab resistance require dense weaves to prevent yarns from being pushed aside from the tip of sharp pointed objects such as knives, needles, awls, and ice picks. Dense weaves that prevent punctures can lead to premature or punch-through failures in ballistic impacts. Consequently, design parameters for optimizing both ballistic defense and stab defense often work against each other. This is similar to the issues with resulting blunt trauma after ballistic impact regarding soft body armor preventing penetration to the underlying individual by stopping the high velocity projectile and dissipating the blast and shockwave energy.

Most vests are made from tightly woven Kevlar or Spectra fibers and are designed to withstand bullets fired from handguns and shotguns, as well as fragments from hand grenades and other explosive devices. Metal and ceramic plates can be added to ballistic vests for additional protection, and to help shield soldiers from knife attacks and stabbings. Most combat soldiers wear "hard plate vests" that have the additional plate protection. As stated previously, many aspects of the vest and projectile are involved in the outcome of a ballistic impact. Today, ballistic-resistant vests are fabricated to different levels of protection with a tradeoff between more protection and wear-ability or concealability. The 3 most prevalent levels of antiballistic vests are:

    Level II-A: ~ 4 mm thick
    Level II: ~5 mm thick
    Level III-A: ~ 8 - 9 mm thick

 The vests may consist of 8 to 24 layers of woven high performance fiber plies which are sandwiched together with heat and pressure [22]. The fibers can be woven together into a number of configurations, some of which are illustrated in Figure 7, to provide varying degrees of performance and flexibility. Fiber structures for armor applications have traditionally been in unidirectional, plain, or basket weave configurations. Unidirectional

fiber layers may be rotated 90° with respect to adjacent layers to create a cross-ply fabric. Additional woven structures have been studied for armor applications, such as 3D structures to enhance the multi-hit capability of the materials.
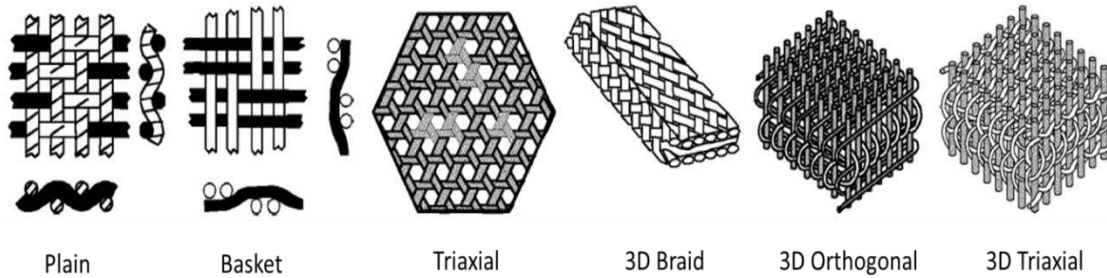
Figure 7. Woven fiber structures [22].

Figure 8 shows the Interceptor Ballistic Armor (IBA) vest currently worn by US military troops. Depending on the size and additional add on, it can weigh from 8 to 33 pounds [22]. The IBA is a modular system that consists of an outer vest, ballistic plates, and attachments that increase the area of coverage. It increases survivability by stopping or slowing bullets and fragments and by reducing the severity of wounds.

Figure 8. Different camouflaged Interceptor vests. [23]

Military Helmets

Helmets have been used for head protection for centuries and are routinely updated as better technology and ballistic protection are achieved. In the early 1960s, the US Army embarked on a program to replace the M1 steel helmet design with a single-walled, lighter, and more protective configuration. After considerable research and development efforts, the improved Personnel Armor System for Ground Troops (PASGT) combat helmet made using Kevlar fibers and phenolic resin replaced the steel M1 helmet. Composite materials have been found to offer increased protective performance for a given mass when compared with steel, thus all of today's combat helmets are composed of aramid or polyethylene based composites. Since the PASGT helmet, the Advanced Combat Helmet (ACH) has been produced to reduce weight and increase anti-ballistic performance and comfort (Figure 9) [24]. To add additional energy dissipation qualities and comfort to the helmets, various padding systems have been developed. The ACH utilizes a 9 pad system which is shown in Figure 10. These pads are made of polyurethane foams with size and dimension specifications for optimal performance. These foams have helped somewhat helped alleviate the TBI problem but not to sufficient degrees.

Figure 9. Military helmets. [24]
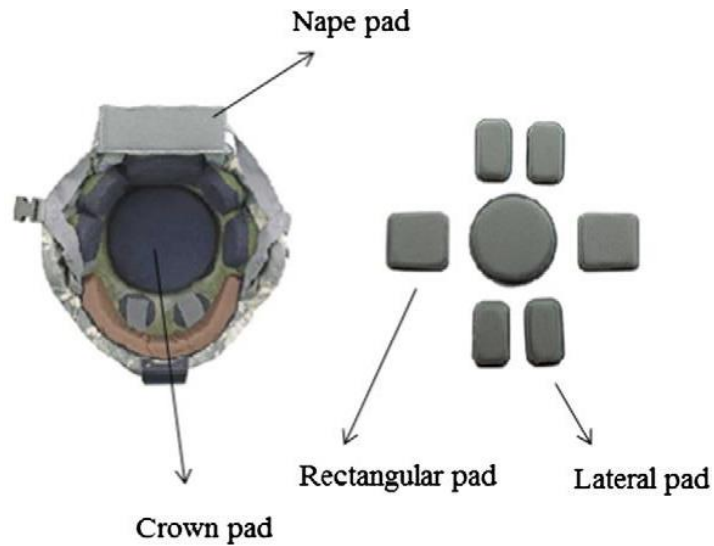
Figure 10. ACH and its parts.[24]

1.5: Proposed Addition to Existing Personal Protection Gear

As noted previously, while current anti-ballistic personal armor is generally effective at preventing projectile penetration to the underlying individual, they are not sufficient at absorbing the remaining kinetic energy of the impact or shockwaves generated by explosions. This research will attempt to address these armor shortcomings by developing flexible shockwave absorbing protective panels from nanoparticle reinforced elastomeric fibrous sandwich composites of light weight which can be used as a liner in conjunction with current antiballistic materials to minimize shockwave induced trauma soldier's experience. This addition to existing armor will be of minimal weight and may even allow for reduction of primary anti-ballistic layers.

15

CHAPTER 2: LITERATURE REVIEW

2.1: Thermoplastic Elastomers (TPEs)

Thermoplastic elastomers (TPEs) are a class of polymers which have the elastic behavior of thermoset elastomers and the processability of thermoplastics. The development of thermoplastic materials having elastic properties started in the early 1930s at BF Goodrich with the invention of plasticization of PVC [25]. In 1937, scientists at DuPont made a major breakthrough with the discovery of basic diisocyanate polyaddition reactions which was applied to urethane polymers. After much research, the first thermoplastic elastomer was commercialized by DuPont as thermoplastic polyurethane (TPU) in 1958 [25]. Since then, a few other thermoplastic elastomers have been commercialized to bridge the cost/performance shares of the elastomer market (Figure 11) [26]. The TPEs listed in Table 1 are the six primary TPEs which are relevant in today's market. These six TPEs fall into one of two classes, multi block copolymers and polymer blends. The olefin elastomers are part of the blend class while the remaining TPEs are multi block copolymers.
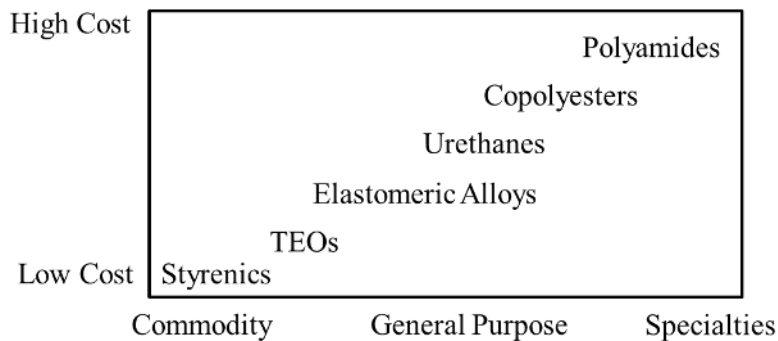
Figure 11. Cost and performance of TPEs. [26]

Table 1. Commercialization of thermoplastic elastomers.

TPE	Year	Manufacturer
Thermoplastic Polyurethane (TPU)	1958	DuPont
Styrene Block Copolymers (SBC)	1965	Shell
Copolyesters (COPE)	1972	DuPont
Olefin Blends (TPO)	1976	Uniroyal
Olefin Vulcanates (TPV)	1981	Monsanto
Copolyamides (COPA)	1982	Dow

Since the commercialization of the first thermoplastic elastomers, the growth of TPEs has been truly phenomenal with an annual growth rate of 8 to 9% per year between 1970 (100,000 metric tons) and 1990 (650,000 MT) [26]. TPEs have mostly found their use in replacement of thermoset rubber compounds in existing parts, but have also found new applications in the medical, housewares, and fiber industry among others. While the class of thermosets is made of a broader chemical composition, the major distinguishing difference in thermoset elastomers and thermoplastic elastomers is the type of crosslinking between polymer chains. Thermosets are typically molded followed by chemical crosslinking through vulcanization with sulfur or curing with peroxide crosslinking agents. These crosslinks are irreversible and the final product is unmeltable. Some examples of thermoset elastomers include: latex, silicone, and neoprene (natural rubber). The vulcanized chemical structure of neoprene is shown in Figure 12a. Thermoplastics are physically crosslinked by crystallization between short segments of adjacent polymer chains and reversible hydrogen bonding (Figure 12b) [27]. These crosslinks may be broken under strain or heat but reform once the source of deformation is removed [27]. The ability to be melted multiple times is a major advantage for TPEs as they may be recycled.
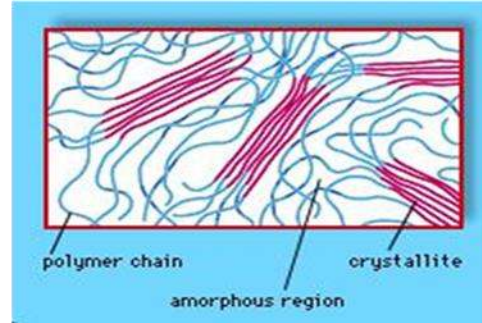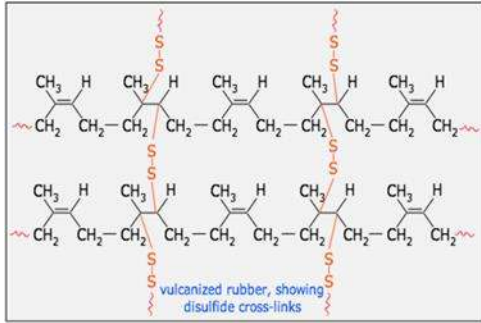
Figure 12. a.) Vulcanized Neoprene. [28] b.) physical crosslinking by crystallization.

2.1.1: Structure and Morphology of TPEs

Thermoplastic elastomers are generally composed of incompatible components where their free energy of mixing (ΔG_{mixing}) is ≥ 0 [25]. Upon cooling, these incompatible components undergo phase separation to reach a more favorable entropic state (Figure 13). This phase separation is what allows the polymers to act as elastomers. The more incompatible the components, the better the phase separation will be and the greater the elastic properties [27]. Virtually all TPEs consist of at least two polymeric phases, a dispersed hard thermoplastic phase and a continuous soft elastomeric phase. The properties of the resulting TPE will be derived from the properties of each of the two phases and their mutual interaction. In multiblock copolymers, the hard and soft phases alternate along the chain (Figure 14). The olefinic blends have random arrangement of the hard segments along the chain but still consist of two separated phases.
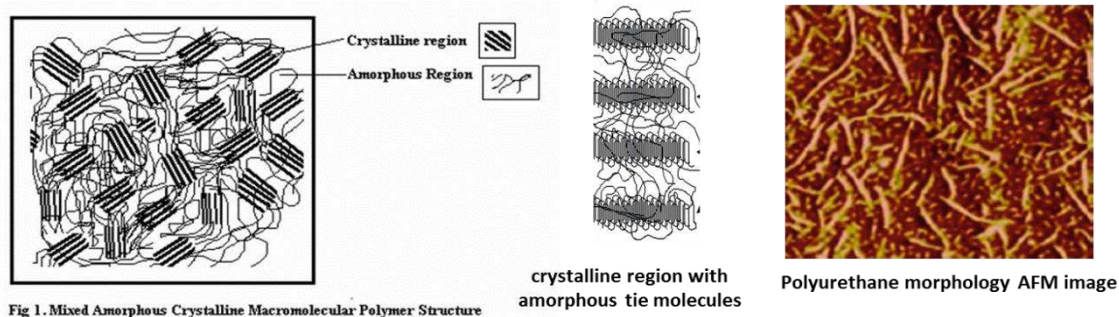
Figure 13. Morphology of TPEs. [30], [52]
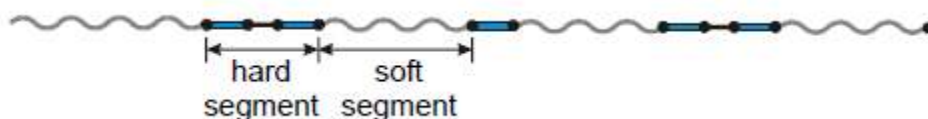
Figure 14. Block copolymer TPE alternating segments. [27]

Mechanical properties are controlled by the hard/soft segment ratio [28, 29]. The soft segments are typically composed of low Tg polyethers, polyesters, or glycols. They form the continuous amorphous phase and control the elasticity, hydrolytic stability, chemical stability and other low temperature properties [29]. The polyether types are slightly more expensive and have better hydrolytic stability and low temperature flexibility than polyester types. Mechanical strength properties of the polyester types are generally higher however due to the higher degree of hydrogen bonding which leads to greater phase mixing and stronger interchain bonding [29]. As the hard segment content is decreased and the soft segment is increased, the strength decreases and elongation increase. These composition alterations allow producers to provide TPEs to cover a broad range of properties.

The hard blocks account for the mechanical stability of the material. They give rise to reversible crosslinks which are embedded in the low glass transition temperature amorphous phase. Above the melting temperature of these hard domains, a viscous polymer melt is obtained which can be processed easily on conventional thermoplastic equipment. The hard blocks are generally based on polyester, polyamide, or polyurethane segments. At ambient temperatures, the hard blocks are incompatible with the soft blocks. This induces microphase separation by crystallization upon cooling from the melt. The ordered arrays are formed by the crystallized hard blocks (Figure 12b and 13). Hard blocks that are not crystallized are dissolved in the amorphous soft phase, and this incomplete phase separation leads to an increase of the glass transition temperature of the soft phase, which is undesired for the low temperature flexibility and elasticity of the material therefore the need for high incompatibility of the segments [29].

Upon static deformation of these materials, the hard blocks remain crystalline and do not deform. However, the soft elastic domain is easily deformed with the hard segments acting as tie points that function both as physical crosslinks and reinforcing fillers. The recovery of TPEs is good as long as the domains are not strained to greatly and the temperatures are well below the crystallization temperature. Irreversible changes in their morphologies may occur above a certain point as the hard blocks are disrupted and reorganize, resulting in energy dissipation but incomplete recovery to their initial dimensions.

2.2: Thermoplastic Polyurethane (TPU)

A TPU is prepared from three types of chemicals: a diisocyanate, a macroglycol (polyol), and a short chain extender to form a multiple hard/soft block structure [30]. The diisocyanate can be aromatic or aliphatic. Diphenylmethane diisocyanate (MDI), toluene diisocyanate (TDI), and naphthalene diisocyanate (NDI) are common aromatic monomers utilized in commercial fiber resins. Their structures are shown in Figure 15.

4,4-methylene-bis-
(phenylisocyanate) (MDI)

1,5-naphtalene
diisocyanate (NDI)

2,4-toluene diisocyanate
(TDI)
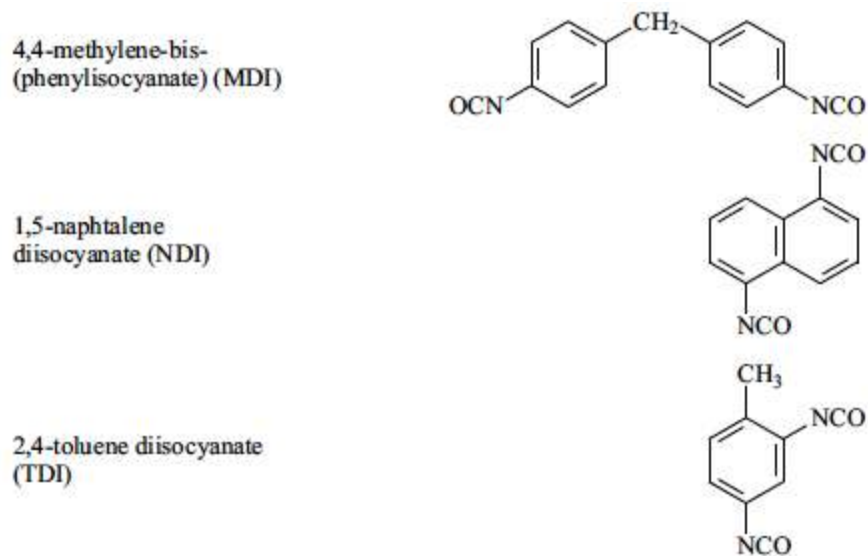
Figure 15. Commonly used aromatic diisocyanates. [30]

The diisocyanate and short chain extender form urethane linkages and are the basis of the hard segments (HS). The urethane linkages in the hard blocks are capable of a high degree of inter and intramolecular hydrogen bonding. Such bonding increases the crystallinity of the hard phase and can influence the mechanical properties.

The chain extenders play a very important role. Without a chain extender, a TPU formed by directly reacting diisocyanate and a polyol generally has very poor physical properties and often does not exhibit microphase separation. The introduction of a chain extender increases the HS length to allow HS segregation, which results in good mechanical properties, such as an increase in the modulus and an increase in the HS glass transition temperature of the polymer [30]. TPU chain extenders can be categorized into two classes: aromatic diols and diamines and the corresponding aliphatic diols and diamines. In general TPUs chain extended with an aliphatic diol produce a softer material than do their aromatic chain extended counterparts [30]. The chain extender structure strongly influences the TPUs mechanical performance. By modifying the ratio between the polyol and chain extender, TPUs may result in a change from a hard, brittle material to a rubbery

elastomer, as a result of the variation of the HS concentration (defined as the ratio of the mass of the non-polyol components to the total mass of the polymer) [30]. Some common diol chain extenders include: ethylene glycol (EG), diethylene glycol (DEG), butanediol (BD or BDO), hexane diol (HG), octanediol (D) and aromatic diols such as teiazine diol. Examples of diamine chain extenders include: diamino-dibenzyl (DAB), diamine-pyridine (DAPy), and methylene diamine (MDA).

The long chain macrodiols used for the soft segment (SS) typically have a molecular weight between 600 and 6000 and can be divided into polyester and polyether diols [29]. Some examples are shown in Figure 16. With higher molecular weight, the degree of phase separation of the two phases increases. These long chain diols form the continuous amorphous phase.

Polyester Macrodiols

(PEA) polyethylene adipate glycol

$$H-[O-(CH_2)_2-OCO-(CH_2)_4-CO]_n-OH$$

(PCD) poly(caprolactone) glycol

$$H-[O-(CH_2)_5-\underset{O}{\overset{\parallel}{C}}-O-(CH_2)_5-\underset{O}{\overset{\parallel}{C}}]_n-OH$$

(PBA) polytetramethylene adipate glycol

$$H-[O-(CH_2)_4-OCO-(CH_2)_4-CO]_n-OH$$

(PHA) polyhexamethylene carbonate glycol

$$H-[O-(CH_2)_6-\underset{O}{\overset{\parallel}{OCO}}-(CH_2)_6-\underset{O}{\overset{\parallel}{OCO}}]_n-OH$$

Polyether Macrodiols

(PTHF or PTMO) polytetrahydrofurane or polytetramethylene oxide or poly (tetramethylene ether) glycol

$$H-[O-(CH_2)_4]_n-OH$$

(PPO) poly(propylene) oxide

$$H-[O-HC-H_2C]_n-OH \quad (\text{with } CH_3 \text{ branch})$$

(PEG) poly(ethylene) glycol

$$H-[O-CH_2-CH_2]_n-OH$$

(PBU) polybutadiene diol

$$HO-[CH_2-CH=CH-CH_2]_n-OH$$

Figure 16. Commonly used macrodiols for TPU soft segments.

The ether (C-O) bond in the polyether soft segment (SS) and ester (CO-O) bond in the polyester are capable of hydrogen bonding with the urethane linkages (NH-CO) in the hard domain, influencing the degree of phase segregation. There is also hydrogen bonding within the hard segment urethane groups. Figure 17 shows the hydrogen bonding interactions found in thermoplastic polyurethanes. The polyesters are generally stronger hydrogen bond acceptors than polyethers as they generally have no unreactive end groups which contribute the higher strength of polyester based TPUs [30]. The increased polarity of the ester carbonyl group also leads to stronger hydrogen bonding between the hard and soft segments. Therefore, polyester based TPUs typically have enhanced phase mixing due to the increased number of ester groups capable of forming

23

hydrogen bonding with the urethane groups of the hard segments while polyether based TPUs have higher phase separation.

The phase mixing of polyester based TPUs leads to a higher temperature dependence of the TPU properties including more hysteresis or stress softening [29]. The higher degree of hydrogen bonding leads to higher strength and modulus, better chemical resistance to solvents and high temperatures but leaves them susceptible to hydrolytic chain scission. In contrast, polyether based TPUs typically have good hydrolysis resistance and flexibility. The polyether based TPUs usually have a lower glass transition temperature than polyester based TPU with equivalent SS molecular weight due the better phase separation and less phase mixing.
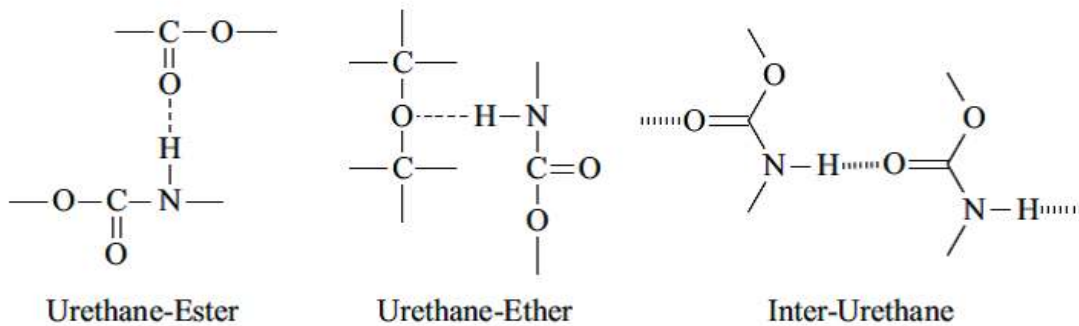
Figure 17. Hydrogen bonding in TPU. [30]

TPUs are melt processed into single fibers, yarns, spunbond, and melt blown into nonwovens. Very little literature of TPU fibers can be found as most research and development has been done in industry. A few articles concerning melt blowing and crystallization kinetics of TPU have been published [76-79]. Numerous patents have been filed covering a broad range of chemical compositions. Newer research is directed at shape memory TPUs which are heat activated. These shape memory TPUs offer

advantages over the traditional shape memory alloys as well as new applications which are designed to take advantage of their behavior [31].

There are numerous manufactures of TPU fiber-grade resins and fibers. A few of the notable supplier and product names in the US are BASF (Ellastolan), Bayer (Texin), and Lubrizol (Estane and Pelletane). An MDI hard segment and polyester based SS TPU from Lubrizol is shown in Figure 18. TPU fibers are the most used out of the four TPEs used in fiber spinning and elastic fiber applications. It is a common belief that the traditional Lycra or Spandex fibers are thermoplastic elastomers and melt processed, however the majority on the market are dry spun while others are wet spun. These polymers are polyurethane-urea based and degrade at temperatures below the urethane/urea linkages melt. This along with extensive hydrogen bonding prevents most from being melt processed.
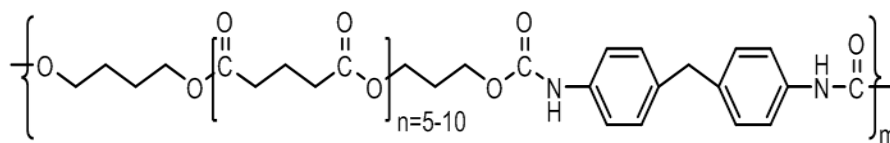
Figure 18. Estane, a polyester based TPU from Lubrizol.

2.2.1: Shore Hardness

TPUs are commonly rated by shore hardness. Shore hardness is a measure of the resistance of a material to penetration of a spring loaded needle-like indenter. Shore A scale is used for testing soft elastomers and other soft polymers. Hardness of hard elastomers and most other polymer materials is measured by Shore D scale. A conversion scale for the two is shown in Table 2. Shore hardness may be used to relate a

25

hard/soft segment ratios and mechanical properties.

Table 2. Shore hardness conversion table.

Shore A	45	50	55	60	65	70	75	80	85	90	95	100
Shore D	10	12	14	16	19	22	25	29	33	39	46	58

2.2.2: TPU Fibers

Fibers extend and contract by conformational change from compact random coils to extended chains as shown in Figure 19.   Conventional fibers like polyethylene terephthalate, nylon, acrylic, polypropylene etc., which have the stress strain curves as shown in Fig. 20 exhibit strain up to 50% depending upon the fiber type and show little recoverable extension which is sufficient for the traditional apparel end uses.
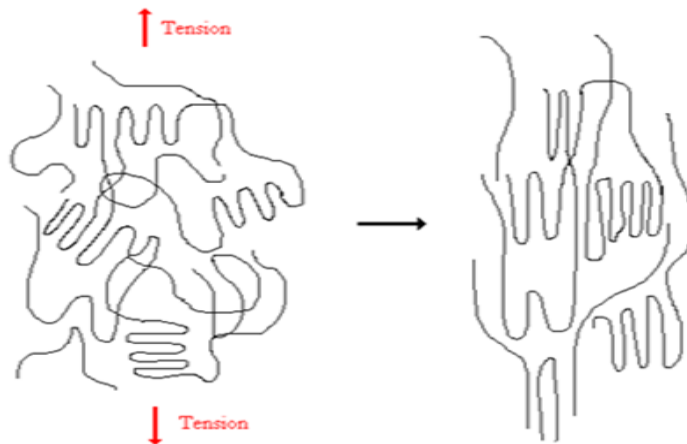
Figure 19. Polymer chain alignment extension under tension.
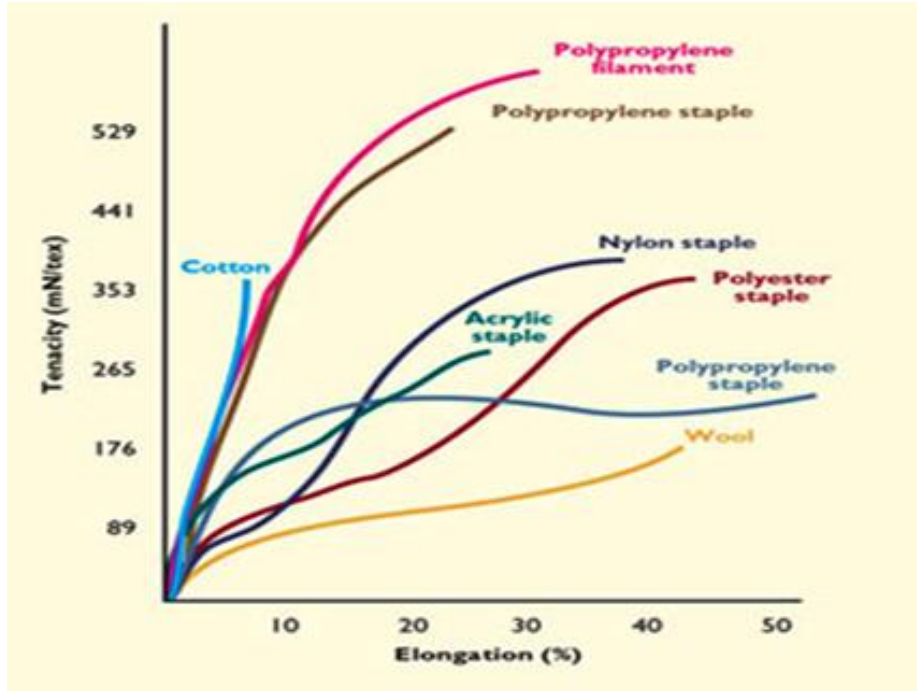
Figure 20. Typical tensile curves of thermoplastic fibers. [32]

The amount of stretchability desired in the products like sportswear, leisurewear, stockings, tights, socks, underwear, elastic bands in clothes, and personal care products like baby diapers, incontinence products, and medical bandages is far higher than these levels achieved by the conventional fibers [33]. TPUs have the potential to exhibit the required level of extensions as shown in Figure 21. Note the elongation ranges from ~ 300 to 750%. This graph also shows the effect of changing the hard/soft segment ratio. The fiber of 75D shore hardness has a tensile strength of ~ 10,500 psi with ~ 300% elongation. As the ratio of hard to soft segments decreases (75D to 80A), the strength decreases and the elongation increases. All of the TPEs show this trend with hard/soft segment ratio chemistry changes.

27
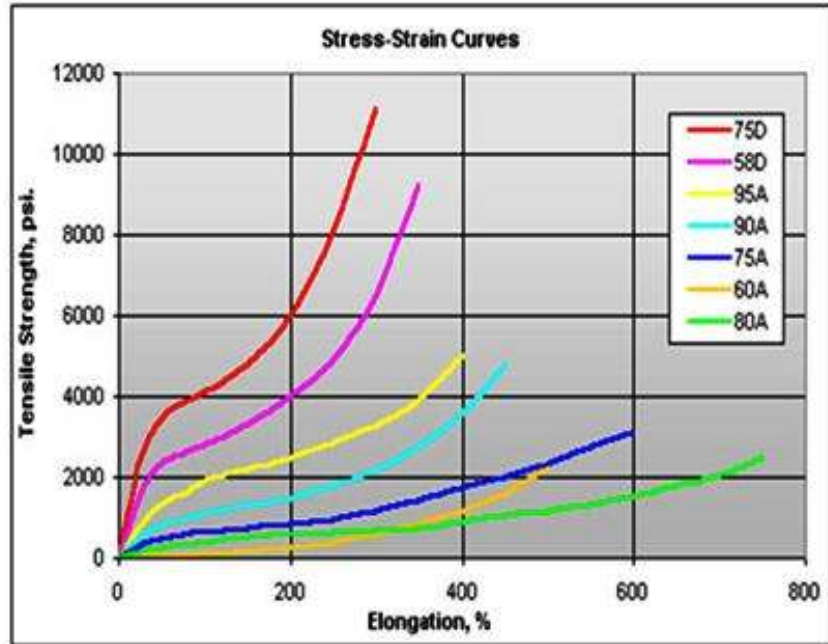
Figure 21. Tensile curves of TPU fibers. [33]

2.3: Energy Dissipation Mechanisms of Elastomers

Research in elastomer energy absorption and dissipation has increased in recent years due to the increased number of soldiers suffering from TBI and blunt trauma. The high cost for the development of a new high performance fiber which may at least maintain current antiballistic properties while improving upon the residual energy dissipation also led to investigation of existing materials in which little research had been performed for mechanical properties at high strain rates. It is well known that thermoplastic polymers and especially elastomer mechanical properties are strain rate dependent. In particular, phase separated copolymers have displayed outstanding energy dissipation capabilities and researchers have suggested this could be a result of the phase separated structure [34]. Even with the abundant research devoted to elastomers, the nonlinear viscoelastic mechanisms and dynamics in polymers during and immediately following ballistic or

28

blast events remain obscure. A major problem in investigation of polymer behavior at high strain rates is the lack of methods and instruments which can be utilized to study the phenomena exhibited on those time scales as well as difficulty relating to easily attainable small strain, linear viscoelastic measurements in DMA to large strain, highly nonlinear behaviors encountered at impact. Polymers exhibit strong rate-dependent mechanical behavior and in a high frequency regime, the rate sensitivity of polymers changes as various primary and secondary molecular mobility mechanisms are accessed.

Early research focused on qualitative correlation between the mechanical dampening peaks and impact toughness of polymers. Heijboer et al [35] and Boyer et al [36] observed that if a polymer possesses subambient relaxations (γ and α) which originate from side chain and main chain motions, the polymer would exhibit good impact toughness at room temperature. The α transition also known as the glass transition is a second order transition during which the first order Gibbs free energy terms, (volume, enthalpy, entropy) remain constant while second order derivatives such as specific heat and coefficient of thermal expansion undergo change [54]. Though the glass transition is generally reported as a single temperature, it occurs over a range of temperatures. For ease in quantifying, Tg is generally taken to be the temperature at which half of the transition is complete. During this transition when the temperature is increasing, the polymer behavior changes from glassy to rubbery over the Tg range, and the opposite occurs on cooling through Tg. Tg can be monitored during calorimetric experiments or under dynamic mechanical loading in the linear region of the polymers viscoelastic properties over the appropriate temperature range. It should be noted that the two methods will give different results with the DMA Tg value typically being greater.

Vincent et al [37] disputed this relationship of dampening peak (γ transition) and impact toughness proposed by Heijboer and Boyer, citing a large number of polymers in which only about 60% of the cases could be accounted for by the loss peak toughness relationship. Never the less, many other researchers have been able to make correlations between polymer viscoelastic properties in the linear regime with nonlinear behavior at

strain rates and time scales associated with blast impacts and shockwave energy.

Of the multitude of elastomers available in the market, much research has been devoted to polyurea as a coating or laminate on hard armor and structures for blast resistance and reduction of fragmentation. This polymer is very similar to polyurethane with only nitrogen in place of the oxygen in urethane (Figure 22) while maintaining the hard/soft separated phase morphology. Reflecting the performance advantages of the polymer and the desire to further its application, there has been a large amount of experimental research aimed at a better understanding of the structure, molecular dynamics, static and dynamic mechanical properties, blast and impact resistance, constitutive modeling, and sophisticated multi-scale modeling [38-56].
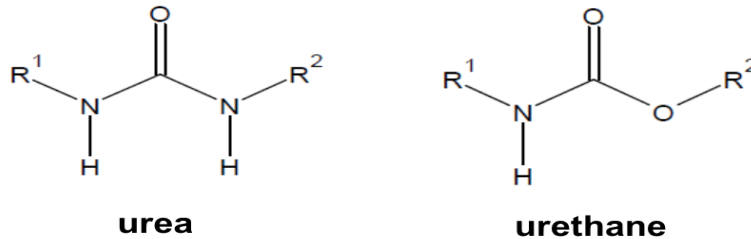
urea   **urethane**

Figure 22. Urea and urethane chemical structures.

Rowland et al [38-43] has done extensive research into polyurea and various other elastomers to a lesser extent under high strain rate deformation. He found that not only is the polymer behavior dependent on the rate of deformation but also on the temperature and pressure increases caused by ballistic impacts and shockwaves. Particularly, if the loading or impact imposes a strain rate sufficiently high that the material response extends to frequencies beyond the rubbery plateau regime of the viscoelastic spectrum, large scale rearrangements of the polymer chains over a significant length are precluded [40]. Under these conditions, the elastomers rubbery like behavior becomes more leather

like as it transitions into the glassy state and displays large energy dissipation [52]. An important aspect of this phenomenon is the relaxation time (τ) of the segmental dynamics of the polymer in comparison to the strain rate during loading. For ballistic impacts and shockwave infringement, the strain rate may be as high as 10^5 s^{-1} or more. If the polymer chain relaxation time is similar, the deformation will involve the polymer segmental dynamics and relaxations by transferring to the glassy state. However, if the deformation rate is too low (low frequency) compared to the chain relaxation time (t >> τ), the material will respond in a rubber like fashion due to large scale mobility of the chain segments. If the deformation rate is very high (high frequency), the material will behave like a glass as the chain motions will be frozen out (t << τ) leaving the material with little energy dissipation ability. To analyze this, Rowland investigated two materials with different Tg and relaxation times, polyurea and polybutadiene. The polyurea had the higher Tg and shorter relaxation time of the two. Under the same high strain rate testing conditions, he found the polyurea to undergo phase transition from rubbery to glass while the polybutadiene remain in the rubbery state. The polyurea was able to absorb over two orders of magnitude more energy than the polybutadiene due to the phase transition during impact. To exploit this effect, Rowland proposed that the polymer must have a relatively high Tg being close to the operating temperature. Also since the glass transition is rate dependent, the polymer Tg should be 5 to 20 degrees lower than the service temperature with a broad transition to further maximize the deformation-induced glass transition energy absorption phase change.

Other possible energy dampening mechanisms of polyurea or polyurethane could involve the breakage of H-bonding between chains, the high frequency resonance of the hard segments, the viscous dissipation of the soft matrix, and the nano and micro-scale interactions with the separated phases.

2.4: Melt Blowing Process

The melt blowing process concept was developed by Wente in the 1950s at the Naval Research Laboratory and later further developed and commercialized by Exxon Chemical Company in the early 1970s [57,58]. Since then it has become one of the major nonwoven processing methods utilized commercially due to its high quality webs and fast production rate. Melt blowing may best be described as a process in which thermoplastic polymer granules are fed into a heated extruder where they are melted and mixed and then pumped into the die. The molten polymer is then extruded through the die orifices into converging hot air streams that rapidly attenuate the fibers while transporting them to the collector [57]. When the fiber exits the die, it immediately begins cooling and usually completes quenching while on the collection belt, forming a self-bonded nonwoven web. The average fiber diameter of melt blown nonwoven microfiber webs typically average from 1 – 10 um depending on the polymer viscosity and processing conditions. Conventional fiber spinning methods and spunbonding typically produce textiles with average diameters between 12 and 50 um [58]. The small fiber diameters of melt blown nonwoven webs give them excellent filtration qualities and consequently filtration applications present a great demand for nonwoven webs. Other applications that utilize nonwoven materials include: hygiene products (i.e. wipes), wound dressings, tissue scaffolding, oil absorbents, thermal insulators, battery separators, and various apparel garments [58, 59].

A typical melt blowing line (Figure 23a) consists of a hopper, extruder, metering pump, a multi-hole die assembly, an air compressor, air heaters, a collection belt equipped with a suction system, and a winding apparatus. Consequently there are numerous parameters which have an effect on the final properties of the melt blown nonwoven web. Starting from the beginning of the process, the extruder speed and temperature zones, the metering pump speed and temperatures, the die design and orifice diameter, die temperatures, air temperature and flow rate, the die-to-collector distance (DCD), and collection speed all play a role in the final web quality and properties. Some melt

blowing lines may also use a secondary quenching air system to solidify the fibers at a faster rate. Many of the web characteristics can be manipulated by altering multiple process parameters. For instance, the average fiber diameter mainly depends on the die orifice size, throughput rate, melt viscosity and die temperature however, air temperature and velocity can also have a significant effect for some polymers while DCD can have a small effect under select processing conditions. The web basis weight (g/m^2 or gsm) depends on the throughput rate, die orifice density and collection speed. Other properties such as strength and elongation, pore size, and permeability are largely influenced by the temperature of the fiber exiting the die, air temperature, air velocity, and DCD.
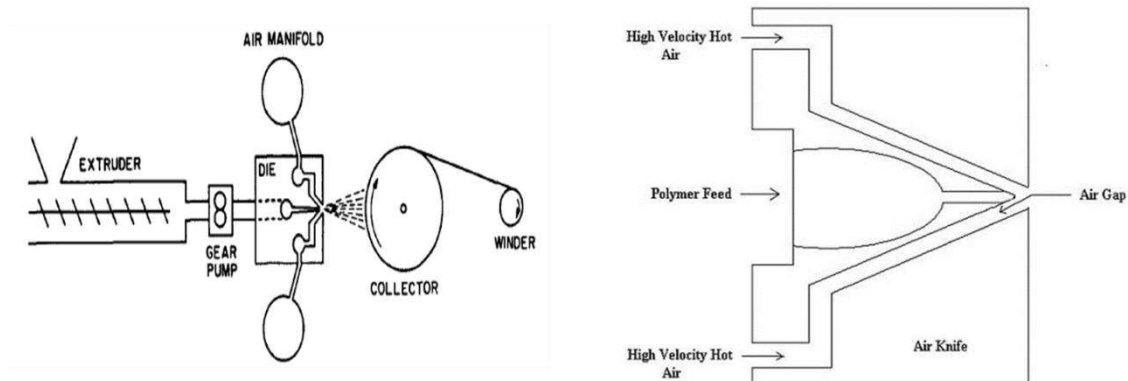
Figure 23. a) Schematic of horizontal melt blowing line. b) Exxon style melt blowing die.

The die assembly is the most important part of the melt blowing line and must be precisely engineered for production of acceptable quality webs. It consists of three components: the polymer distribution, die faceplate/nose, and air flow manifolds [60]. The polymer distribution may utilize a conventional T or straight manifold, fishtail, or coat hanger geometries. Most commercial systems utilize the coat hanger type which is also used in this study. (Figure 24) It is designed to yield a uniform polymer flow and

temperature distributions at the die exit without excessively increasing the pressure drop in the die.

Figure 24. UTNRL 15.4 cm (6 in) melt blowing line coathanger.

The die nose piece geometry has a great influence on the uniformity of the web. The prevalent geometries in melt blowing are: slot dies (Exxon style shown in Figure 23b), Hills, AGR/NTI, and annular capillary (Biax) [61]. The melt blowing dies typically contain several hundred orifices in single or several rows and must be precisely engineered to very tight tolerances. Hole diameters may range from 0.3 mm or larger for microfibers to 0.03 mm for nanofiber production. The angle and the gap or air distance the die nosepiece (see Figure 23b) makes with the air manifold also influence web uniformity and fiber attenuation.

Little research has been published concerning the melt blowing process and the properties of the nonwoven webs produced at different parameters. This is likely due to the high startup cost for pilot scale melt blowing lines to be used in academics as industry doesn't typically publish. Many researchers have adapted by building small single and multi-hole orifice melt blowing equipment to investigate aspects of the process and formulate mathematical models. Shambaugh and coauthors [62-68] have modeled many aspects of melt blowing concerning die geometries, air flow fields, and air temperature profiles and their influences on fiber diameter and distributions. Sun [69] and Xin [70] modeled melt

34

blown fiber formation and whipping motion while Tan and Zhau [71,72] modeled viscoelasticity effects.

Provided the molecular weight is not too high, any thermoplastic polymer can be melt blown though very few species have been reported on. PP is by far the most used in commercial operations. Lee and Wadsworth [73,74] investigated the effect of different processing conditions on 700 MFR PP webs produced on a 20 in. melt blown line equipped with an Exxon style die (401 holes of 0.4 mm diameter) at a throughput rate of 0.4 g/hole/min. They found little change in average fiber diameter with changes in DCD. However they did see significant diameter decreases with decreasing die temperature and increasing air velocity. They also found air permeability and pore size to increase with increasing DCD while both decreased with increasing die temperature and air velocity. They proposed these changes were due to the average fiber diameter and the degree of fiber entanglement and bundling in the web at the respective die temperature and air flow rates. From examination of SEM images, they determined the degree of entanglement to decrease with decreasing DCD and increasing die temperature and air velocity. They also studied strength properties of the webs in the machine (production) and cross (transverse) directions. Overall they found strength to decrease with increasing DCD while elongation increased. Machine direction (MD) strength was greater than CD strength at low DCDs and became similar as DCD increased due to decreasing fiber orientation in the web at higher DCDs. Web strength was also found to increase with increasing die temperature and air velocity. Bresee [58,75] studied effects of DCD on fiber entanglement, fiber orientation, and pore structure of 1259 and 400 MFR PP. All of his findings were similar to Lee [73,74] except he found fiber diameter and entanglement to increase with increasing DCD.

Lee and Wadsworth [76] also investigated microfiber nonwoven polyether based TPU webs of shore hardness 79A and 80A respectively. The webs were processed on UTNRL's 20 in line equipped with an Exxon style die of 30 holes/in at a diameter of 0.368 mm. They found melt blowing TPUs to be much more complicated than

35

processing PP due to much narrower range of processing conditions which produce high quality webs. They found average fiber diameter to increase with increasing DCD when die temperature and air flow rate remain constant. This is fundamentally different than the trends PP webs show under similar circumstances [73,74]. They also found average fiber diameter decreased by approximately 8 um with increase from ~ 123 scfm to ~150 scfm air flow rate for the polymer with 79A shore hardness. Fiber orientation in the web was also found to increase in the machine direction with increasing DCD. Again, this is the opposite of what they found with PP [74]. They observed that the fiber entanglement increased with increasing DCD.

Zapletalova [77] investigated melt blown polyether based TPU melt blown webs of 80A, 90A, and 98A shore hardness respectively. The webs were processed at North Carolina State Research Center (NCRC) though die characteristics were not discussed, the polymer flow rate was maintained at 0.5 g/hole/min. Webs were collected under the same air flow rate at different DCDs. They found all webs produced, no matter shore hardness, had an average fiber diameter of ~ 5 microns with similar distributions. The polymer intrinsic viscosities decreased 75 to 80% after processing. Web breaking strength and break elongation decreased with increasing DCD. The effect of decreasing polymer shore hardness was found to decrease breaking strength and increase breaking elongation.

Bergenir [78,79] investigated polyether and polyester TPUs and PEBA of various shore hardness's. The webs were processed at NCRC using a slot die with 535 holes having 0.381 diameter. TPU webs were processed at 0.5 g/hole/min while PEBA at 0.24 g/hole/min. They investigated the crystallization rate, finding it to be dependent on the relative concentration of the hard and soft segments under similar cooling conditions and increasing with polymer hardness. The PEBA webs showed decreasing web strength and elongation with increasing hardness while the TPU webs showed increases with increasing hardness. The strength of the two softer PEBA webs remained almost constant with increasing DCD while the highest shore hardness web showed significant

decrease and elongation. The TPU webs breaking strength and elongation decreased over the entire DCD range investigated.

PLA melt blown webs were investigated by Gazzola [80] for use in tissue scaffolds. Nano and microfiber webs were processed on UTNRL's six inch research line. An in depth study was conducted involving web crystallization, strength and pore size for different processing conditions. Liu [81] studied the filtration performance of PLA melt blown webs. Interestingly, they found average fiber diameter to increase with increasing die temperature and air gap width. Chen [82] processed PBT webs and formulated a model to predict average fiber diameter.

In this research, we will investigate properties of melt blown nonwoven aromatic hard segment based and polyether and polyester soft segment based TPU's of different shore hardness collected at multiple air flow rates and DCDs. One web will be used for reinforcement with nanoparticles.

CHAPTER 3: OBJECTIVES AND METHODS

3.1: Introduction

The primary function of a bullet resistant vest is to stop the projectile therefore the materials utilized in the vest construction are chosen based on their ability to contribute to that function. While the current high performance fibers have high strength and moduli, they are brittle and have poor viscoelastic properties. These fibers are highly efficient at preventing penetration. Conversely, they are not as efficient in absorbing and dissipating the remaining kinetic energy after the projectile has been stopped or from shockwaves generated by explosive blasts.

As discussed previously, polyurea and polyurethane elastomers have displayed outstanding energy dissipation capabilities [34, 38–56]. Polyurethane foams have long been utilized as damping materials for the auto industry and are also incorporated into the ACH combat helmet shown in Figure 10 [83 – 88]. Other forms of polyurethane such as injection molded parts, fibers, and films have also shown excellent damping ability [89-93].

Composite materials are designed to achieve unique mechanical properties and superior performance characteristics, not possible with traditional materials. The need for high strength, high stiffness and lightweight materials for structural applications has increased the use of composites in high performance applications like aircraft, land-based vehicles and armor. Many researches have shown that addition of nanoparticles and nanofillers can greatly increase the inherent damping ability of polyurethane materials. Hwang [94], Mackintosh [95], Xia [96], Tzong [97], and Chen [98] have all shown polyurethane strength and damping ability can be improved with addition of carbon nanotubes. Other nanoparticles such as graphene, cellulose nanocrystals, and silica have also been shown to improve damping in polyurethane [99-101].

Multi-layered sandwich composites may be engineered to absorb and dissipate shock energy by using elastic materials such as TPU nanocomposites which exhibit damping

properties. In addition, fibrous composites composed of nonwoven webs have an ability to disperse the shock energy over a large area due to their high degree of fiber-to-fiber contacts and their small fiber diameter. The web structure can also be tuned to capture and hold high modulus reinforcing nanoparticles which increase the composite strength and provide additional surface area for shockwave interaction. A layered nonwoven composite system fabricated with high pressure at low temperatures can yield densified nanoparticle reinforced fibrous structure engineered for maximum energy dissipation at high frequencies or time.

This research is aimed at designing and fabricating elastic sandwich nanocomposites to use as a layer behind the current anti-ballistic armor to minimize the transfer of energy to the underlying individual. The approach has been to reinforce thermoplastic polyurethane nonwoven webs with nanoparticles consisting of nanoclay, graphite, C60, POSS, and tungsten disulfide multi-walled nanotubes (INT). Whereas TPU polymers have high-energy absorption, this can be enhanced by reinforcing with nanoparticles that have high modulus and energy absorption capability.

To exploit these characteristics, studies are performed by physically dispersing nanoparticles into preformed TPU microfiber melt blown nonwoven webs and melt blowing webs with compounded TPU/nanoparticle blends. The webs are then fabricated into sandwich composites by compression molding. Methods will be utilized such that these nanofiller infiltrated fabrics will have a fairly uniform distribution and dispersion of nanoparticles in the matrix. These sandwich nanocomposites are designed to exploit the energy dissipation capabilities of the raw materials and the composite design. Some possible energy dissipation mechanisms consist of: strain induced phase transition, high frequency of the hard segments, viscous dissipation of the soft matrix, interaction with nanoparticles, nanoparticle mechanical properties, strain dispersion of the nonwoven fibers, friction at the nanoparticle/polymer interface, and the sandwich layer interfaces and delamination processes.

3.1.1: Objectives

Project Objective: The overall project objective is to develop potential shockwave absorbing protective panels which can be used as a liner in conjunction with current antiballistic materials to minimize shockwave induced trauma soldiers experience from ballistic impacts and/or blast exposure.

Research Objectives:

1. Understand the influence of Melt Blowing behavior and property development of TPU nonwoven microfiber webs and optimize process parameters. This includes investigation of the:
    a. Influence of Ether and Ester based resins
    b. Influence of shore hardness
    c. Influence of die-to-collector distance (DCD)
    d. Influence of Air Pressure
2. Develop Processes for Dip and Spray Coating and optimize those processes to investigate different nanoparticle add on wt%
3. Melt Blow compounded TPU/Nanoparticle blends to understand process behavior and characteristics of nanoparticle loaded TPU nonwoven webs
4. Identify the nanoparticle and method of introducing nanoparticles to the TPU nonwoven web which should be investigated for high strain rate performance.

3.1.2: Approach

Ether and ester based soft segment thermoplastic polyurethane of various shore hardness are melt blown into microfiber webs with one being chosen for the reinforcing procedures.   The chosen web is reinforced with nanoparticles by dip and spray coating methods. The selected TPU is also compounded with C60 fullerene and melt blown into nonwoven TPU/C60 webs. The reinforced webs from the 3 strategies are then fabricated into multi-ply sandwich composites. A flow chart for the process is shown in Figure 25.
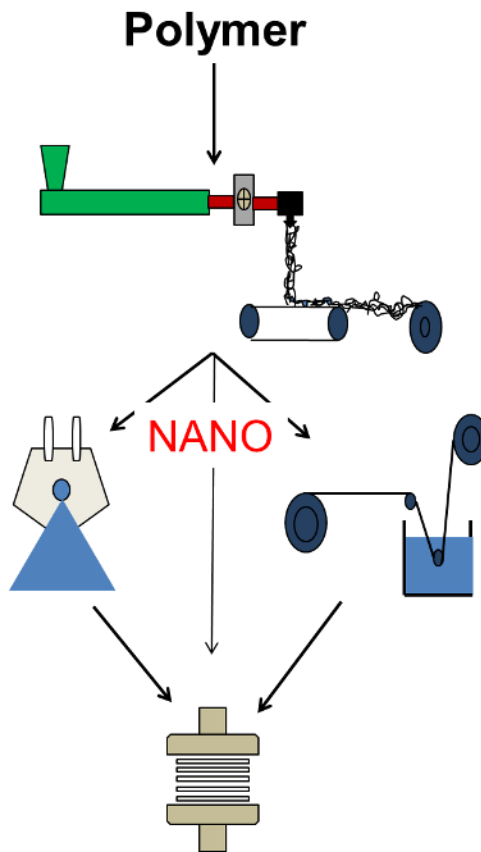
Figure 25. Schematic for melt blown nonwovens and nanofiller incorporation by dip coating and ultra-sonic spraying.

3.2: Materials

3.2.1: Lubrizol Estane TPU

Estane 58315, 58219, 58271, 58277 and Estane ETE 55DT3 and 60DS3 TPU elastomers provided by Lubrizol, Inc. were used in processing melt blown nonwoven webs. All of the TPUs have aromatic based hard segments. The 58000 series consists of 2 polyether-based soft segment TPUs and 2 polyester-based soft segment TPUs with matching shore hardness of 85A and 92A. The ETE (Easy to Extrude) TPUs consist of a polyether-based soft segment TPU with shore hardness of 55D and a polyester-based soft segment based TPU of shore hardness 60D. Within this study, ether and ester series will be denoted as *Txxh* and *Sxxh*, respectively, where T and S represent ether and ester based soft segments while the *xx* represents the shore hardness and *h* represents the shore hardness scale letter.

Estane 58215, an aromatic based hard segment and polyether-based soft segment TPU of 90A shore hardness was used for reinforcing with nanoparticles. It was chosen after analysis of the results for the melt blown webs of the TPUs detailed previously.

3.2.2: Nanofillers

Nanoclay

The most common type of nanoclay used for reinforcement is montmorillonite (MMT) as it is readily available in large quantities at low cost, and its chemistry is well understood. Montmorillonites belong to the family of 2:1 smectic minerals whose layers are composed of two tetrahedral sheets linked to an octahedral sheet [102]. Stacking of the layers occurs through weak van der Waals forces and can be broken up by intercalation into individual sheets having a high aspect ratio of around 1000 that can be subsequently dispersed in the polymer matrix for reinforcement. The d(001) spacing of

42

montmorillonite, comprising the platelets separated by an interlayer called the gallery, can vary over a wide range from a minimum distance of 0.95 nm which corresponding to the fully collapsed state [103]. Usually montmorillonite has negative charges on the interlayer gallery walls, in which cations such as $Na+$ or $Ca2+$ can be absorbed. To reduce the polar characteristic of the silicate, cation exchange reactions are used with various organic modifiers to render the hydrophilic silicate surface at least partially organophilic. Also, ion exchange advantageously increases the initial gallery spacing at the same time as improving compatibility with non-polar polymers. Generally the structure of nanocomposites can be differentiated by the degree of dispersion of the layered silicates [104]. Layered silicates can assemble into tactoids, which are relatively large aggregates in the polymer matrix and thus resemble an immiscible phase as in a conventional microscale composite. Intercalated structure indicates that a single polymer chain diffuses into the galleries between the layers, resulting in formation of alternate layers of polymer and inorganic mineral [105]. In the ideal exfoliated structure, the silicate layers are completely opened up and dispersed disorderly and uniformly in a continuous polymer matrix [106].

Cloisite 30B, a alkyl quaternary ammonium salt bentonite nanoclay, donated by Southern Clay Products Inc. was used in this research. The nanoclay consists of organically modified nanometer scale, layered magnesium aluminum silicate platelets. The silicate platelets that the additives are derived from are 1 nanometer thick and 70 – 150 nanometers across [107]. Figure 26 shows the structural change of nanoclay particles with exfoliation.
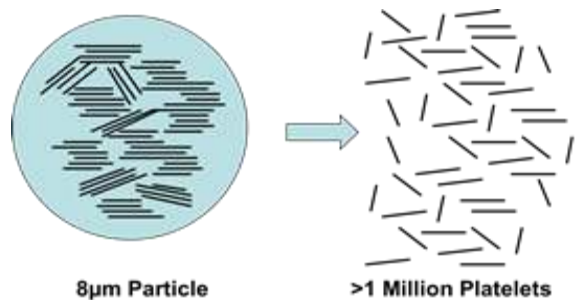
Figure 26. Dispersion and exfoliation of nanoclay. [106]

Graphite

Synthetic graphite powder was purchased from Sigma Aldrich. The particle size was less than 10 microns. The graphite powder was exfoliated by a high power sonication treatment to achieve nanoscale graphene powder. The resulting powder was found to consist of nano and meso sized graphite sheets and platelets. The structure of a graphite platelet is depicted in Figure 27.
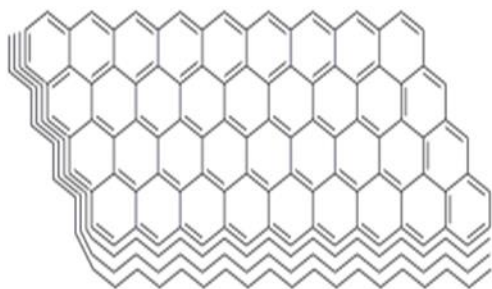
Figure 27. Graphite Structure.

Carbon 60 Fullerenes

Carbon 60 fullerene was purchased from *SES Research*. C60 fullerene consists of 60 carbon atoms aligned in a sphere made up of many carbon rings. (Figure 28) Due to the shape and inherent nature of the C60 sphere, incorporating them in composite materials can impart energy dissipation qualities. During the shockwave propagation, the C60 is put under an influx of pressure, and the spheres respond by contracting and expanding with the pressure, allowing a great deal of the energy to be absorbed and dissipated. The C60 have a mean sphere diameter of 68.3 nm and sphere outer diameter of 101.8 nm. [108]
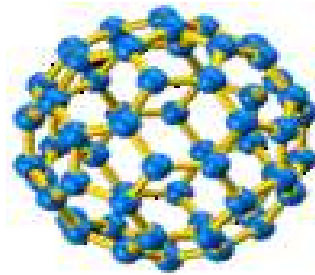
Figure 28. Fullerene C600 structure. [108]

POSS

Methacrylate Isooctyl Polyhedral Oligomeric Silsesquioxane (POSS) was purchased from Hybrid Plastics. (Figure 29) As received, it is a clear colorless oil. The POSS molecule contains a basic polyhedral silicone-oxygen nanostructured skeleton cage structure. It may have 8 or 12 Si atoms surrounded by 8 or 12 organic groups. This particular POSS has 8 Si atoms located at the corners surrounded by 12 oxygen atoms. There are 7

45

individual iso-octyl groups bonded to Si for compatibility and a polymerizable methacrylate functional group for interaction with polymers and surfaces.

R = i-octyl
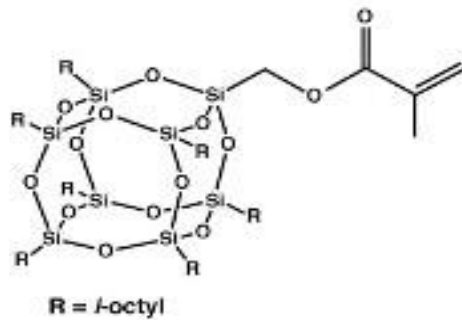
Figure 29. Methacrylate Iso-octyl POSS structure. [109]

Tungsten Disulfide Nanotubes

Tungsten disulfide multi-wall nanotubes (INTs) were purchased from ApNano. They are needle-like particles with a large aspect ratio (width: length = 100: 15) with mean outer diameter of ~100 nm and a length of ~15 nm. INTs exhibit excellent shock absorbing properties and impact resistance [110]. They have shown resistance to shockwave pressures > 21 GPa. [110] An SEM image of a single INT is shown in Figure 30.
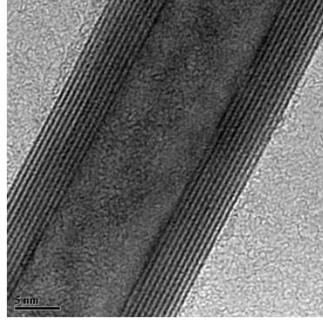
Figure 30. Tungsten Disulfide multi-walled nanotube. [110]

3.3: Melt Blowing

3.3.1: Ether and Ester based TPU Screening

The TPU nonwoven webs were processed on the University of Tennessee Nonwovens Research Laboratory (UTNRL) horizontal six inch research melt blowing line. The processing line consists of a 4 zone single screw extruder (1.5 in. diameter and 33 in. screw length), positive-displacement 10 cc/rev Zenith metering pump, an Ingersoll-Rand SSR-2000 air compressor, 2 air heaters in series, and a belt collector with vacuum. An image of the melt blowing line is shown in Figure 31a. A 5.24 cm (6 in.) Exxon style die with a 60° nose angle, 20 holes/in at 0.457 mm (0.018 in.) diameter, and die setback and air gap of 1.52 mm (0.06 in.) was used in processing. Prior to processing, all polymers were dried at 105 ° C in a Compu-Air humidifying dryer for 3-4 hr. to achieve moisture content below 0.02%. Starting temperatures of the process were determined by analysis of DSC and MFR results. In melt blowing, it is vital to start at temperatures relatively close to optimal processing temperatures to avoid die clogging. Clogged die orifices create webs with poor web quality and consequently, the system must be shut down to remove the clogged die for burn out procedures. Once the process was begun, the extrusion temperatures were adjusted to maintain die pressures in the range of 300 – 500 psi (2068 – 3447 kPa) and allow equal comparison of the processed web properties.   Air

47

temperatures were adjusted in accord with die temperature. The process conditions for each polymer are shown in Table 3. The polymer throughput was maintained between 0.67-0.68 g/hole/min and the collector speed was adjusted between 8.5-8.7 m/min to produce melt blown microfiber webs of 80 g/m^2. The webs were collected at die-to-collector distances (DCDs) of 20, 30, and 50 cm. and at air pressures of 20 and 25 psi (137 – 172 kPa) to give a good representation of the effects of DCD and air pressure (comparable to air flow rate) on the web properties. Figures 31b and 31c show fibers exiting the die and being collected on the winder.

Table 3. TPU Melt Blowing Conditions

Polymer	ID	Extruder Temp. (°C)	M.P. Temp. (°C)	Die Temp. (°C)	Air Temp. (°C)
55DT3	T55D	215, 260, 255, 245	230	230	250
58219	T92A	205, 220, 230, 230	230	225	238
58315	T85A	200, 230, 230, 225	240	220	225
60DS3	S55D	215, 245, 240, 245	255	245	250
58277	S92A	205, 225, 230, 230	230	230	235
58271	S85A	180, 190, 200, 200	210	190	190
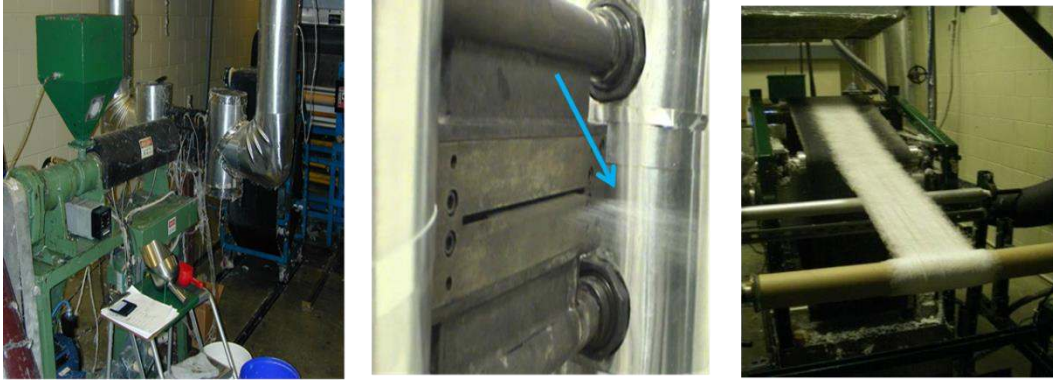
Figure 31. (a.) Single screw extruder. (b.) Fibers exiting the die. (c.) Web being collected on the bobbin.

3.3.2: TPU Web for Nanofiller Reinforcing

From the melt blowing trial of 80 grams per square meter basis weight (areal weight) webs, it was determined by taking into account a combination of ease of processing, web properties, and characteristics (Tg) that a TPU with shore hardness between 85A and 92A would likely exhibit the qualities desired. Estane 58215 of 90A shore hardness was chosen for nanoparticle solution coating methods and melt blowing compounded TPU/C60 blends. This polymer was not included in the melt blowing trial of TPUs previously discussed though there was experience with this polymer previously. It will be referred to as T90A.

Webs of 100 g/m^2 basis weight were melt blown on the UTNRL six inch research line. The processing parameters are listed in Table 4. The webs were collected at a DCD of 40 cm with an air pressure of 35 psi. Die pressure was maintained at approximately 500 psi (3447 kPa) during processing. The throughput was maintained at 0.83 g/hole/min (ghm), marginally higher than the first melt blowing trial and comparable to commercial

production rates. It should be noted that the throughput (0.67 – 0.68 g/hole/min) in the screening trial was limited to what was attainable for the shore hardness D polymer.

Table 4. Melt blowing conditions for TPU T90A shore hardness webs for nanofiller coating reinforcement.

Extruder Temp. Zones (°C)	Die Temp. (°C)	Air Temp. (°C)	Air Pressure (psi)	Throughput (g/hole/min)	Collector Speed (m/min)	Basis Wgt. (gsm)	DCD (cm)
230, 260, 250, 230	230	260	35	0.83	5.2	100	40

3.3.3: TPU/C60 Compounded Blends

The C60/TPU masterbatch was prepared at 0.5 wt% loading (4 kg TPU pellets, 20 g C60). In an attempt to increase C60 nanoparticle dispersion in the compounded masterbatch, a unique spray coating method was developed utilizing nickel plated aluminum and steel air atomizing sprayers purchased at McMaster-Carr. A flow chart of the process is depicted in Figure 32. The TPU pellets were divided into four 1 kg batches and spread evenly into 20 x 14 x 2 in. baking pans. The C60 nanoparticles, in four 5 g. batches, were dispersed into four 1 L volumes of toluene, a concentration of 5 mg/mL. The individual volumes were put under magnetic stir for 5 min followed by sonication treatment at 42 kHz for 30 min before filling the 32 oz. steel air atomizing sprayer. The sprayer was shaken periodically during spraying to maintain dispersion of the particles in the solution. Each TPU batch was sprayed with 1 L of C60/toluene solution. Prior to spraying the C60/toluene solution, DMF was misted onto the pellets followed by mixing to cover the entire pellet surface. The pellets were then allowed to sit for 5 minutes to allow for swelling of the pellet surface. This allowed the C60 nanoparticles to be absorbed into the outer layers of the individual pellets once dried. The process was

repeated 4 times to attain the desired 0.5 wt% loading. The 4 kg of C60 spray coated pellets were allowed to air dry for 1 week with periodic mixing under a laboratory vacuum hood.

Neat TPU Pellets → DMF Misting (mix) → 5 min → C60 Spraying (mix) → Drying (mix)
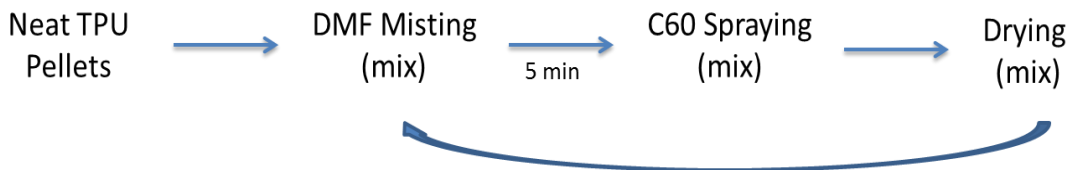
Figure 32. Illustration of TPU/C60 masterbatch preperation.

The coated pellets were dried at 105 ° C in a Compu-Air humidifying dryer for 3-4 hr. to achieve a moisture content below 0.02% and remove all toluene. The dried resin was sealed in an air tight bag until compounding. The compounding of the master batch was performed at Techmer PM in Clinton, Tennessee. Briefly, the dried C60 sprayed pellets were fed through a twin screw extruder and the extruded filament was quenched in a water bath and then pelletized. Out of the initial 4 kg, 2270 g. was returned.

The 0.5 wt% C60/TPU masterbatch was further diluted down to 0.1 and 0.3 wt% by mixing with neat polymer then melt blown into microfiber nonwoven webs of 100 g/m^2 basis weight. UTNRL's six inch research line was used again. For this melt blowing trial, the metering pump was removed as a precaution to avoid system clogging and particle agglomeration. A 5.24 cm (6 in.) Exxon style die with a 60° nose angle, 7.87 holes/cm (20 holes/in) at 0.635 mm (0.025 in.) diameter, and die setback and air gap of 1.52 mm (0.06 in.) was used in processing.

The processing parameters for the TPU/C60 blends and control webs are presented in Table 5. Loaded C60/TPU webs of 0.1 and 0.3 wt% along with neat TPU webs for controls were all processed at the same temperature and throughput parameters. The

51

screw speed had to be increased from 16 rpm for the neat samples to 18 rpm for the loaded webs in order to maintain throughput (0.55 ghm) throughout the trial. Despite this, the die pressure in the extruder remained between 130 and 150 throughout processing. Collection speed was maintained at 4.36 m/min to produce webs of 100 g/m^2 basis weight. Webs were collected at DCDs of 20, 30, and 40 cm to investigate nonwoven properties of the 0.1 wt% and neat materials. The 0.3 wt% batch was only collected at a DCD of 30 cm due to lack of compounded polymer. It was found that high quality webs could only be obtained at a narrow air pressure range, 16 – 19 psi, thus a pressure of 19 psi was utilized in this study.

Table 5. Melt Blowing parameters for compounded TPU/C60 blends and control (neat) samples.

Extruder Temp. Zones (°C)	Die Temp. (°C)	Air Temp. (°C)	Air Pressure (psi)	Throughput (g/hole/min)	Collector Speed (m/min)	Basis Wgt. (gsm)
220, 240, 230, 230	220	274	19	0.55	4.36	100

3.4: Nanofiller Reinforcing Strategies on Preformed Webs

3.4.1: Dip Coating Strategies

Continuous Dip Coating

A Mathis Coating/Padder/Dryer (Figure 33) was utilized in continuous dip coating of T90A webs of 30 gsm basis weight with Cloisite 30B nanoclay. The system consists of 2 nip pressure rolls, drying oven with vacuum, and winding system with collection speeds

ranging from 0.1 m/min to 2 m/min. Equations (1) and (2) were used to determine the
solution concentration needed to achieve a specific loading of nanoclay.

$$\% \ wet \ pickup \ of \ web = \frac{wet \ wgt}{dry \ wgt} * 100 \qquad\qquad (\ 1\ )$$

$$\% \ concentration = \frac{\% \ add \ on}{\% \ wet \ pickup} \qquad\qquad (\ 2\ )$$

Figure 33. Mathis Coater/Padder/Dryer System

Webs were loaded at 1, 3, and 5 wt% on the 30 g/m^2 (gsm) web by coating in
concentrations of [0.0015], [0.0046], and [0.0077], respectively. The pentanol/30B
solutions were sonicated at 42 kHz for 20 min prior to coating to break up the clay

platelets and disperse the nanoclay evenly in the pentanol. The nanoclay/pentanol solutions were then transferred to an online sonicator and sonicated at 25 kHz during the coating process. This online sonicator was used to prevent settling of the nanoparticle in the solvent thereby allowing high dispersion in the microfiber webs at the desired add on weight percent. Table 6 presents the Mathis operation parameters used during the coating process. The % wet pick up for the 30 gsm TPU webs in pentanol was found to be 650%. Once the webs were run through the sonicating nanoclay/pentanol solution, they traveled through nip pressure rolls then the dryer followed by a final nip pressure and a winding roll for collection.

Table 6. Dip coating parameters for 30 gsm TPU preformed nonwoven webs in nanoclay/pentanol solution

Parameters	30B/Pentanol Solution
% Wet Pick-up	650
Web Run	1.5 m/min
Nip Pressure	0.75 bar
Dryer Temperature	130°C
Dwell Time	36 sec

Individual Dip Coating

Cloisite 30B and carbon-60 fullerene were used in single dip coating 2.5 x 2.5 in. samples of 100 gsm T90A nonwoven webs. Solutions of nanoclay 30B/pentanol and C60/toluene were prepared for 1, 3, and 5% loading of the nanofillers. The mass of each 2.5 x 2.5 in. sample was recorded, and the appropriate mass of nanofiller to achieve the desired add on wt% was weighed out and added to 25 mL of the corresponding solvent. The clay solution was sonicated at 42 kHz for 20 min and the fullerene solutions were sonicated

for 5 min at the same frequency. The 25 mL nanofiller solutions were then poured into a petri dish and allowed to spread evenly. The webs were then carefully placed in the dish and allowed to absorb the solution. The samples were then dried overnight in a chemical hood to allow for complete evaporation of the solvent. Figure 34 shows the system used and samples coated with 1 and 5 wt% C60 as well as a control sample without nanofiller.
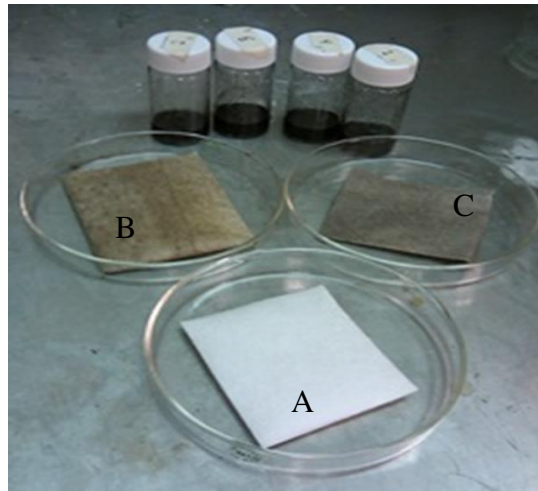
Figure 34. Estane coated with C60/toluene solution. A. Control, B. 1 wt%, C. 5 wt%

3.4.2: Continuous Ultrasonic Spray Coating

A Wide-Track ultra-sonicating spray system was purchased from *Sono-Tek Corporation*. The system is equipped with a 25 Hz stainless steel non-clogging ultrasonic nozzle capable of producing droplet sizes averaging ~55 um. The atomization of the solvent and nanofiller allows for precise control of coating at a specified flow rate, providing for a more uniform dispersion of the nanofiller. Spray widths may range from 2 to 24 inches. The spray system was used in conjunction with a Mathis Coater/Padder/Dryer machine to enable continuous spraying and online drying of the webs after spraying. (Figure 35)

Figure 35. Sono-Tek WideTrack spray system paired with a Mathis Coater/Padder/ Dryer.

As their name implies, ultrasonic nozzles employ high frequency sound waves, those beyond the range of human hearing. The sound waves are created by disc-shaped ceramic piezoelectric transducers which convert electrical energy into mechanical energy. The transducers receive electrical input in the form of a high frequency signal from a power generator and convert that into vibratory motion at the same frequency. Two titanium cylinders magnify the motion and increase the vibration amplitude at the atomizing surface. A schematic of the nozzle assembly is shown in Figure 36b. Nozzles are configured such that excitation of the piezoelectric crystals creates a transverse standing wave along the length of the nozzle. The ultrasonic energy originating from the crystals located in the large diameter of the nozzle body undergoes a step transition and amplification as the standing wave traverses the length of the nozzle. The air delivery system is composed of two air jets. (Figure 36a) They alternate on and off to create a sweeping spray pattern which is uniform and highly repeatable. All components of the WideTrack system are shown in Figure 37 along with a web being sprayed with C60 solution and the same web exiting the dryer.
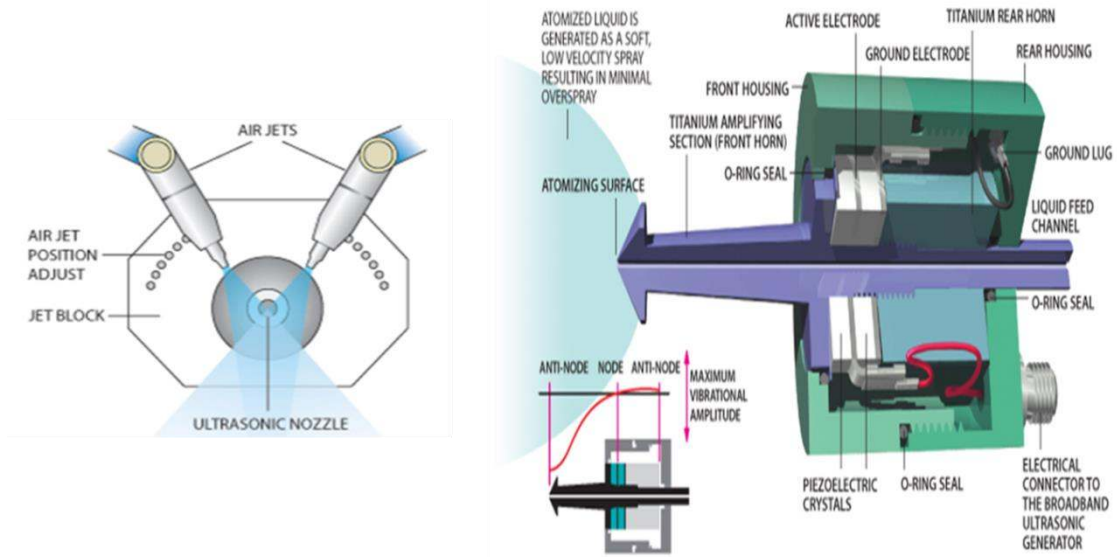
Figure 36. a) Illustration of nozzle and jet block emphasizing positioning of air jets to control spray width. b) Nozzle Construction
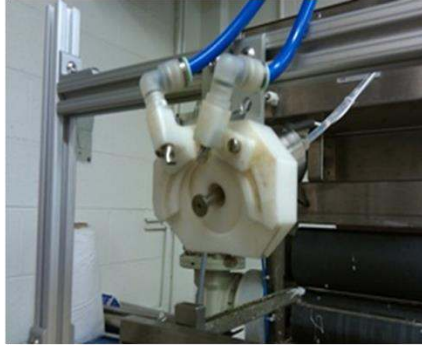
Figure 37. WideTrack Spray System Components.

The operation parameters of the system were determined by simultaneously solving the equations (3) – (6).

$$\textbf{Nanoparticle Feed Rate} = \frac{\textbf{Volume Flow Rate}}{\textbf{Solution Concentration}} \qquad (\,3\,)$$

$$\textbf{Fabric Areal Feed Rate} = \frac{\textbf{Deposition Width}}{\textbf{Belt Speed}} \qquad (\,4\,)$$

$$\text{Nanoparticle Deposition Density} = \frac{\text{Nanoparticle Feed Rate}}{\text{Fabric Areal Feed Rate}} \qquad (5)$$

$$\text{Nanoparticle add on wgt\%} = \frac{\text{Nanoparticle Deposition Density}}{\text{Fabric Basis Wgt}} \qquad (6)$$

Two nanofiller solutions spraying trials with different parameter constants were performed and carried out as follows.

Trial 1

For Trial 1, the nanoparticle solution concentration was kept constant while the volume flow rate (VFR) and belt speed (BS) were varied in order to achieve the desired add on wt% of the respective nanoparticles. The webs were sprayed on both sides, half of the desired add on wt% per side, to achieve totals of 1, 3, and 5 add on wt%. The process parameters are listed in Tables 7 and 8 for C60 and POSS nanofillers dispersed in toluene. Prior to spraying, the solutions were sonicated at 42 kHz for 30 min. The drying oven was set at 65 °C.

Table 7. C60 spray parameters.

C60/Toluene [2.735 mg/ml] concentration			
Total add on wt%	Add on wt% per side	Flow Rate (ml/min)	Belt Speed (m/min)
1	0.5	27.8	1
3	1.5	35	0.418
5	2.5	40	0.287

Table 8. POSS spray parameters.

POSS/Toluene [4 mg/ml] concentration			
Total add on wt%	Add on wt% per side	Flow Rate (ml/min)	Belt Speed (m/min)
1	0.5	25	1
3	1.5	30	0.525
5	2.5	35	0.367

Trial 2

From Trial 1 observations, it was determined that the spray system produced the best nanoparticle dispersion between 25 – 30 ml/min flow rates with belt speed close to 0.5 m/min. For Trial 2, the VFR and belt speed were kept constant while the solution concentration was altered to achieve the desired add on wt% of the respective nanoparticles. The parameters for Trial 2 are detailed in Table 9. The nanofillers sprayed include fullerene C60, graphite, and inorganic tungsten disulfide nanotubes (INTs). The C60 and graphite were dispersed in toluene while the tungsten disulfide INTs were dispersed in ethanol with 15% Wetter D-75E surfactant to aid in keeping the particles in solution. The solutions were sonicated for 30 min at 42 kHz prior to spraying. Unlike Trial 1, Trial 2 solutions were also sonicated at 25 kHz during the spraying process to prevent settling of the nanoparticles while in the spray system reservoir.

Table 9. Spray parameters for Trail 2: C60, Graphite, and INT.

Nanomaterial/Solvent	Concentration (mg/ml) for target add on wt%			Operation Parameters	
	0.20%	0.60%	1%	VFR (ml/min)	BS (m/min)
C60/Toluene	0.610	1.83	3.05	25	0.5
Graphite/Toluene	0.4064	1.219	2.032	30	0.4
INT/Ethanol/15% Wetter D-75E	0.6096	1.829	3.048	25	0.5

3.5: Sandwich Composite Fabrication

Sandwich nanocomposites were fabricated with a Carver hot press. (Figure 38) The webs are all stacked in 0-90° with respect of the machine direction orientations and covered in a Kapton sleeve. Appropriate temperature, time, and pressure parameters were determined by investigation of different combinations of the three parameters with a goal of obtaining complete and durable adhesion while maintaining the fibrous structure of the webs. Choosing the appropriate parameters was done by visual examination for uneven melting, delamination, and DMA testing. The pressing parameters will be reported in the results section of the corresponding sandwich composite.

Figure 38. Wabash Hot Press

3.6: Characterization Methods

The polymers and corresponding melt blown webs were characterized for thermal, strength, viscoelastic, and web structure properties. Sandwich composite characterizations are also incorporated into this section.

3.6.1: Differential Scanning Calorimetry (DSC)

Thermal analysis was carried out using the Mettler Toledo Differential Scanning Calorimetry, DSC821. Samples were first dried under vacuum at 80 °C for 1 hour. All DSC scans were carried out in aluminum crucibles under nitrogen atmosphere at a flow rate of 200 mL/min with samples of 6-8 mg. The scans ran from 25 °C to 220 °C at a heating rate of 10 °C/min, held at 220 °C for 3 min, and then cooled back to 25 °C at a rate of 10 °C/min.

An annealing investigation was performed on the T90A web. DSC samples were prepared and annealed at 90°C and 130°C for four hours to investigate the effect of annealing temperature on the TPU morphology. DSC scans were performed as previously detailed but without the drying step.

3.6.2 Melt Flow Rate (MFR)

Melt flow rates of the TPU polymers were measured with a Tinius Olsen Plastometer Model MP987 (Figure 39) with a load of 2.16 kg per ASTM D1238, Procedure B. The instrument specifications are as follows:

Barrel diameter: 9.55 mm; Barrel length: 162 mm,

Capillary diameter: 2 mm; Capillary length: 8 mm,

Travel length of piston in the barrel: 25.4 mm

Temperatures of 210, 220, 230 °C were utilized. Four readings were taken at each temperature and MFR was calculated using the following equations.

$$Melt\ Density\left(\frac{g}{cc}\right) = \frac{Extrudate\ mass\ (g)}{1.804} \qquad (\ 7\ )$$

where 1.804 cm^3 is the volume of the polymer that will be extruded by 25.4 mm movement of piston in the barrel if the polymer melt density is 1 gm/cc.

MFR is expressed in grams/10 min is calculated using relationship:

$$MFR = \frac{426 * L * d}{t} \qquad (8)$$

Where,

L is the length of the piston travel, 2.54 cm

d is the resin density of the polymer at test temperature (g/cc),

t is the time (sec) of piston travel for length L,

426 is the mean of areas of piston and cylinder x 600.

Figure 39. Tinius Olsen Extrusion Plastometer MP987

3.6.3: Solution Viscosity

Dilute Solution Viscosity is a simple yet useful technique for analysis of polymer systems. The dependence of polymer solution viscosity on concentration and chain size gives an indication of the polymers molecular weight. The measurement of solution viscosity involves use of a constant temperature bath and a capillary viscometer. An illustration of an Ubbelohde viscometer is shown in Figure 40. During measurement, the viscometer is inserted in the water bath which is held at a constant temperature. The polymer solution is forced from the A bulb to the B bulb, and the efflux time for the polymer to flow from time lines B to C is recorded for different concentrations.
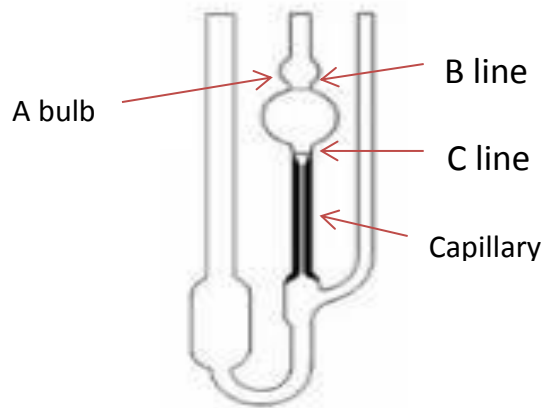
Figure 40. Ubbelohde Viscometer

The solution flow time is proportional to the viscosity and inversely proportional to the respective density.

$$t_{solvent} = \eta_{solvent}/\rho_{solvent} \qquad t_{soln} = \eta_{soln}/\rho_{soln} \qquad (9, 10)$$

Relative viscosity (η_{rel}) is defined as the ratio $\eta_{soln} / \eta_{solvent}$. With a dilute concentration of polymer in the solvent, $\rho_{soln} = \rho_{solvent}$. This allows for the following relationships:

$$\boldsymbol{\eta_{rel}} = {}^{\boldsymbol{t_{soln}}}\!/_{\boldsymbol{t_{solvent}}} \qquad \boldsymbol{\eta_{sp}} = \frac{\boldsymbol{\eta_{soln} - \eta_{solvent}}}{\boldsymbol{\eta_{solvent}}} = \boldsymbol{\eta_{rel} - 1} \qquad (\,11,\,12\,)$$

Specific viscosity (η_{sp}) represents the incremental viscosity from polymer in the solution as seen with the relation with relative viscosity above. The inherent viscosity (η_{inh}) is related to the relative viscosity through the following equation.

$$\boldsymbol{\eta_{inh}} = \frac{\ln \boldsymbol{\eta_{rel}}}{\boldsymbol{c}} \qquad (\,13\,)$$

Like η_{sp}, η_{inh} also represents the incremental viscosity in the polymer solution. By normalizing η_{sp} and η_{inh} with concentration and extrapolating to zero concentration, the intrinsic viscosity can be determined (Figure 41). This is proved by:

$$[\boldsymbol{\eta}] = \lim_{\boldsymbol{c \to 0}} \frac{\boldsymbol{\eta_{sp}}}{\boldsymbol{c}} = \lim_{\boldsymbol{c \to 0}} \frac{\ln \boldsymbol{\eta_{rel}}}{\boldsymbol{c}} \qquad (\,14\,)$$
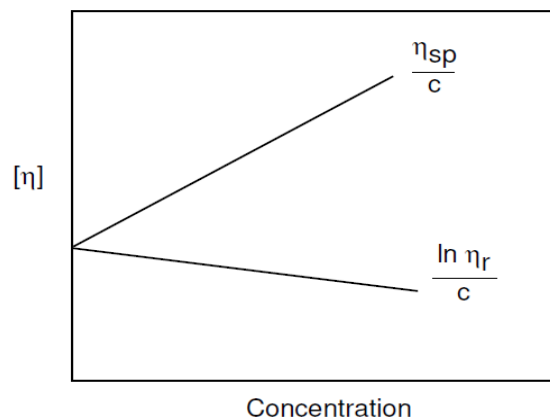
Figure 41. Extrapolation of intrinsic viscosity.

Solution viscosity measurements were taken with a Cannon Constant Temperature Bath (Figure 42) and Ubbelodhe viscometer model OB K361 by Cannon Inc at 30 °C for both raw pellets and webs processed at a DCD/Air Pressure conditions of 30/25 for the 80 g/m^2 screening webs and the T90A 100 g/m^2 web. Solutions of 0.2, 0.4, 0.6, and 0.8 g/dL concentrations were prepared in Sigma Aldrich DMF under magnetic stir.   Each sample was allowed to equilibrate in the temperature bath for 15 minutes prior to testing. The efflux time was recorded for five runs and an average taken for use in plots for determining the intrinsic viscosity.

Figure 42. Cannon Temperature bath CT-1000 with Cannon OB K361 Ubbeholde Viscometer.

3.6.4: Scanning Election Microscope Imaging (SEM)

A Leo Gemini Scanning Electron Microscope was used to image the respective webs and sandwich composites. Samples from 3 different locations in the web were fashioned to a metal post with conductive tape. Two posts were prepared from each sample to obtain a good representation of the webs. All samples were sputter coated with gold for conductivity. Multiple images were taken at different magnifications to analyze web structure.

3.6.5: Fiber Diameter Measurements

Fiber diameters were measured from images taken on a Leo Gemini Scanning Electron Microscope. For each sample, 100 total measurements taken from 3 separate locations across the web and used in calculation of average fiber diameter, standard deviation, and plotting fiber distributions.

3.6.6: Strength and Elongation at Break

Tensile properties of the of 1 layer web samples were determined using a United Tensile tester equipped with a 10 lb load cell per ASTM D5035. Briefly, samples of 1 in. by 6 in size were tested with a gauge length of 3 inches at 12 in/min crosshead speed. Results from 5 samples in the machine direction (process direction) were used to calculate average break force and percent elongation. Results were plotted as functions of DCD and air pressure.

3.6.7: Air Permeability

A TexTest FX3300 Air Permeability Tester (Figure 43) which measures the air flow rate through a 38 cm^2 sample at a pressure drop of 125 Pascal was used to measure the air permeability of each melt blown web per ASTM D737. Ten samples were tested with average and standard deviation calculated.

Figure 43. TexTest Air Permeability Tester

3.6.8: Pore Size

The average pore diameter was determined by averaging results from 3 samples tested with a Capillary Flow Porometer, Model # CFP-1100-AEX. Measurement on the Porometer entails exclusion of a wetting liquid with very low surface tension of 0.0156 N/m from the pores of a completely saturated nonwoven media by pressurized air. When the applied air pressure exceeds the capillary attraction of the wetting liquid in the pores, air will pass through the sample, allowing the determination of the mean pore size. Smaller pores have a higher capillary attraction than larger pores and thus smaller pores open up at higher pressures.

3.6.9: Dynamic Mechanical Analysis (DMA)

This instrument is vital to this research endeavor due to the vast amount of sample combinations fabricated. It will be used to evaluate viscoelastic properties of the sandwich composites in the linear elastic region and as a screening method for choosing the appropriate TPU for reinforcing with nanofillers as well as which sandwich composites merit further investigation with the high cost of high strain rate testing by with Split-Hopkinson Pressure Bar and/or Shock Tubes. Both temperature scans and frequency sweeps will be investigated. Due to the great reliance on this method, more insight into its function is discussed in the next paragraphs.

Dynamic Mechanical Analysis (DMA) is a method used for the characterization of viscoelastic properties of materials. The degree to which a polymer exhibits more solid-like or liquid-like behavior is dependent on temperature as well as time or frequency. DMA applies a sinusoidal force to a sample and the resulting sinusoidal deformation is monitored. The stress at any time is given by the equation:

$$\sigma = \sigma_0 \sin \omega t \qquad (\,15\,)$$

where σ_0 is the maximum stress. The corresponding strain, ε, is given by:

$$\varepsilon = \varepsilon_0 \sin(\omega t - \delta)$$ (16)

A purely elastic material is one in which all the energy stored in the sample during loading is returned when the load is removed. As a result, the stress and strain curves for elastic materials are completely in phase as shown in Figure 44. Elastic materials follow Hooke's Law and the stress in proportional to the strain while the modulus is the ratio of the stress to strain. For a purely viscous material, all of the energy applied during loading is dissipated or lost by conversion to heat once the load is removed. Here the stress is 90° out of phase with the strain and the ratio of stress to strain is known as viscosity (Figure 45).
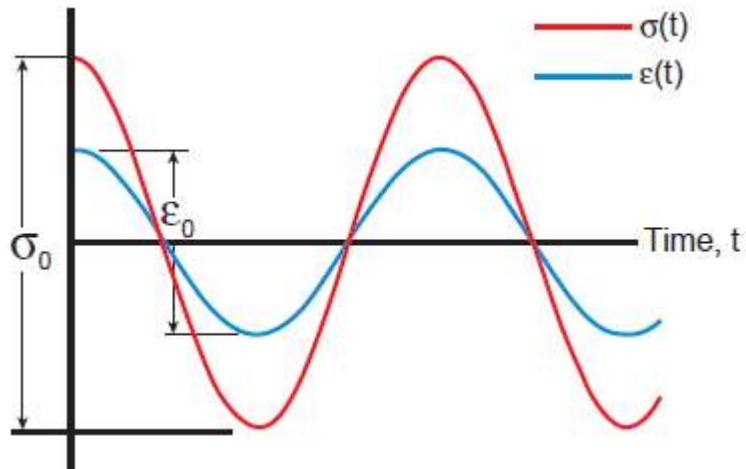
Figure 44. Cyclic stress-strain curve for purely elastic materials showing stress in phase with the strain. [111]
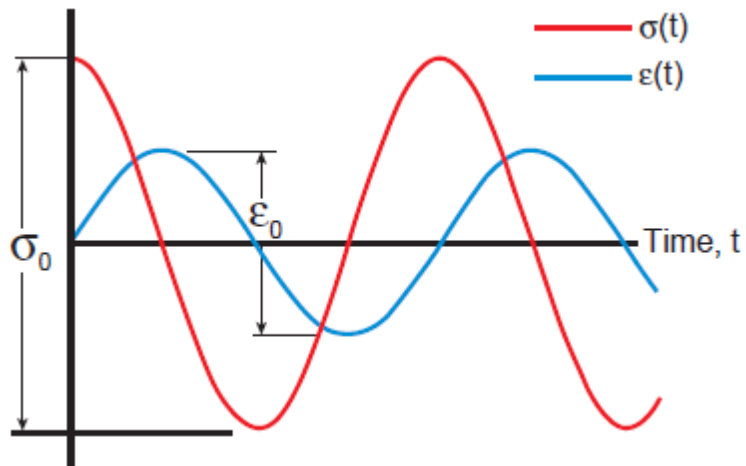
Figure 45. Cyclic stress-strain curve for purely viscous materials showing stress 90° out of phase with the strain. [111]
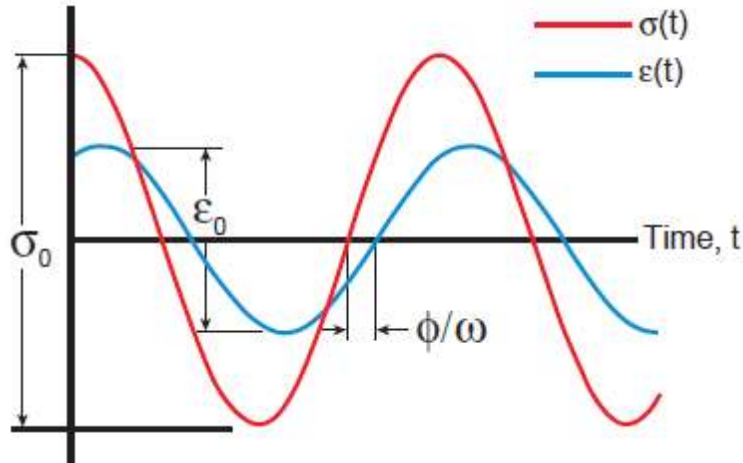
Figure 46. Sinusoidal curve with strain lagging behind the applied stress by the phase angle, δ. [111]

For viscoelastic materials, the sample response lags behind the applied stress wave with respect to time (Fig. 46). This lag is known as the phase angle, δ. The stress can be resolved into two parts, in-phase (elastic) and out-of-phase (viscous) with the strain. The storage modulus (E') corresponds with the in-phase or elastic part while the loss modulus (E") relates the out-of-phase or viscous part with tan δ as the ratio of E" to E'. They are defined mathematically by the following equations:

$$E' = \frac{\sigma_0 \cos \delta}{\varepsilon_0} \qquad E'' = \frac{\sigma_0 \sin \delta}{\varepsilon_0} \qquad \tan \delta = \frac{E''}{E'} \qquad (17-19)$$

The storage modulus (E') refers to a materials ability to return or store energy. For glassy or amorphous polymers, E' is high and lower for rubber or semicrystalline polymers. The loss modulus (E") is associated with the viscous response and represents the energy converted to heat by the molecular motions from the material under stress. Tan delta is the ratio of the E" to E', consequently it behaves much like E" but is

73

independent of sample dimensions. It translates to a measurement of the ratio of energy absorbed by the sample as heat to the energy used by the sample to return to its original shape. The loss modulus and tan delta are indicators of the polymers ability to internally dissipate energy which is why peaks in tan delta are often referred to as damping peaks.

The DMA technique is sensitive to the various transitions which a polymer undergoes as a function of changing temperature and frequency of the applied stress or strain. Viscoelastic materials are typically characterized by the type of behavior shown in Figure 47. They exist in various states or phases over broad temperature and frequency ranges, and the behavior regions are typically referred to as the glassy, transition, rubbery, and flow regions. Viscoelastic materials behave differently based on which region they exist in for a specific application.

In the glass region, the polymer chains are ordered into crystalline domains with the polymer possessing rigid glass-like behavior. Stiffness, E', of the material is at its highest point in this region while the damping, E" and tan delta, are typically low. In the transition region, the polymer is transitioning from a glass to a rubber state. In this region, the polymer goes through its most rapid rate of change in stiffness and possesses its highest level of damping performance. The polymer chains are in semi-rigid and semi-flow states and are able to rub against adjacent chains creating friction. The frictional effects result in the mechanical damping characteristics of viscoelastic materials. In the rubber region, the polymer is above the glass transition and below the melting temperature. The polymer reaches a lower plateau in stiffness and damping is lower. In the flow region also termed the terminal region, the polymer has reached its melting point and the polymer chains slide past each other and the polymer flows.
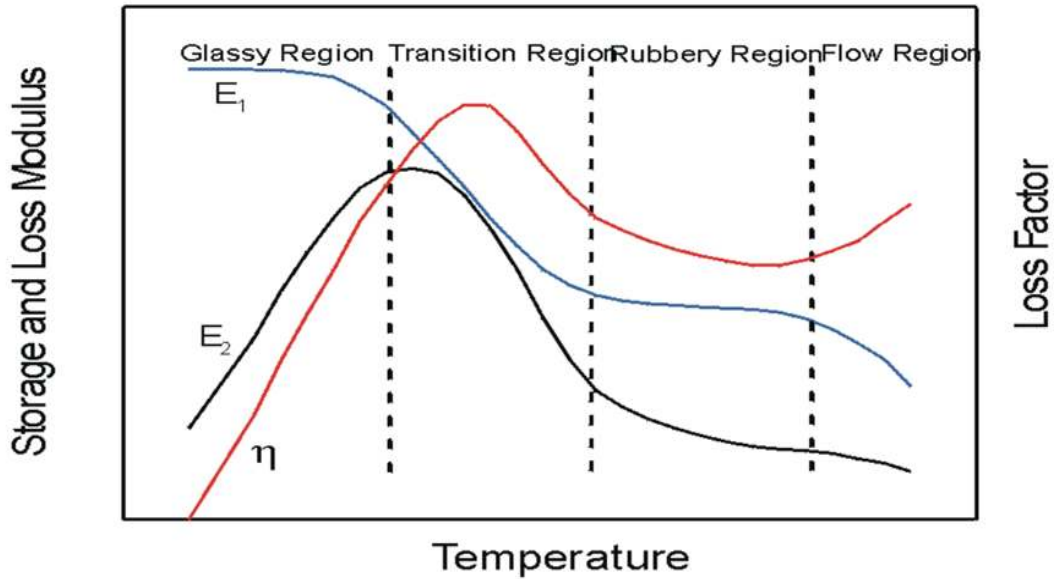
Figure 47. Illustration of storage modulus, loss modulus and tan delta for a polymer in various phases. [112]

The thermal transitions in polymers can be described by changes in free volume changes or relaxation times to supply information for the various segmental motions [111]. Changes in free volume can be monitored as a volumetric change in the polymer by the absorption and release of heat associated with that change, by the loss of stiffness, increased flow, or a change in relaxation time [111]. The free volume concept was developed by Doolottle and is defined as the space within the polymer unoccupied by the polymer chains [113]. The variation of free volume with temperature is shown in Figure 48 where the amount of free volume increases with increasing temperature above the Tg. The slope of the specific volume curve is the coefficient of thermal expansion, CTE, and, in fact, one definition of the Tg is the point at which the coefficient of thermal expansion suffers a discontinuity. The variation in free volume allows for greater mobility of the molecular chains and gives rise to greater time or viscoelastic effects as temperature increases.

75
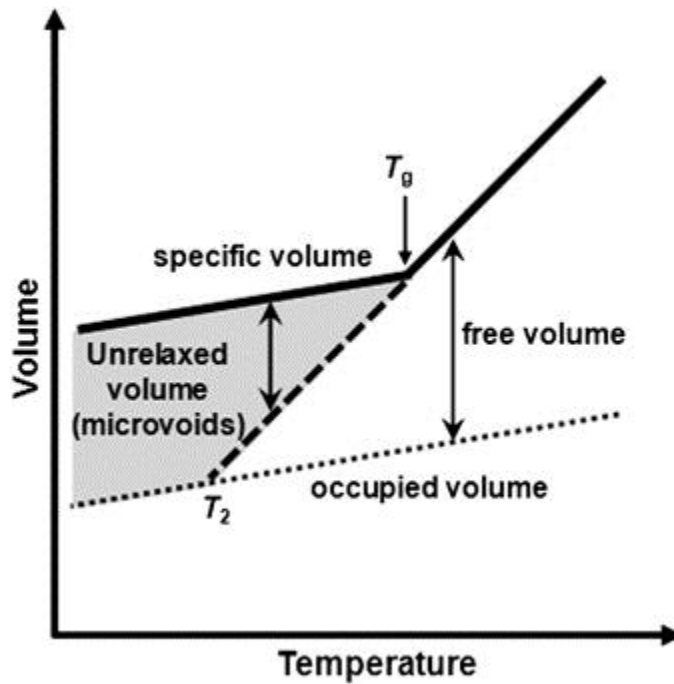
Figure 48. Free volume in polymers as a function of temperature. [94]

A simple approach to looking at free volume is the crankshaft model where the polymer chains are imagined as a series of jointed segments. This model is depicted in Figure 49. Other chain in tube models based on the reptation and Rouse motion of a single polymer chain in solution and the melt proposed by de Gennes [114] and Doi-Edwards [115] which were built off the early pioneering efforts of Kuhn, Rouse, Zimm, and Flory for dilute solutions above the glass transition temperature. Ferry [116] extended the work of Rouse and Zimm to bulk polymer in the rubbery state by utilizing Doolittle's free volume theory and the method of reduced variables.

Stretching Bending Rotating

Coordinated movements Slippage
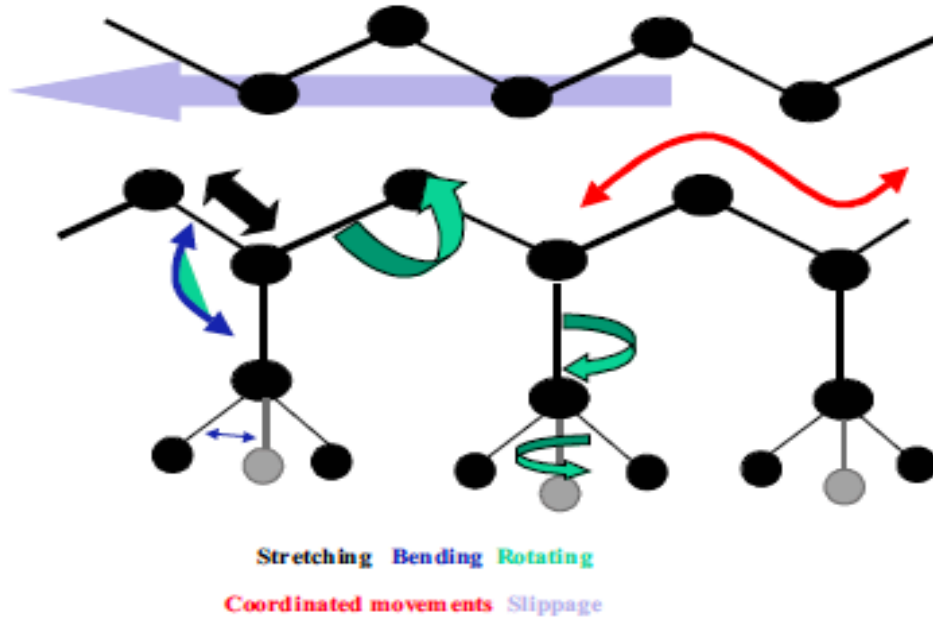
Figure 49. Crankshaft model showing various motions of a polymer chain.

The crankshaft model treats the polymer chain as a collection of mobile segments that have some degree of free movement. As the free volume of the chain segment increases, its ability to move also increases. This increased mobility in either side chains or segments of the chain backbone results in lower moduli of the polymer. Figure 50 depicts transitions which may be seen during a DMA temperature scan at a constant frequency for various types of polymers.
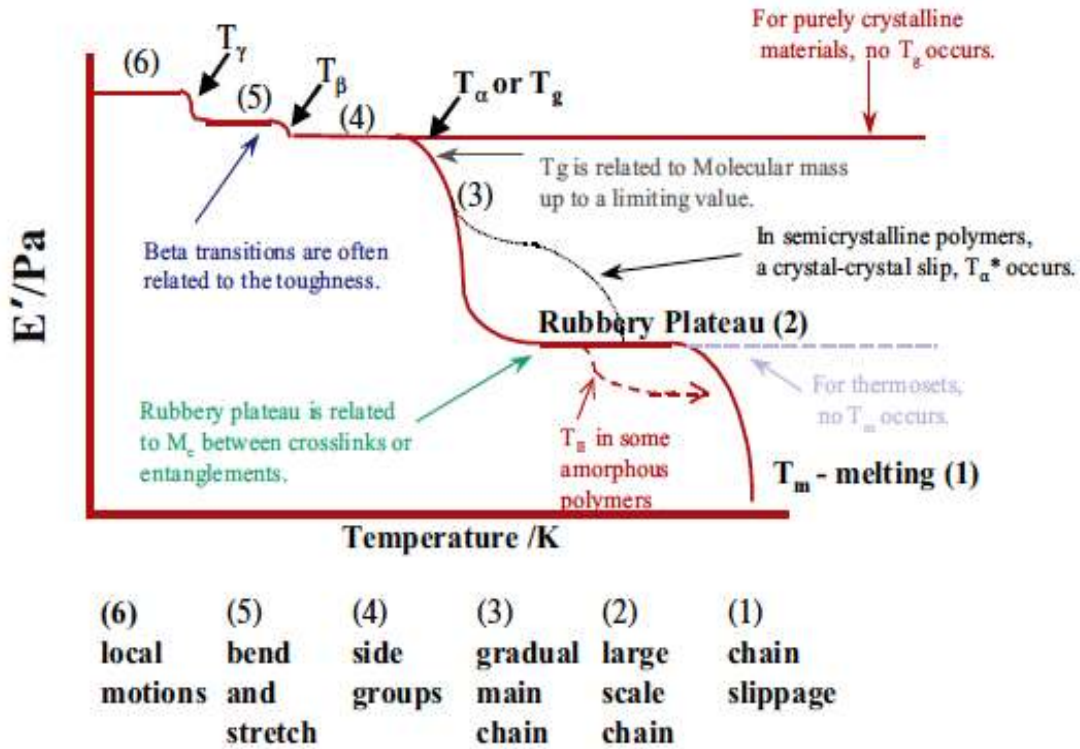
Figure 50. Idealized DMA temperature scan showing possible transitions for different polymer types. [111]

At very low temperatures where the polymer chains are tightly compressed they pass through the solid state transitions. The localized bond movement of bending and stretching and small side chain movements is ascribed as the gamma (γ) transition. As the temperature and free volume increases, whole side chains and localized groups of four to eight backbone atoms begin to have enough space to move and the material starts to develop toughness [111]. Such transitions are called beta (β) transitions. The large scale motions of the amorphous regions as heating increases further are related to the glass (α) transition. The Tg is very dependent on the degree of polymerization up to a value known as the critical Tg or critical molecular weight. The Fox-Flory empirical equation describes reasonably well the Tg dependence on molecular weight [117].

$$T_g\ (M_n) = \ T_g(\infty) - \frac{K}{M_n} \qquad\qquad (\ 20\ )$$

Here Tg (∞) is the maximum glass transition temperature that can be achieved at infinite molecular weight and K is an empirical parameter related to the free volume present in the polymer. The free volume approach explains the Fox-Flory equation, assuming that chain ends contribute an excess free volume. In that case, a decrease in Mn leads to an increase of chain end concentration and increase of free volume. Therefore an increase in free volume leads to decrease in Tg. Above that threshold the rubbery state appears. The modulus in that region is proportional to the number of cross-links or the molecular weight between entanglements, M_e. This is often expressed as

$$E'\sim \frac{(\rho RT)}{M_e} \qquad\qquad (\ 21\ )$$

Here, E' is the storage modulus in the rubbery plateau at a specific temperature (T), ρ is the polymer density, and R is the gas constant. Dependent of the polymer, other transitions may be seen in the region between Tg and the melting point of the polymer as shown in Figure 50.

There are at least five different accepted methods for determining Tg from DMA temperature scans. The peak or onset of the tan delta curve, the onset of E' drop, or the onset or peak of the E" curve may be used. The values obtained from these methods can differ up to 25°C from each other on the same run. In addition, a 10 - 30°C difference from the DSC Tg is also seen in many materials. In practice, it is important to specify exactly how the Tg was determined, including defining the heating rate, applied stress or strains, the frequency used, and the method for determining Tg.

The relaxation spectrum of a polymer may also be analyzed using a frequency sweeps at a constant temperature. These types of scans however are limited to the lowest and highest frequencies attainable by the DMA. Typically, DMA frequencies range from 0.001 to 100 Hz. This range is generally not great enough to cover the entire range of the relaxation spectrum. In these cases, the William-Landel-Ferry (WLF) equation is employed to exploit the equivalent relations of high temperature-low frequency and low temperature-high frequency aspects of viscoelastic materials relaxations [116].

$$\log a_t = \frac{-C_1 \, (T - T_0)}{C_2 + T - T_0} \qquad (22)$$

Here, a_T is termed the horizontal shift factor, C_1 and C_2 are empirical constants used to fit the values of the superposition parameter a_T. T_0 is the reference temperature and usually taken as Tg of the polymer. To employ the WLF equation, multiple frequency sweeps are employed at different temperatures and a master curve is constructed for a particular reference temperature. This is termed the Time-Temperature Superposition Principle (TTS). A typical master curve is shown in Figure 51. The relaxation time of the material may be taken for the crossover point of E' and E" and the reciprocal of the frequency at that point.
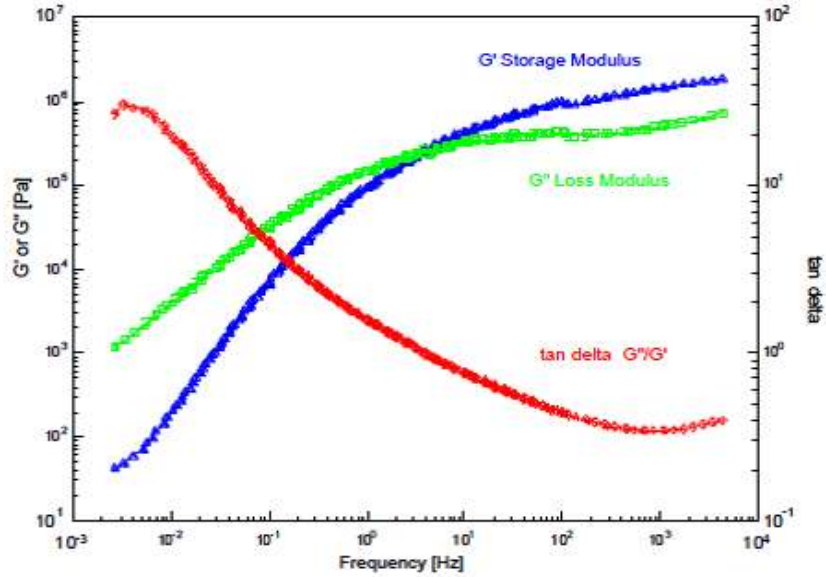
Figure 51. Master curve generated form the WLF equation.

The materials in this research were tested by DMA with frequency sweeps in tensile mode from 1 – 100 Hz at 25 °C with 0.1% strain applied. A Rheometric DMTA V and a TA Q800 DMA were utilized. No discrepancies in the results were found using two different instruments. Three samples of each material were tested and averages of the three are reported. Sample dimensions were 10 mm in length and 5 mm in width. The TA Q800 was also used to conduct temperature scans in tensile mode from -100 to 60 °C at a heating rate of 3°C/min and at 1, 10 and 100 Hz. The 1 Hz frequency curves showed a lot of noise due to relaxation of the stress over the sample and are not presented. Two samples of each material were tested to ensure repeatable results within a sample lot. Sample dimensions were 10 mm in length and 5 mm in width. The glass transition of the materials is taken as the peak of the tan delta curves.

3.6.10: Densification

Sample bulk density measurements were performed by cutting samples to 3 cm length and 3 cm widths. Thickness and mass were then measured using a TMI thickness tester Model 49-70 and a Mettler Toledo micro-balance to calculate the bulk density.

3.6.11: Fracturing

To investigate the fracture mechanics, samples were dropped into liquid nitrogen and allowed to sit for one minute. The samples were then removed and fractured. The fractured surface was examined by Scanning electron microscope imaging.

3.6.12: Mini-Shaker

High frequency vibration testing of the 4 layer sandwich composites was performed under continuous excitation with a mini-shaker at the University of Alabama-Birmingham by members of Dr. Uday Vaidya's research group. The instrument set-up is presented in Figure 52. The sample dimensions were 4 inches in length and 0.5 inches in width and supported by lightly bonding with a spray adhesive to a Teflon beam. The samples were mounted in a free-free edge support condition by mounting at their center and directly over the impedance head with double-sided tape.
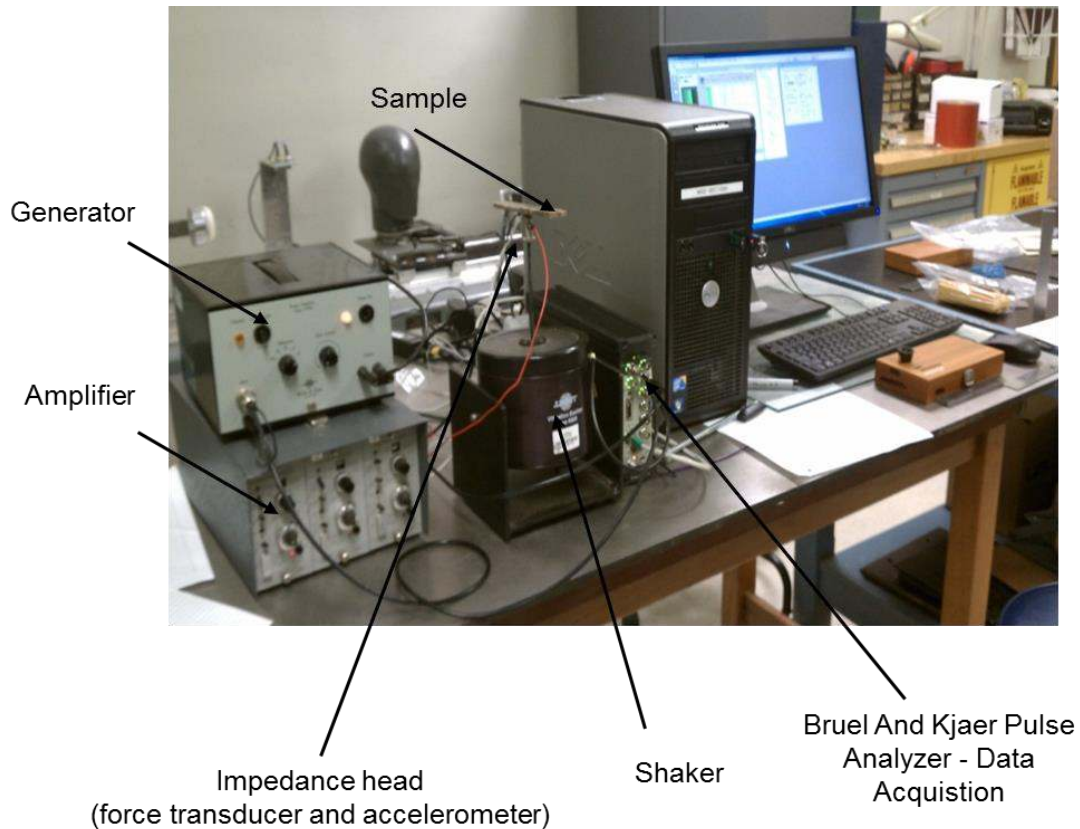
Figure 52. Mini-Shaker setup

The instrument operates by applying a random noise excitation through a noise generator which is amplified by a power amplifier to excite the Bruel and Kjaer Type 4809 electrodynamic shaker. A Bruel and Kjaer Type 4000 impedance head mounted over the stinger rod of the shaker measures input force and output acceleration. The vibration response was measured using a dual channel Bruel and Kjaer Pulse Analyzer after the signal is amplified by two Kistler-Type 5004 dual mode preamplifiers. The frequency response function (FRF) is plotted against frequency to get the baseband response. Damping is measured by zoom transform at each frequency and the damping ratio by the half was calculated power bandwidth method also known as the -3dB drop method as shown in Figure 53. Results are presented as baseband resonance frequencies as a function of amplitude and damping ratio as a function of resonance frequency.

$$\zeta = \frac{f_2 - f_1}{2f_n}$$
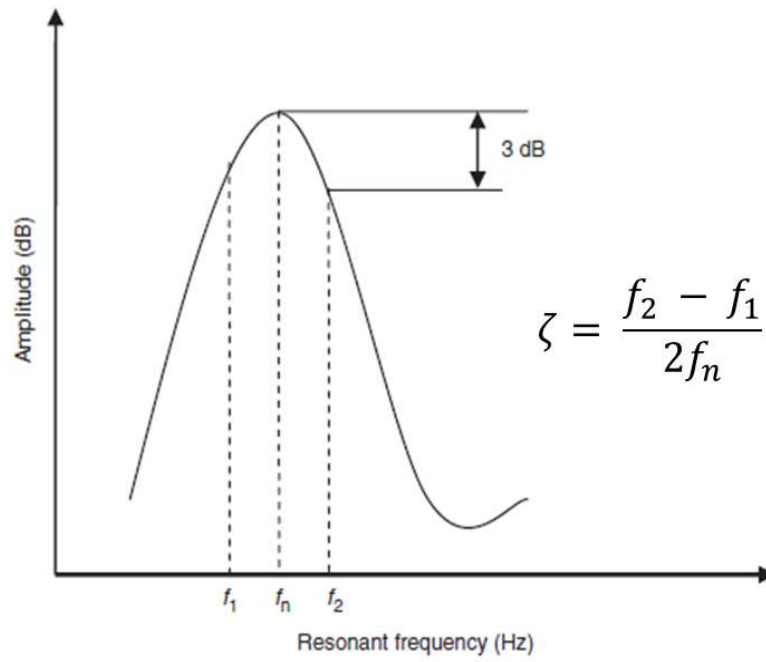
Figure 53. Half power bandwidth method (-3dB method)

CHAPTER 4: MELT BLOWING AND COATING RESULTS

4.1: Ether and Ester based TPU Screening

4.1.1: Determination of Process Parameters

DSC scans and melt flow rates were used to determine starting melt blowing process temperatures for the extruder, metering pump, die, and air temperature. The DSC melting curves are shown in Figure 54. For melt processes, the highest endotherm is of importance to determine the melting point of the polymer. All polymers were found to have broad melting peaks, indicating a range of crystal sizes, and the T55D and T85A both have dual melting peaks. As a rule of thumb in melt blowing, setting the die to 30℃ above the highest melting temperature is a good starting point for polymers which there is no previous experience or knowledge of melt processing behavior. The orifices of melt blowing dies are very small compared to other melt processing dies and can become clogged very easily and thus causing necessary shutdown of the process. Being 30℃ above the highest melting point is typically high enough to avoid this while remaining in a reasonable temperature range to avoid polymer degradation.
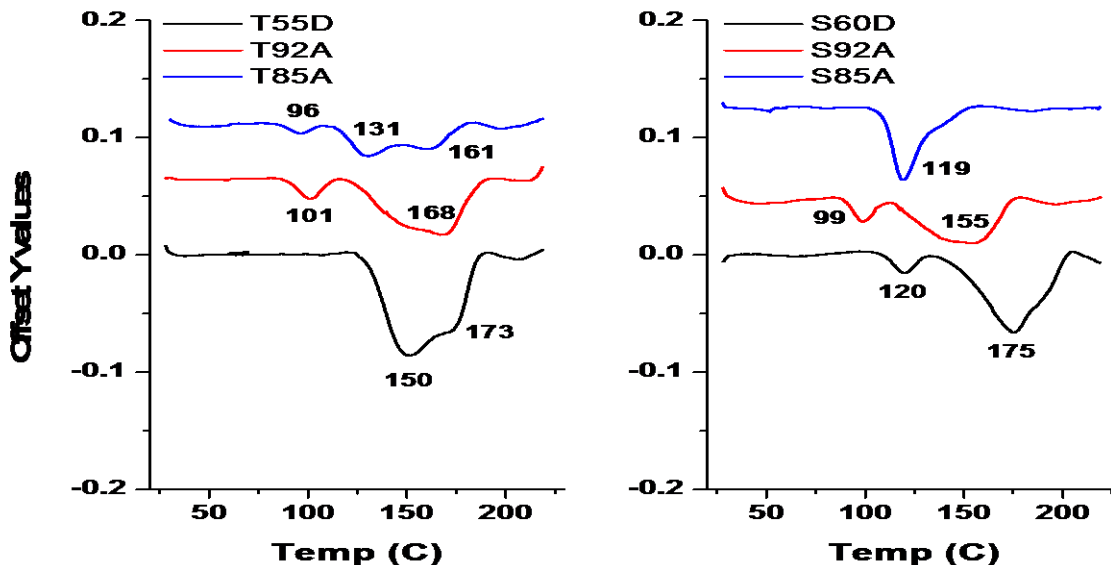
Figure 54. Ether and Ester based TPU resin melting curves.

Other than zone 1 of the extruder, other processing temperatures should be set to at least 10°C above the highest polymer melting temperature. The melt flow rate of the polymers can be used to give an idea of how to set these processing temperatures. Figure 55 shows the melt flow rate of the six screening polymers at temperatures of 210, 220, and 230°C. As expected, the MFR of all the polymers increases with increasing temperature. The graphs of the ether and ester soft segment based TPUs both show a change in slope at the 220°C temperature, indicating a shear thinning behavior. This rheological behavior is useful in melt processing, as it alleviates torque on the extruder screw and lowers processing pressure. From the graphs, it is seen that MFR increases with decreasing polymer shore hardness (decreasing hard segment content). However, the 85A polymers show lower melt flow rates than the 92A polymers at high temperatures. This is due to a greater contribution of the viscous effect of the higher soft segment content compared to the elastic effect of the hard segments to the melt flow rate or viscosity.

As previously stated, these characterizations give an indication of starting temperatures which will allow melt processing to begin without problems. Final melting temperatures

are adjusted once the process has stabilized and extruder torque and pressure and die pressure can be taken into account. The final processing temperatures of the screening polymers were presented in Table 3 and were set to maintain processing pressures between 300 and 500 psi. This was done to minimize differences on processing effects on the nonwoven web properties.
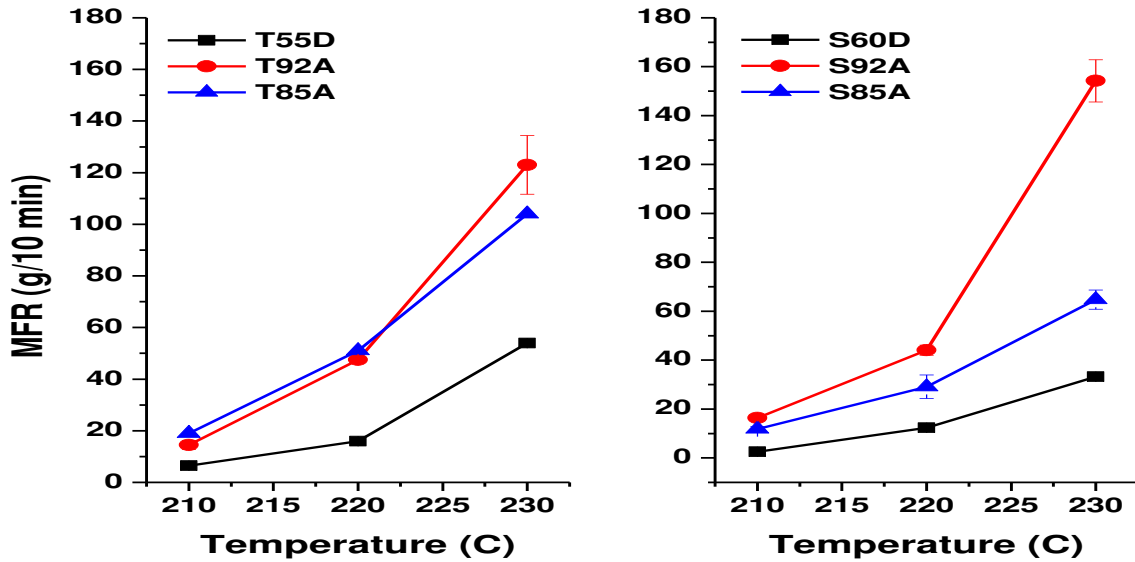
Figure 55. Ether and Ester based TPU resin melt flow rate as a function of temperature.

4.1.2: Nonwoven Web Characterization

TPU Processing Observations

Web quality varied greatly with different air pressures and DCD's. At an air pressure of 20 psi, the 85A polymers exhibited poor fiber formation at the 20 cm DCD but improved with increasing DCD. The S85A webs could not be collected due to considerable shrinkage down to approximately 2 − 3 inch width and wrinkling. The webs which were collected averaged approximately 6 inches. Figure 56 shows the cooling curves obtained

with the DSC scans of the polymers. Though webs quench at a much faster rate during melt blowing than the 10 degree per minute rate used in the DSC, the curves remain useful in analyzing the crystallization kinetics of polymers during melt blowing. All polymers show crystallization on cooling except the S85A indicating there would likely be problems during collection of nonwoven webs of this polymer.

The extruder overheated periodically during processing of the shore hardness D polymers. To compensate, the first heating zone of the extruder was increased to much higher temperatures above the polymer melting temperatures. This did alleviate the overheating issues however the hopper feed throat would clog over time if not agitated due to premature melting of the pellets. High air temperatures were also required to form quality webs of the shore hardness D polymers. This may be significant in industry as air heating is the most expensive component of the process. No issues were experienced with processing the 92A shore hardness TPUs.
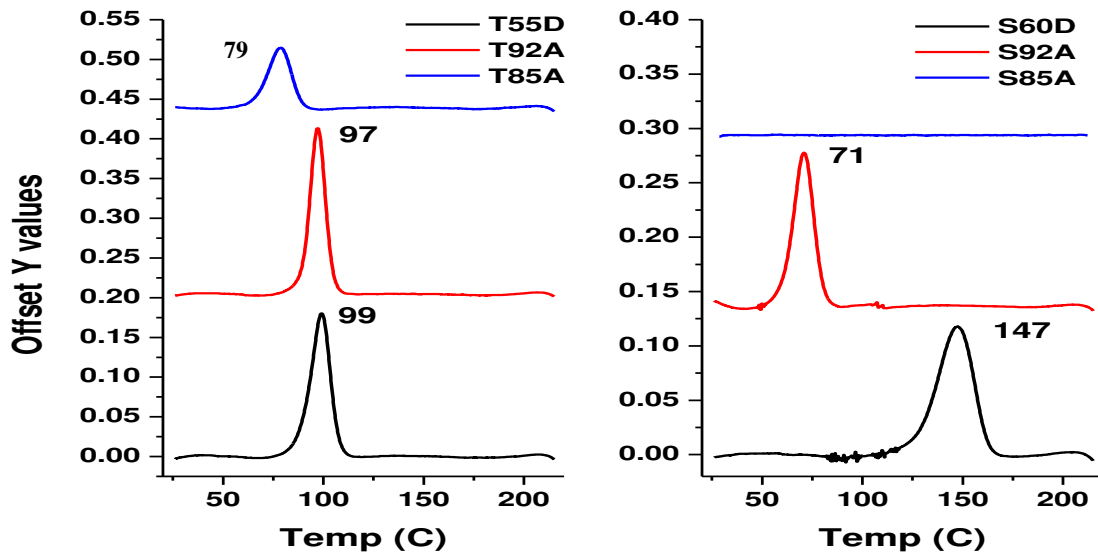
Figure 56. Ether and Ester based TPU resin cooling curves.

Intrinsic Viscosity

Polymer and web intrinsic viscosity (IV) is presented in Figure 57 and the values are tabulated in Table 10. A loss of intrinsic viscosity is expected during melt extrusion processing due to chain scission. Also, thermoplastic polyurethanes are known to undergo urethane dissociation at temperatures above 130°C leading to additional loss in molecular weight. The shore hardness D webs lost more than 50% of the polymer intrinsic viscosity due to the very high temperatures necessary to prevent extruder overheating. The S92A web also lost a considerable amount of IV at 48%. The T92A and T85A webs both lost less than 40% IV. Melt blowing typically sees IV losses in polypropylene and polyesters around 30%. The higher losses here are attributed to the urethane bond dissociation. The intrinsic viscosity losses here were much lower than those published by Zapletalova [77] which lst between 75 to 80%. Those TPUs were processed at temperatures greater than 260°C while the highest processing temperature here was 245°C.
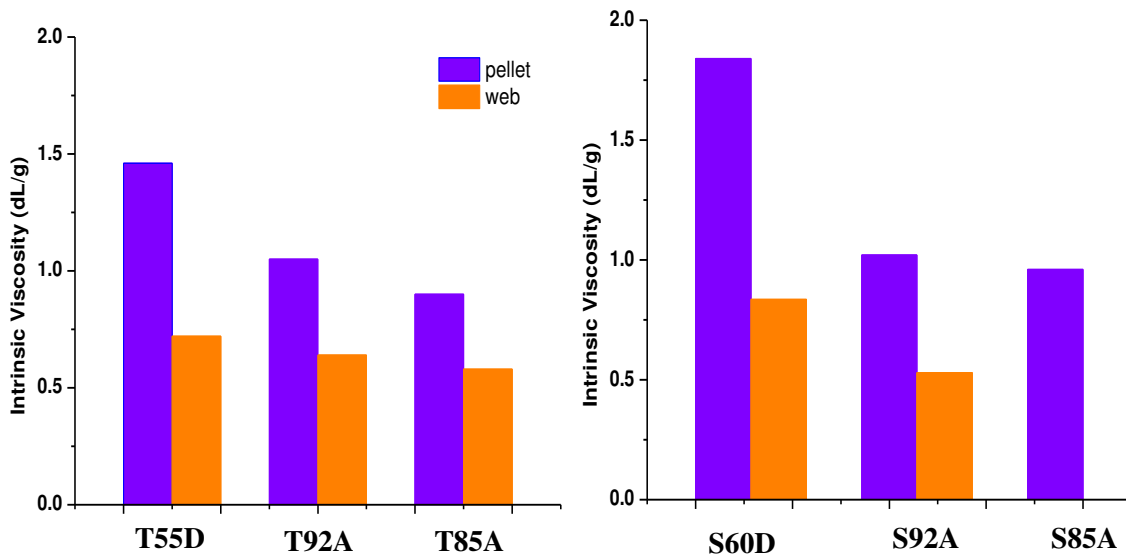
Figure 57. Ether and Ester based TPU resin and web intrinsic viscosity.

Table 10. TPU pellet and web intrinsic viscosity.

| Polymer | Intrinsic Viscosity (dL/g) | | %Δ [η] |
	Pellet	Web	
T55D	1.46	0.72	50.7
T92A	1.05	0.64	39.0
T85A	0.9	0.58	35.6
S60D	1.84	0.835	54.6
S92A	1.02	0.53	48.0
S85A	0.96	-	-

SEM Imaging

Scanning electron microscope image of webs processed with 25 psi air pressure at 20,30, and 50 cm DCD are shown in Figures 58 (ether based) and 59 (ester based). Fibers show increasing entanglement and roping with increasing DCD with the degree of entanglement increasing as TPU MFR increases in respect to the corresponding shore hardness of the polymer. The 92A shore hardness polymers had the highest MFR and consequently a higher degree of roping in the webs as the fibers are less stable in the air field.
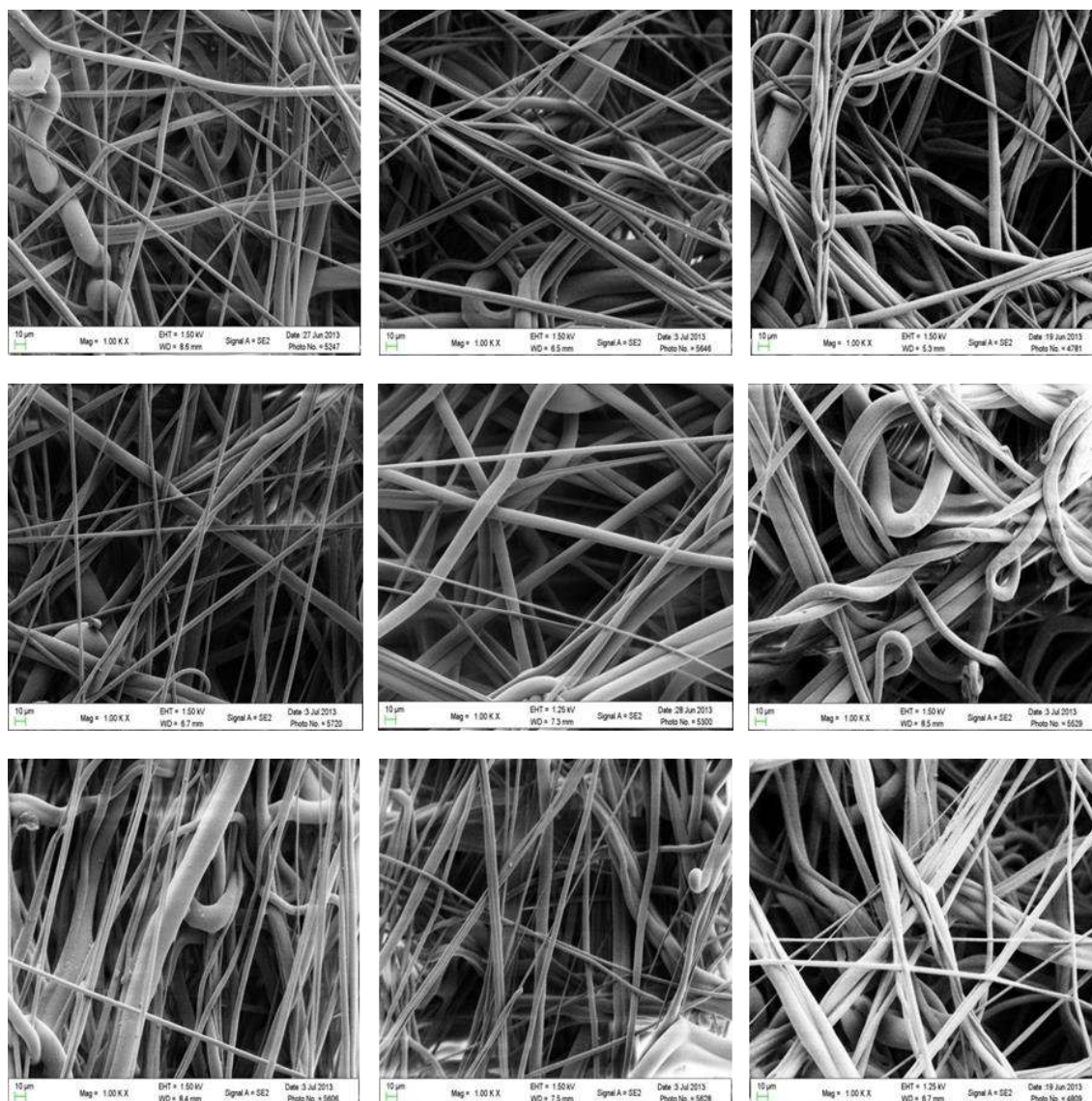
Figure 58. . SEM images of ether based webs. Top down: T55D, T92A, T85A. Left to right: 20/25, 30/25, 50/25 (DCD/Air pressure)
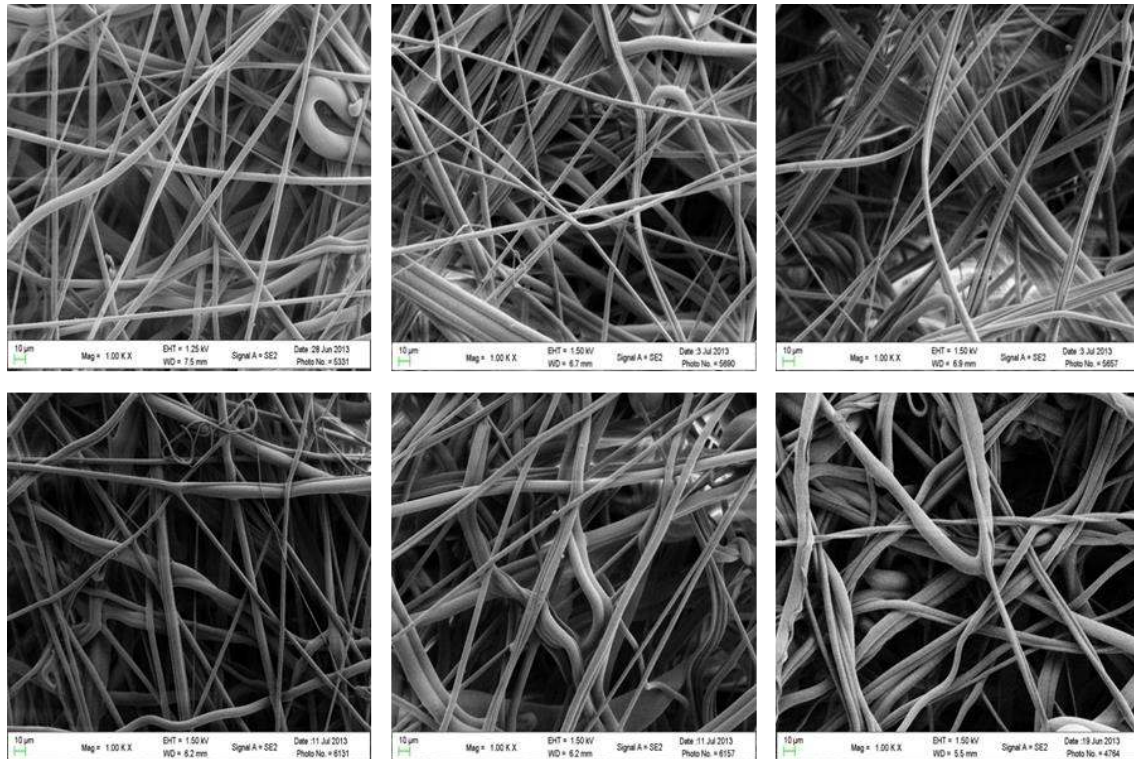
Figure 59. SEM images of ester based webs. Top down: S60D, S92A. Left to right: 20/25, 30/25, 50/25 (DCD/Air pressure)

Average Fiber Diameters and Distributions

The average fiber diameters for all of the webs produced (20 and 25 psi at 20, 30, and 50 cm DCD) are shown in Figure 60. Overall, average fiber diameters of the webs produced ranged from 4.69 to 7.66 microns, a difference of 2.97 microns. No fiber diameters larger than 14 um were measured. Breese [58] and Lee [59, 76] showed that fiber attenuation to smaller diameters occurs at distances less than 10 cm. away from the die face where temperatures are great enough to overcome the molten fiber viscosity. Therefore, changes in average fiber diameter with DCD is not expected in these webs as they were collected at a 20 cm. DCD and greater. The variations seen in average fiber diameter with increasing DCD seen here arise from the selection of fibers for

measurement.   The 25 psi are pressure produce webs with smaller average fiber diameter which is consistent with melt blowing theory concerning effect of air flow rate on fiber diameter. The variation from theory for the T92A web at all DCDs and S60D at 30 cm DCD is likely due to the fibers chosen for measurement. The error bar overlap at each DCD/air pressure combination indicates a broad distribution of fiber diameters. This is further verified in the fiber distribution plots in Figures 61 (ether) and 62 (ester). In these graphs, the peaks of the normal curve overlays represent the average fiber diameter. The distribution of fiber diameter becomes larger with decreasing polymer hardness for both ether and ester based webs while Figure 60 shows little difference in average fiber diameter between the different shore harnesses investigated.
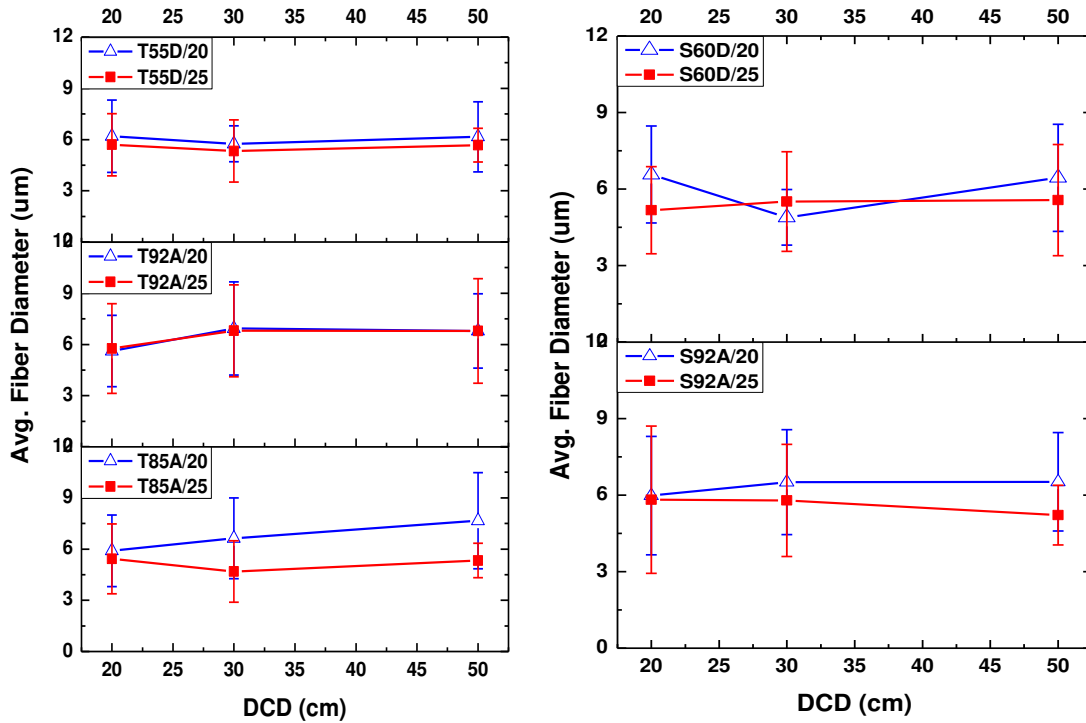
Figure 60. Avg. fiber diameter of TPU 80 gsm webs.
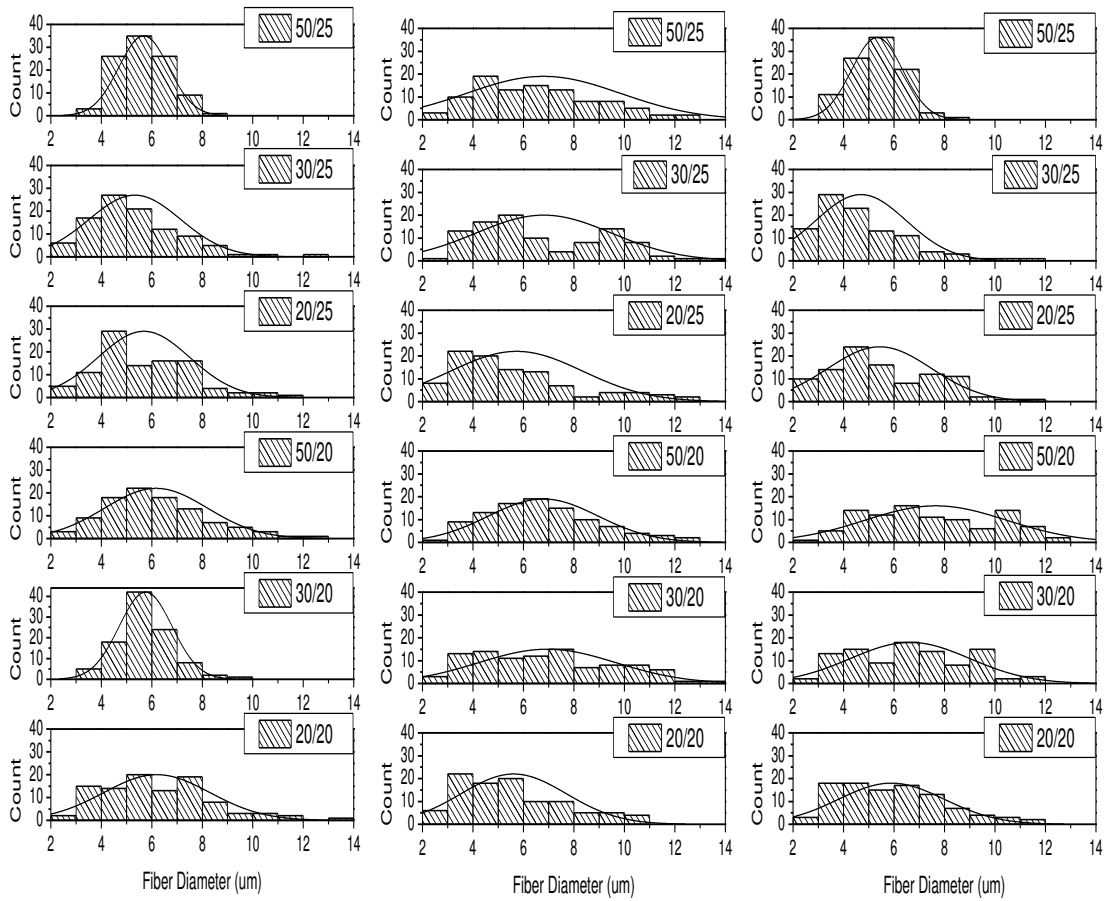
Figure 61. Ether based web fiber diameter distributions. The curve peak represents the average.
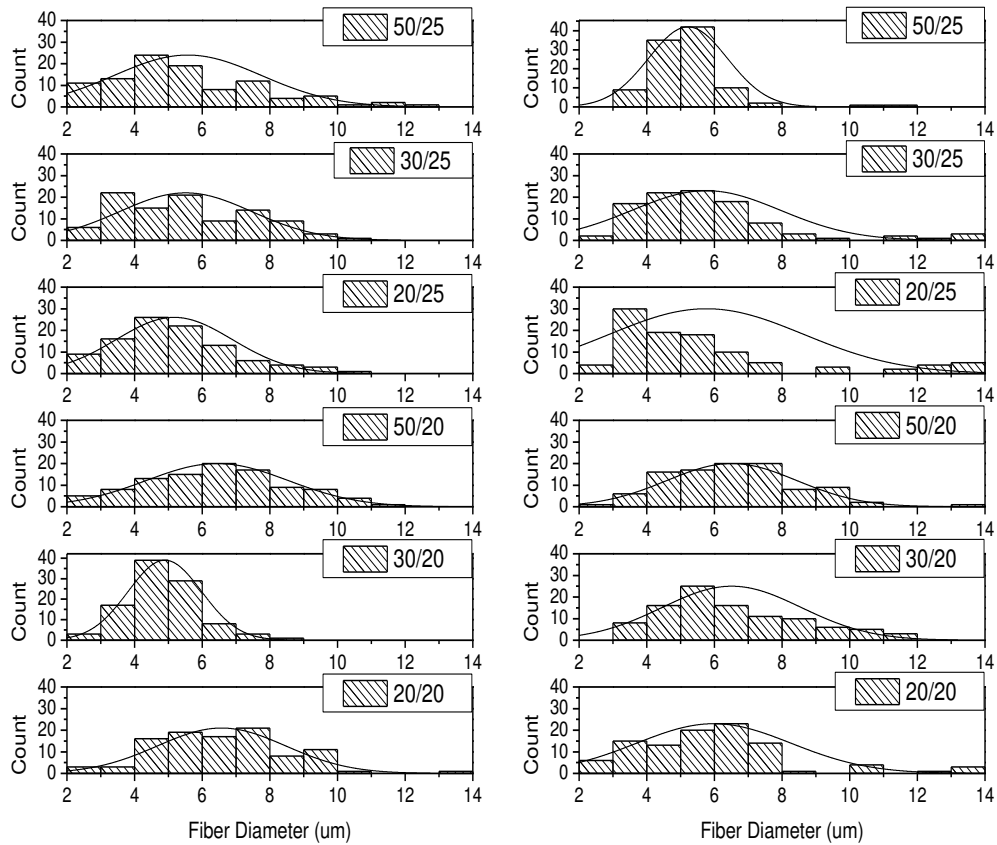
Figure 62. Ester based web fiber diameter distributions. The curve peak represents the average.

Break Force and Elongation

Break force and elongation at break as a function of DCD and air pressure behavior for samples cut in the machine (MD) are shown in Figures 63. Both break force and elongation at break were found to decrease with increasing DCD. This type of behavior is unusual in polymers which generally display increasing elongation with decreasing strength. To understand the behavior observed, it is necessary to understand how nonwoven strength develops during the melt blowing process.
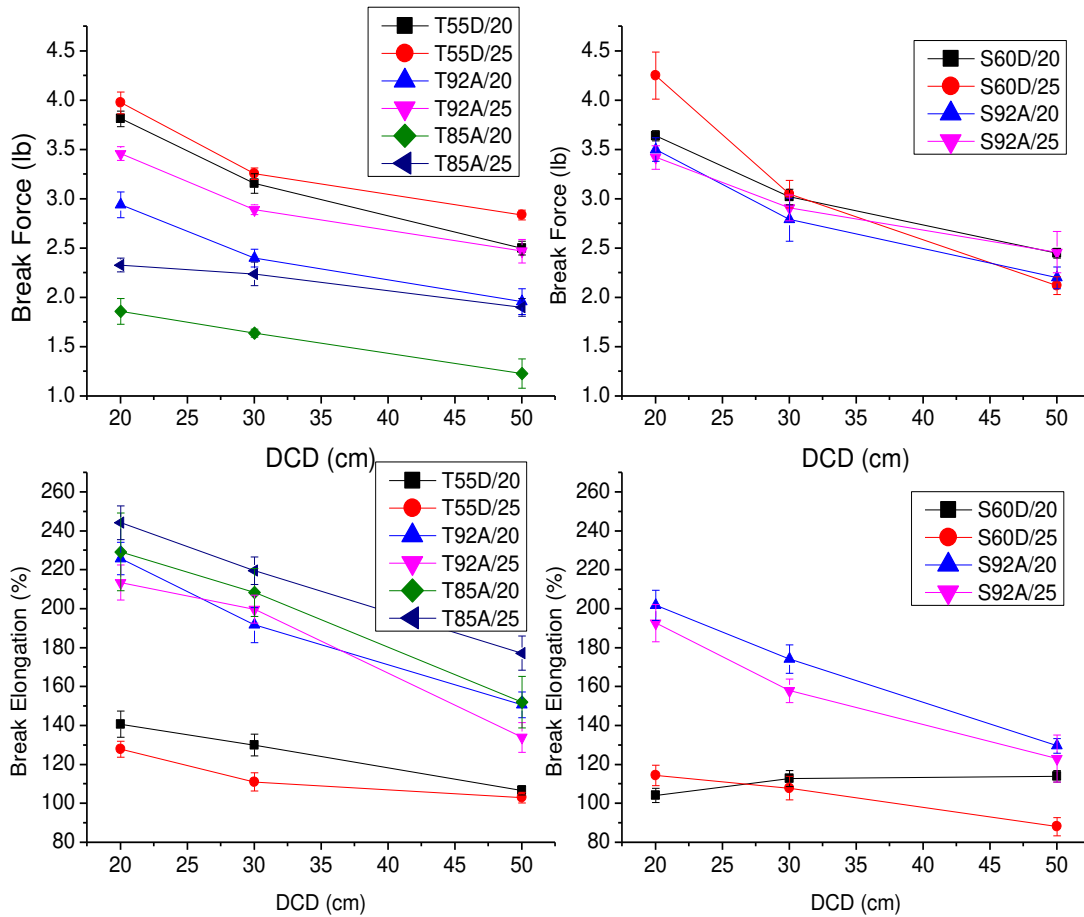
Figure 63. Web strength and elongation % at break in the machine direction.

The air temperature and velocity profiles of commercial style melt blown lines were investigated by Bresee, Begenir, and Lee [74,75,79]. They found that both parameters decrease rapidly away from the die and plateau out around 15 -20 cm. They all found fiber attenuation ceases when the air and fiber velocities are equal and the drag force on the fiber drops to zero. For the different melt blowing lines investigated, this point in which the air and fiber velocities equal was found to be less than 10 cm. At distances greater than 10 cm from the die, the fibers can be considered to be at nearly isothermal conditions. Lee [74] reported that their 240 °C air temperature dropped to 71°C at 6 cm

96

from the die followed by a decrease to 51°C at 20 cm. They reported their air velocity as 60% of an open air valve and measured air speeds at multiple air distances with a pilot tube.

With the fibers being attenuated at high air temperatures near the melt temperature and high air velocities, little to no molecular orientation is obtained in the fiber. Therefore chain orientation has little effect on the strength of the web. This has been verified by Bresse and Begenir for PP and TPU, respectively. Also, crystallinity of the web depends only on the polymer type and time the fiber spends in its crystallization temperature range. This was verified in this investigation as no crystallinity change was found with DSC scans for the same polymer species processed at the DCD's and air pressures investigated. This has also been observed in this melt blowing facility with PP, PET, Nylons, and PBT for different DCD's and air pressures. Some small changes in crystallinity can be found when air pressures are drastically different however the upper range of air pressure necessary to invoke crystallinity changes is not economical from a cost standpoint as well as the resulting web is generally of non-uniform character. To change the web crystallinity, the die temperature should be altered with higher temperatures providing higher crystallinity.

Taking these aspects into account, web strength is thought to be dependent on the inherent polymer properties, the fiber orientation in the web, and inter-fiber bonding within the web [79]. The inherent polymer properties explain the trend of decreasing strength and increasing elongation found with decreasing polymer hardness. Begenir [79] found no effects of DCD changes at constant air velocity for fiber orientation in TPU webs and Lee [74] found similar results for PP webs. Close observation of the SEM images from this study indicate very little change in fiber orientation at different DCD's for a constant air pressure. No difference in fiber orientation was readily observed for increasing air pressure as well. Observations did reveal however, greater fiber bundling and roping with increasing DCD. This leaves inter-fiber bonding as the final component. When the molten fiber exits the die, it begins attenuation and cooling immediately. When the crystallization temperature is reached, the fiber begins to solidify with

97

complete crystallization and solidification typically occurring on the collection belt but before winding. The time it takes for the fiber to reach the collection belt and contact other fibers dictates the amount of inter-fiber adhesion within the web. At short DCD's, the fiber is still hot and tacky when it hits the fibers already on the collection belt. This allows for numerous inter-fiber adhesion sites in the web and therefore a stronger web. As the DCD is increased, the fibers have more time to cool resulting in a web with less inter-fiber adhesion and a weaker web. The effect of air pressure is that with increasing air pressure, the fiber travels at a faster rate to the collector and consequently is at a hotter temperature resulting in a stronger web. The small decrease in fiber diameter with the higher air pressure (25 > 20 psi) is assumed to not have much effect on the cooling rate of the fiber as crystallization kinetics observed in DSC scans did not reveal any changes. This is clearly seen in Figure 63 for the samples tested in the machine directions for 25 vs. 20 psi air pressures.

Figure 63 clearly demonstrates the dependence on DCD and air pressure for web strength in the ether based webs. Strength decreases with decreasing polymer hardness while elongation decreases with increasing polymer hardness. The degree of decrease from 20 to 30 cm is seen to decrease with decreasing polymer hardness as well. From 30 to 50 cm the loss of strength and elongation remains similar between the different TPUs. The ester results show a lower degree of strength dependence on polymer hardness at higher DCD's. The T55D and S60D webs showed considerable less elongation properties compared to the softer webs. Overall, the ester based webs possessed greater strength at break while the ether based webs possessed greater elongation. This coincides with conventional knowledge of ester and ether based TPU tensile properties with polymers of similar molecular weights and shore hardness.

Pore Size

The average pore size was found to increase with increasing DCD and decrease with higher processing air pressure. (Fig. 64) Increasing DCD causes an increase in pore size because fiber entanglement increases at larger DCD's resulting in reduced fiber cover in the web. At higher DCD's, the webs are cooler and therefore less fiber-to-fiber bonding occurs in the web. When air flow is increased, finer fibers are produced, creating a greater pore cover in the web. The fibers also travel faster and are at a higher temperature when they land on the collection belt allowing for more fiber-to-fiber bonding sites.

Most webs showed a large increase in pore size from 20 to 30 cm DCD and from 30 to 50 cm, the increase was to a lesser degree. The T55D web average pore size stayed relatively the same with the increase for 30 to 50 cm DCD. The T85A web processed at 20 psi showed the largest average pore size at 20 cm due to the poor fiber formation in the web. At 25 psi, the T85A web showed a decrease in average poor size from 20 to 30 cm DCD. This is also seen in its air permeability results presented in Figure 65. This is easily explained just by visual observation of the webs. At low DCD, the T85A polymer does not produce a high quality web as the fibers are not quenched and shrink resulting in a web with poor coverage. As the DCD is increased, the fibers have enough time to quench and form a higher quality web. It should also be noted that the standard deviation of the pore size increases with increasing DCD. This tells us that the range of poor sizes in the web increases at higher DCD's.
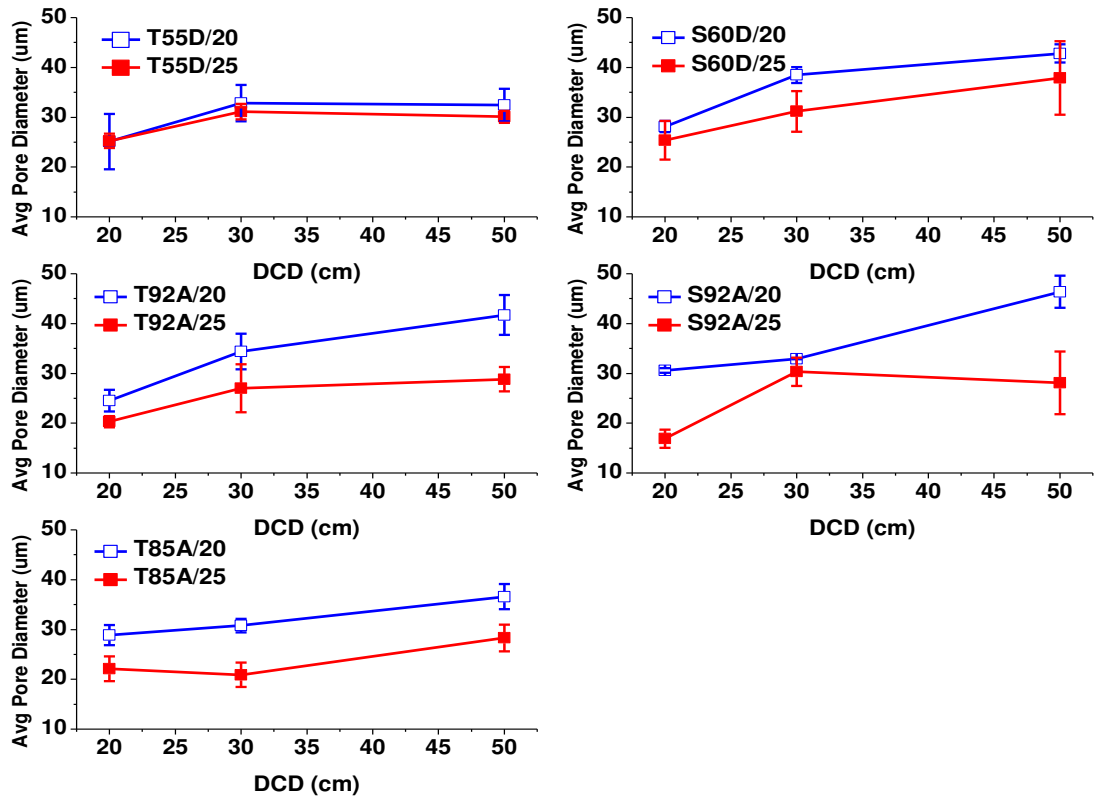
Figure 64. Average pore diameter as function of DCD and air pressure.

Air Permeability

The air permeability results are shown in Figure 65. As expected after analysis of the average pore size, air permeability also increases with increasing DCD. Air permeability was also found to decrease with increasing air pressure. The T85A/20 web showed the highest air permeability due to the poor web formation. The T85A/25 data showed a similar shape as its pore size data.
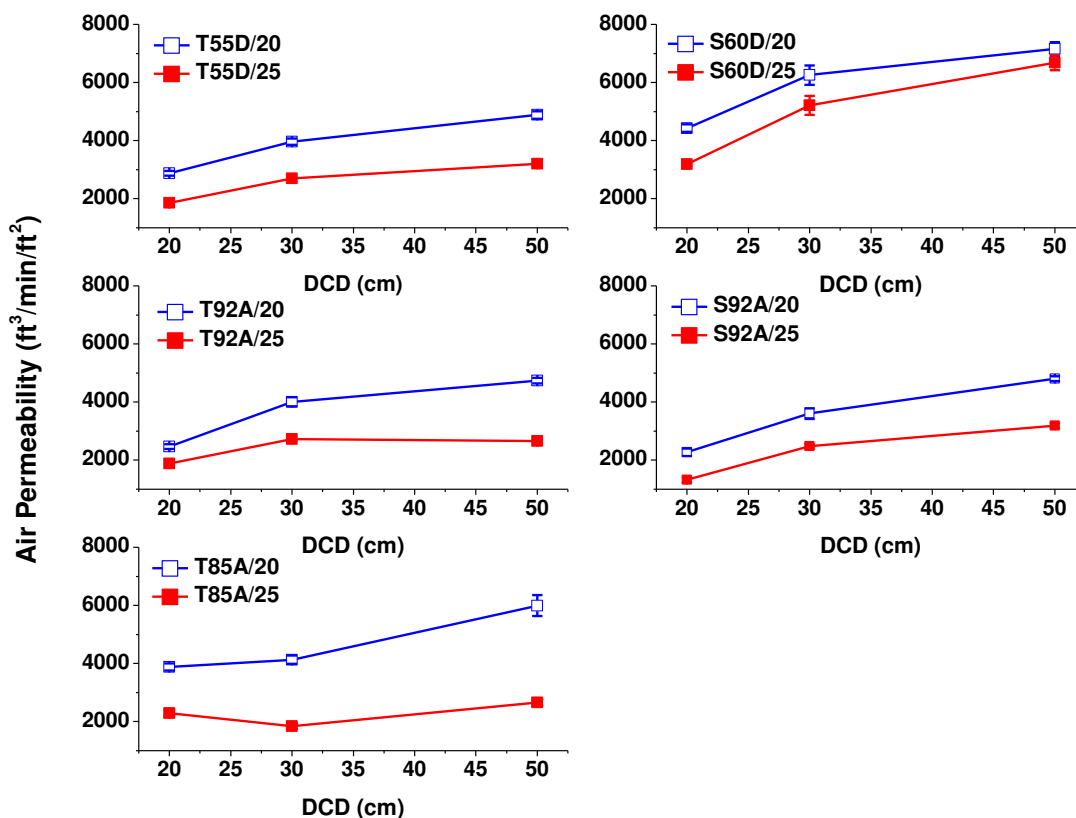
Figure 65. Ether and Ester web air permeability as function of DCD and air pressure.

Dynamic Mechanical Analysis

DMA double log frequency scans for E' and E" at room temperature of single webs are shown in Figure 66. Both moduli, E' and E", increase with increasing shore hardness. This is due to the ratio of hard versus soft segment content. The ester based webs show higher moduli than their respective ether based webs at similar or equal hardness due to a higher degree of hydrogen bonding and phase mixing. Both E' and E" increase over the frequency range investigated which is promising for dampening properties at higher strain rates.
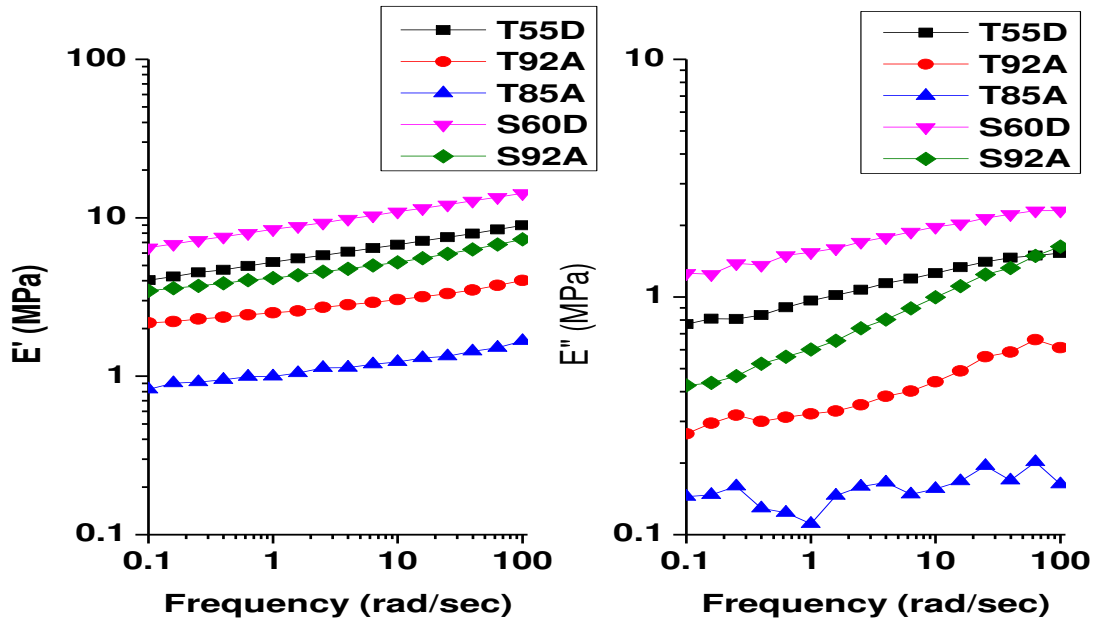
Figure 66. E' and E" of DMA frequency scans at room temperature of 80 gsm 1 layer webs.

Temperature scans at 10 and 100 Hz of 4 layer sandwich composites are shown in Figures 67 - 69 respectively. The webs were hot pressed at 90°C for 90 seconds with 11 tons of pressure. The effect of shore hardness is clear in the storage modulus (E') graph, as E' increases with shore hardness. (Figure 67) This is expected since higher hard segment content increases strength and also acts as a reinforcing filler dispersed in the soft matrix. The storage modulus drops about two orders of magnitude over the temperatures range investigated. The glass plateau is extended and the temperature at which E' begins to drop from the glass plateau increases with increasing shore hardness. This is due to a more perfect hard domain structure attained with higher hard segment content. The onset of the plateau in the rubber region occurs at higher temperatures with increasing shore hardness is also due to the degree of order in the hard segment domain of the higher shore hardness polymers. The storage modulus increases to higher values from the 10 Hz scan to the 100 Hz scan, indicating increasing viscoelastic properties at shorter time scale deformations.

102
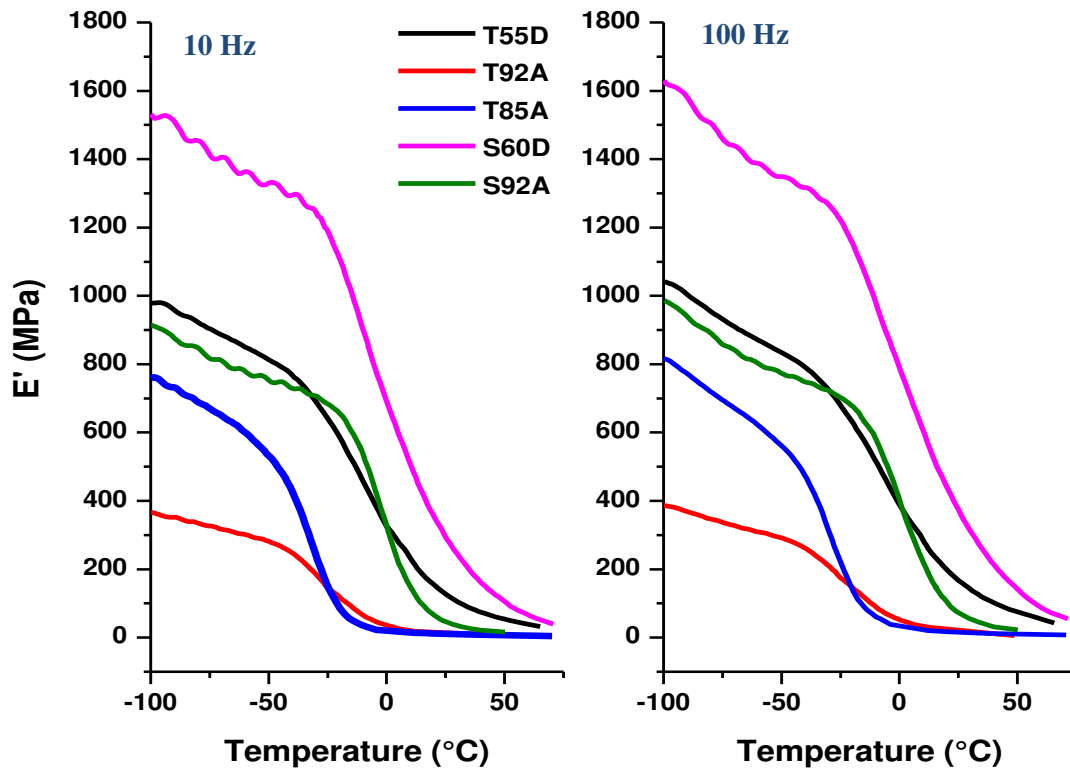
Figure 67. Storage Modulus (E') of 4 layer composites of 80 gsm webs.

The loss modulus curves at 10 and 100 Hz are shown in Figure 68. Damping discussion pertaining to these materials is interpreted with the tan delta curves shown in Figure 69. The peaks of the E" curves were utilized for calculation of the activation energy which are presented in Figure 70. In regards to the E" curves, the magnitude at low temperatures in the 100 Hz scan is much greater than the 10 Hz scan and the peaks are also shifted to higher frequency.
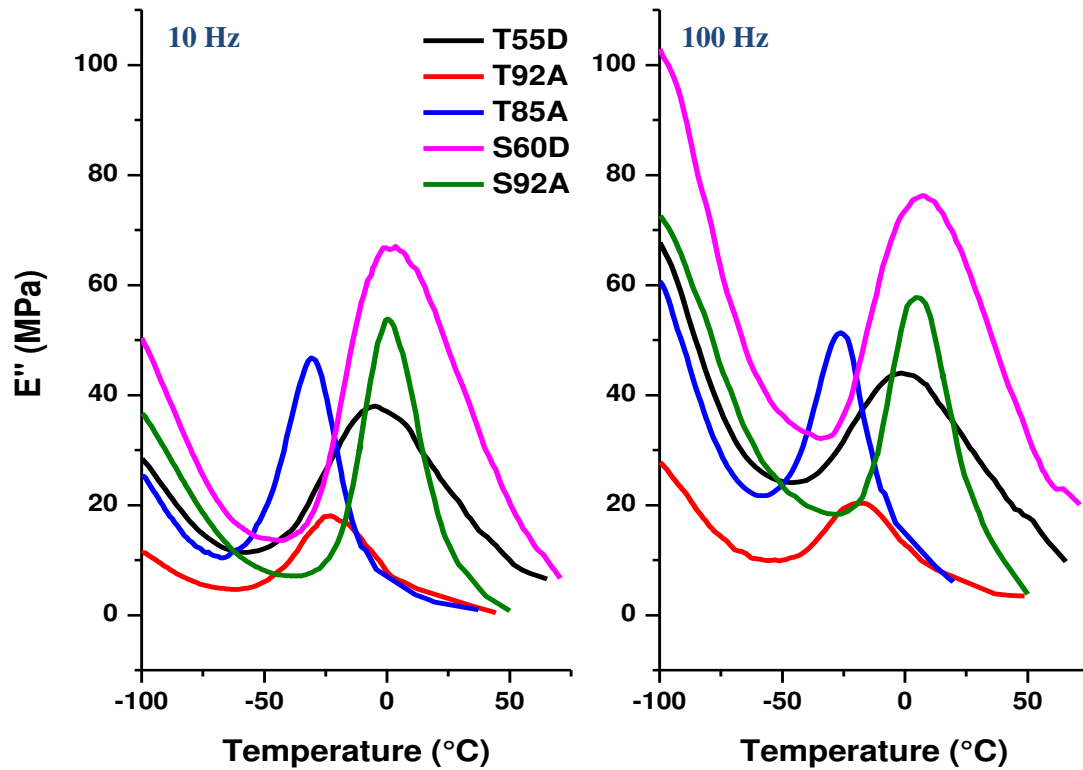
Figure 68. Loss Modulus (E") of 4 layer composites of 80 gsm webs.

Figure 69 shows tan delta curves for 10 and 100 Hz temperature scans. Glass transitions (Tg) are labeled for each curve. The glass transition results from soft segment relaxation and is sensitive to the material composition. In these TPUs, the glass transition was found to increase with increasing shore hardness (increasing hard segment content). The tan delta peaks also broaden and decrease in magnitude with increasing hard segment content. With increasing hard segment content, larger and more ordered hard microcrystalline domains are formed resulting in restricted the molecular motion of the soft segments.

From a soft segment point of view, an increase in soft segment length or molecular weight increases the TPUs degree of phase separation by the increase in incompatability

[30]. This leads to a decrease in Tg and tan delta peak intensity increase while the peaks become narrow. In Figure 69, the Tg decreases with decreasing shore hardness (higher soft segment content and higher molecular weight) as less energy is required for the material to undergo the phase transition from glass to rubber upon heating. This is verified in the activation energy calculations which are discussed later.

The Tg of the polyether based TPUs were found to be lower than that of the polyester based TPUs. This is due to the availability of C=O groups of each monomer in a polyester for possible hydrogen bonding with the N-H groups in the urethane hard segments. The higher degree of hydrogen bonding of polyester based TPUs lowers the free energy of mixing of the hard and soft segments that drives phase separation [29, 30]. The more flexible ether bond and higher free energy of mixing of polyether based TPUs allow them to attain a higher degree of phase separation and thus the soft segments have greater mobility and require less energy to relax.
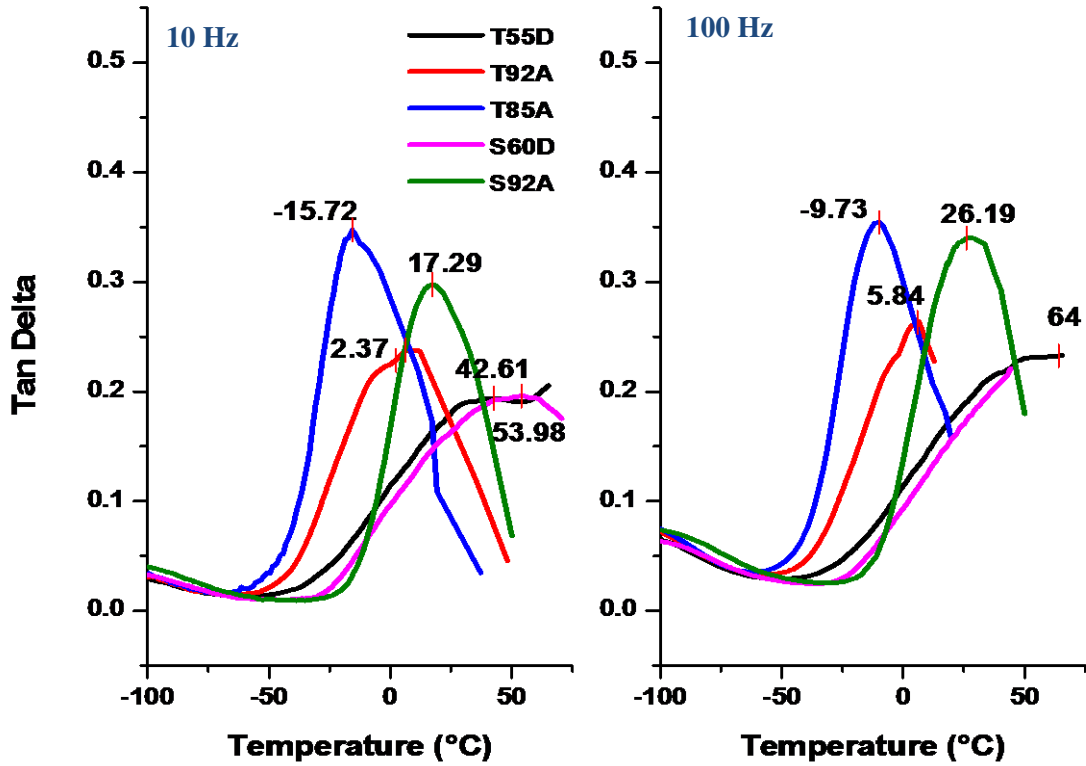
Figure 69. Tan delta of 4 layer composites of 80 gsm webs.

The activation energy of the TPU web glass transitions are shown in Figure 70. The calculations were taken from the E" peaks of the dynamic mechanical analysis temperature scan of each 4 layer sandwich (Figure 68) using the Arrhenius equation.

$$f = A \exp \frac{-E_a}{RT_g} \qquad\qquad (23)$$

The 1 Hz curves are not shown in the graph due to considerable noise which is likely due to stress in the sample relaxing over the length of the sample at longer test times for the

low frequency. The ether samples show a trend of decreasing activation energy required to undergo the glass transition. The ester based webs do not show the expected trend as both have approximately the same activation energy. This is likely due to the high processing temperatures required for S60D which resulted in a large decrease in intrinsic viscosity of the S60D web which can be related to a high degree of molecular weight loss (shorter chain length are more mobile).
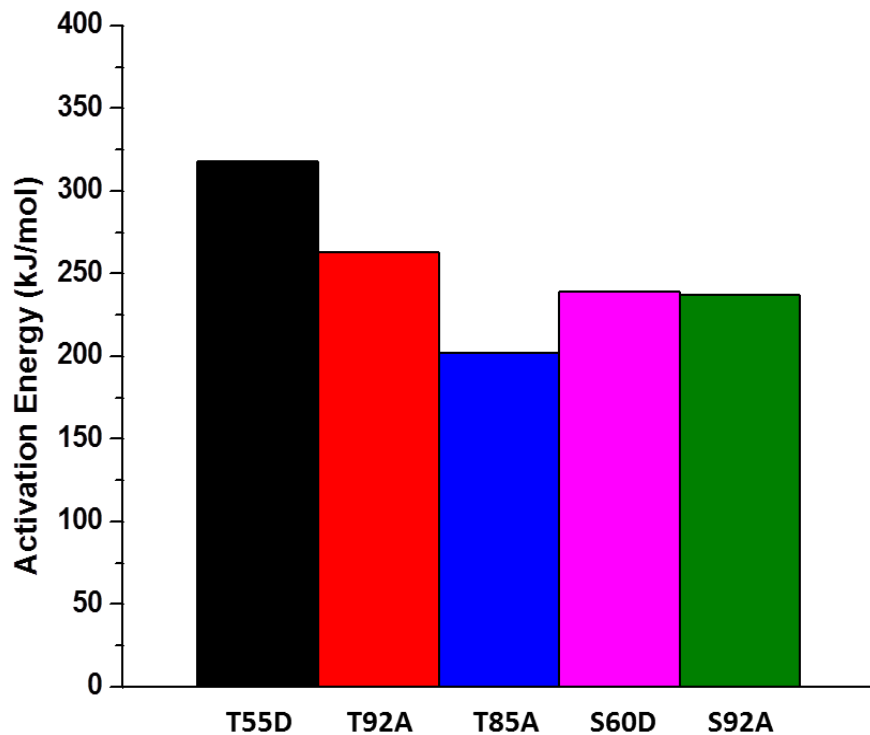
Figure 70. Ether and Ester based TPU web activation energy.

Glass transition temperatures as a function of frequency are shown in Figure 71. The solid lines represent the best fit for the glass transition temperatures determined from the 1, 10, and 100 Hz tan delta peaks. To predict possible glass transition temperatures for the 4 layer sandwich composites at frequencies associated with high velocity impacts, the

best fit solid lines were extended as dashed lines into the high frequency range. As stated previously, the Tg should be close to the expected use temperature in order to exploit the energy consumption of the rubber to glass phase transition at impact. The possible use temperature is dependent on the season and geographical region in which the material is used. To cover a broad temperature range, 20° to 35°C (68° - 95°F) is blocked off in a frequency range of 500 to 10,000 Hz (Figure 71). As stated previously, strain rates ranging from 10^4 to 10^6 are typically experienced with high velocity ballistic impacts. The sacrificial armor (vest or helmet) will absorb much of that energy and the remaining strain of frequency of the propagating strain wave could range from 500 to 10^4 Hz. There is no supporting literature for this theory but it is reasonable to expect reductions in the strain induced by high velocity impact as some energy will be absorbed and dissipated by the sacrificial armor before it is passed to the underlying sandwich composite. The T92A sandwich composite is the only material in which the predicted Tg encompasses the region boxed off in the graph but only a small portion in the low frequency range.
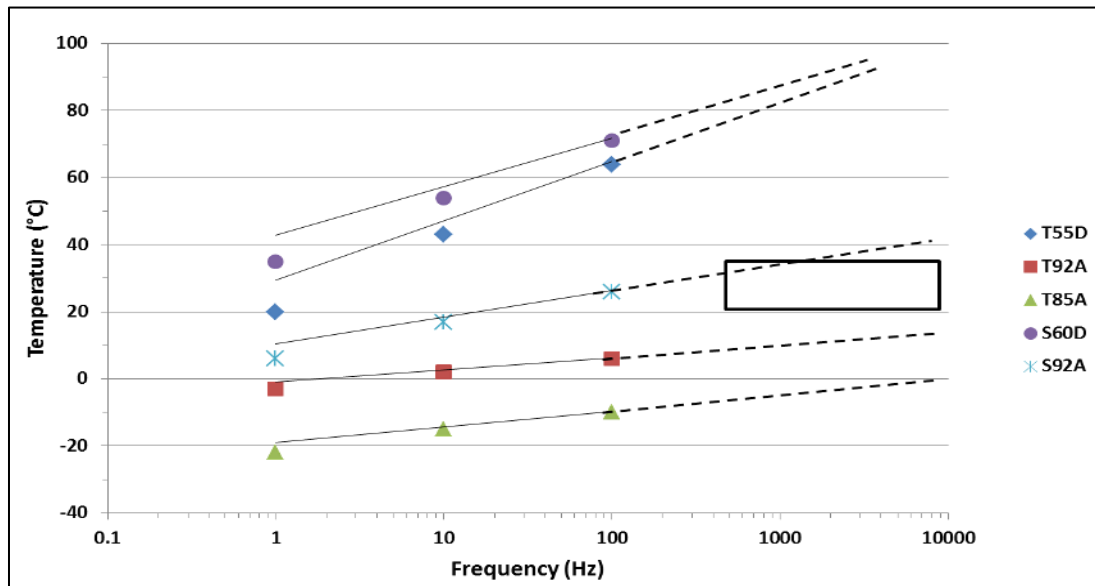
Figure 71. Tg prediction at high frequencies.

4.1.3: TPU Nonwoven Web Screening Conclusions

The shore hardness D polymers were hard on the melt blowing equipment and required processing temperatures much higher than their melting temperatures to reduce the torque on the processing screw and prevent extruder overheating. Also the glass transition temperatures at 100 Hz (64° and ~ 55°C) were higher than the expected use temperature (20 - 35°C) for the application and the transition from rubber to glass upon impact would not be exploited.

The T85A polymer was somewhat difficult to process and due viscous nature of the higher soft segment content and low quenching (crystallization) temperature. The webs collected were very soft and flexible. It is likely that the lack of stiffness would cause difficulties in the coating experiments. The Tg was also too low for the intended application. The 92A shore hardness webs had good processability and the predicted Tg of the S92A in the high frequency range encompasses a small portion of the boxed area in Figure 71. The T92A material showed poor damping in the Tan delta graphs and the Tg is not in a suitable range.

Taking these conclusions into account, it was decided to use an ether based TPU of 90A shore hardness. The chosen polymer and its properties are discussed in the following section.

4.2: TPU Web for Nanofiller Reinforcing

Estane 58215 ether based 90A shore hardness TPU was used for reinforcement with nanoparticles. The web was collected at a DCD of 40 cm with 30 psi air pressure. No issues were experienced during melt blowing. Intrinsic viscosity was found to decrease from 1.35 to 0.8 dL/g, a loss of 40%. This is comparable to the previous intrinsic viscosity results for the screening TPUs.

The web properties and characteristics are listed in Table 11. The webs were collected at 100 gsm basis weight. The average fiber diameter was 4.2 um. This was actually slightly lower than the 80 gsm webs averaged (4.7 – 7.7 um) despite a higher throughput (0.83 > 0.67 ghm). The smaller fiber diameter is attributed to the higher air pressure (35 psi) utilized for this web. This high strength and elongation at break suggest a web with high toughness suitable for energy absorption and dissipation.

Table 11. T90A web properties.

Method	Sample Avg. (std. dev)
Basis Weight (gsm)	100
Fiber Diameter (µm)	4.2 (1.4)
Thickness (mm)	0.47
Air Permeability ($ft^3/min/ft^2$)	1100
Modulus (psi) Machine/Transverse	58/13.2
Break Stress (psi)	790
Break Elongation (%)	330

Figure 72 shows a DMA temperatue scan of the T90A 4 layer snadwich composite. Peak temperatures for E" and tan delta are labeled and show shifts to higher tempertures with the increase in frequency for 10 to 100 Hz. The E' at low temperature doesn't show improvemet with increasing frequency however, E" does therefore tan delta in also increased. At higher temperatures, E" shows a larger improvement with increased

frequency and therefore the tan delta at 100 Hz has an increased magnitude over the 10 Hz peak.
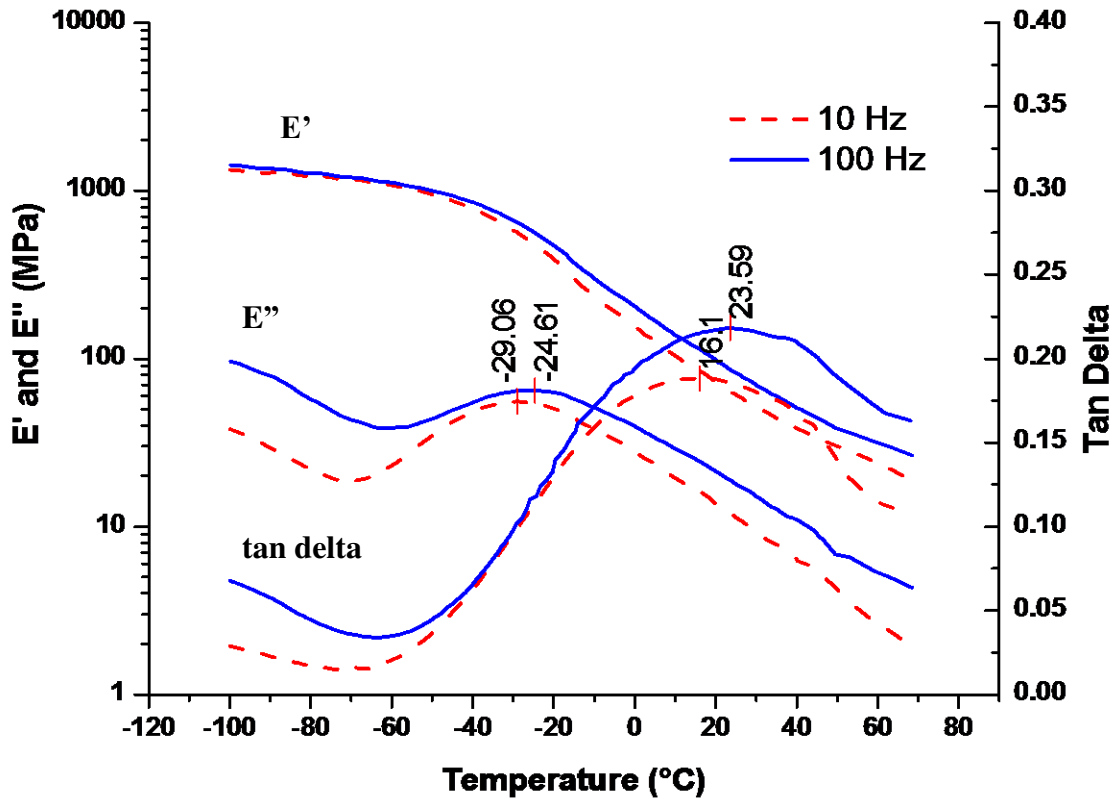
Figure 72. T90A 4 layer sandwich DMA temperature scan.

Figure 73 shows the glass transition temperatures taken from the tan delta peaks at 1, 10 and 100 Hz as a function of frequency. The solid line represents the best fit of the three data points. The dashed line which represents the possible Tg at higher frequencies passes through a good portion of the boxed area for representative use temperatures and possible frequencies of strain the material may be under after impact. This predicts the T90A material will undergo the phase transition from rubber to glass at impact.
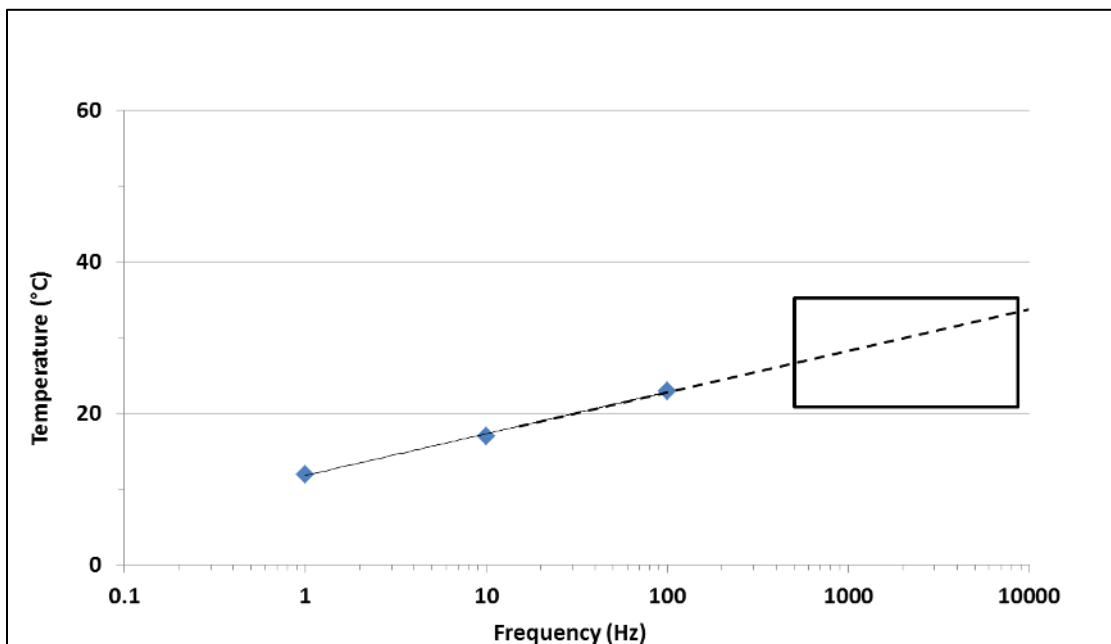
Figure 73. Prediction of Tg for T90A at high frequencies.

DSC scans of the unprocessed polymer and web are shown in Figure 74. A low temperature and high temperature endotherm is observed in both scans with both endotherms showing and increase in peak temperature in the web over the polymer. The 1st endotherm increases from 83°C in the polymer to 102°C in the web. This endotherm could originate from a number of thermal transitions and will be further discussed in the following section. The web T_m is increased to 185°C from 159°C of the polymer. This is due to polymer chain orientation in the fiber and higher degree of crystallinity in the web as ΔH increased from 25 J/g for the polymer to 27 J/g in the web.

The cooling curve in Figure 74 shows the web has faster crystallization kinetics. The web crystallizes at a much higher temperature of 154°C while the polymer crystallizes at 98°C. The enthalpy (ΔH) also increased from 8.7 J/g in the polymer to 13.7 J/g in the

web. These increases are likely due to chain scission during processing with the shorter chains acting as nucleating agents and allowing greater mobility due to a shorter length which enabling them to diffuse in the melt and aggregate to form crystalline hard domains.
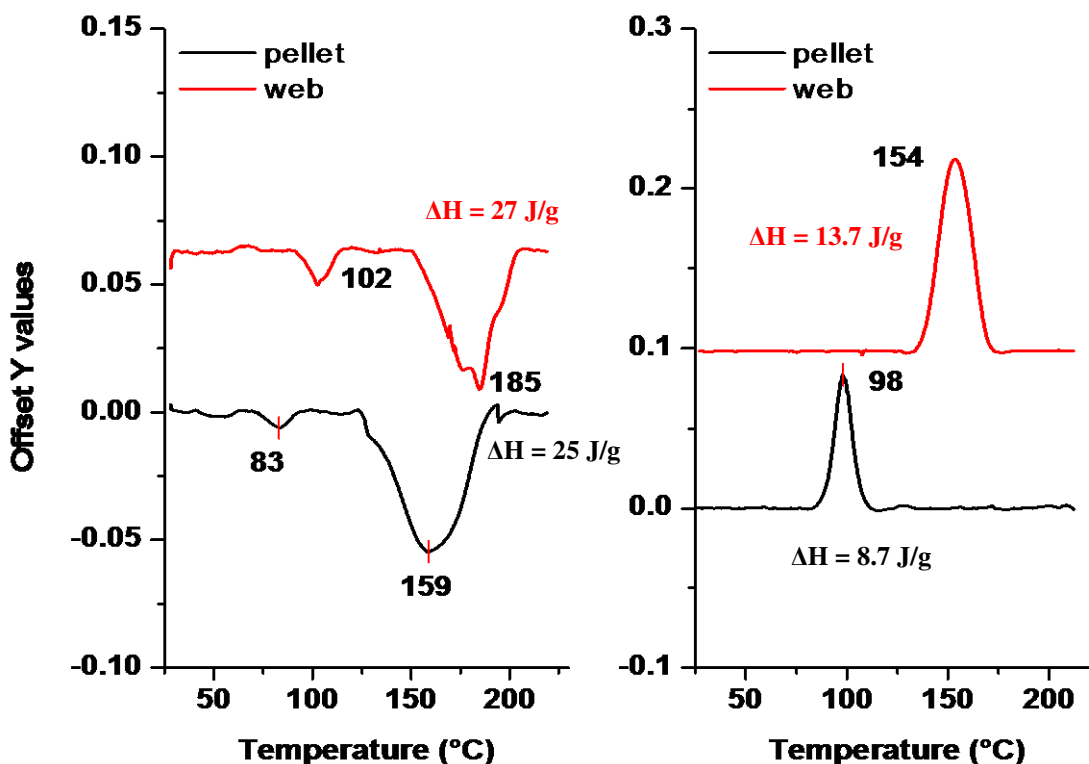
Figure 74. T90A pellet and web melting and cooling curves.

The DSC thermograms of the annealed webs with a control web are presented in Figure 75. T90A webs were annealed at 90°C and 130°C for 4 hours. In the 90°C annealed thermogram, the 1st endotherm has shifted up 8° to 110°C from 102°C in the melt quenched web. No increase in enthalpy ($\Delta H = 8$ J/g) was found. The 2nd endotherm maintained its shape and peak melting temperature however, a 1 J/g increase in ΔH was

observed. In the 130° annealed web, the 1st endotherm has shifted up to and merged with the 2nd endotherm. Consequently, the enthalpy of the second endotherm increased to 35 J/g from 27 J/g in the melt quenched web. The increase in enthalpy of 8 J/g is the amount of enthalpy the 1st endotherm shows for both the melt quenched web and the 90℃ annealed sample. The high end of the 2nd endotherm has also changed shape with an additional peak appearing at a temperature slightly lower than the labeled 185℃ peak. There was no change in the endset melting temperature.

The cooling curves of the control and annealed webs are also presented in Figure 75. Upon annealing, the crystallization kinetics are much slower and the peak crystallization temperature drops to 109℃ for the 90℃ and 130℃ annealed webs from 154℃ for the melt quenched web. The enthalpy decreased from 13.7 J/g for the melt quenched web to 9.2 J/g for the 90℃ annealed web and 10.4 J/g for the 130℃ annealed web. Similar phenomena were also observed by Hu [124] and Martin [131] with annealing of TPUs. They found that a combination of the annealing, DSC heating regime, and isothermal melting before being cooled contributed to an increase in the polyurethanes molecular weight. The increase in molecular weight resulted in lower crystallization temperatures and slightly higher enthalpy, the same as observed here. They found that the molecular weight increase was due to recombination of urethane bonds which were dissociated during melt processing. Many of the these recombination's were found to be branching reactions which along with molecular weight increases would result in decreases in crystallization temperatures.
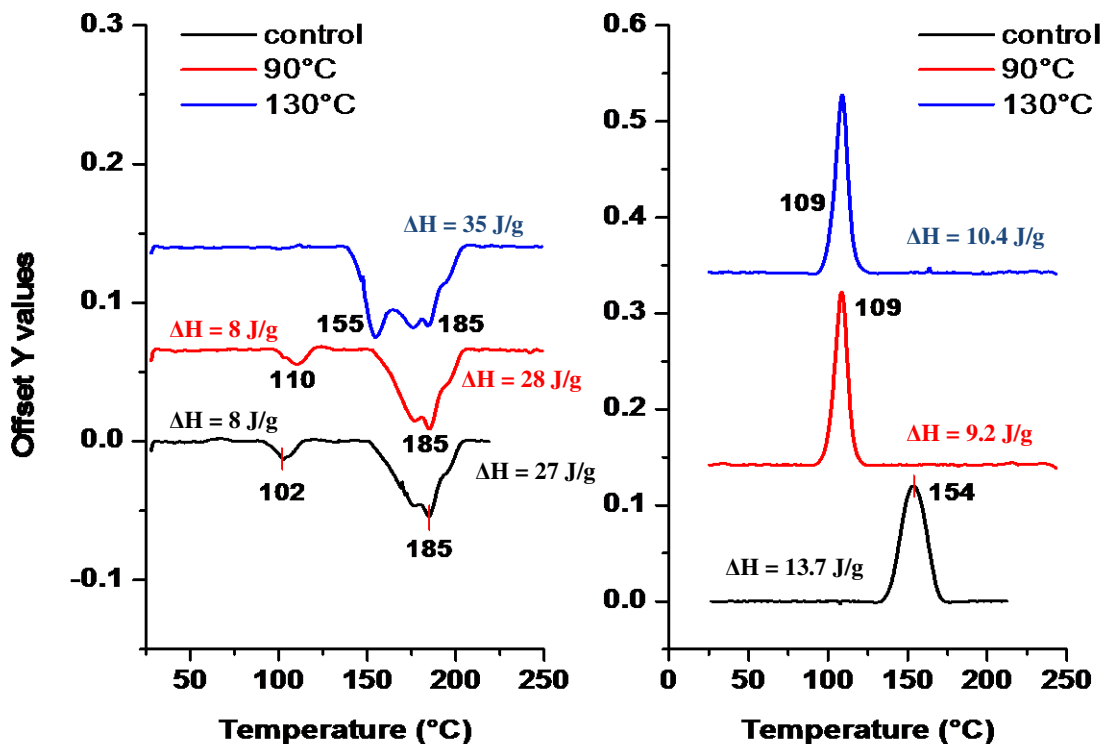
Figure 75. Effects of annealing temperature on T90A webs.

Polyurethanes are known to show multiple endotherms on heating due to various transitions. Their location and cause are dependent on the TPU composition including: length and type of hard and soft segments as well as the chain extender, composition ratio, synthesis or processing route, age, and storage or annealing conditions. The TPUs used in this study were donated by Lubrizol, Inc. on condition the chemistry would not be identified, therefore a literature comparison accompanied with an annealing study was utilized to identify the cause of the 1st endotherm without revealing the nature of the TPU components.

The complex thermal behavior of TPUs is well known and has been reported in numerous publications by Cooper and coworkers [118-123], Koberstein and coworkers [124-129], Martin [130-133], and others [134-137]. In general, 2 or three distinct endotherms are

observed in TPU DSC experiments. Polyurethanes which have a composition ratio of approximately 50% or lower by weight of hard segments have a discrete hard segment domain and show 2 endothermic peaks on heating above the melting temperature. Polyurethanes which contain greater than 50% by weight hard segments have a continuous hard segment domain and show three endothermic peaks with the highest appearing at temperatures of 200°C and above. The TPUs in this study all have two endothermic peaks which are below 200°C and therefore, as expected, all are composed of less than 50% by weigh hard segments.

While it is consensus that the final endotherm observed in heating TPUs in DSC is due to melting of continuous and discrete hard segment microcrystalline domains, the lower temperature endotherms remain ambiguous with identifying their morphological origin. The composition of polyurethanes can vary greatly and therefore show many different thermal behaviors and without knowing the composition ratio of hard and soft segments, the particular hard segment, chain extender, soft segment, and possible additives, identifying the underlying phenomena of the observed endotherms is extremely challenging if not impossible.

Early studies attributed the multiple endothermic behavior at temperatures below the microcrystalline melting endotherm to either hydrogen bond distribution effects or to two types of hydrogen bonds. This was later proven incorrect as polyurethanes incapable of hydrogen bonding were found to show the low temperature endothermic peaks as well. Other researchers have attributed the low temperature endotherms to intradomain ordering [121], the glass transition of the hard segment [134], and enthalpic relaxations [135]. The Koberstein-Stein [1128, 129] model was proposed for polyurethanes which exhibit 3 endotherms. They indicate the 1st endotherm is found approximately 20° above the annealing temperature and is attributed to local reorganization of the hard domains and can be improved by annealing. They explained this by solubility effects for which there is a critical hard segment sequence length below which hard segments dissolve within the soft microphase. At low annealing temperatures, short and long hard segments separate from the soft microphase. At low annealing temperatures, long hard segments

have limited mobility and only short segments can align to form ordered structures. As annealing temperatures increase, shorter hard segments become soluble in the soft microphases and the ordering process is due to progressively longer hard segments and the 1st endotherm eventually merges with the 2nd endotherm. The second endotherm observed between 140 -200°C was attributed to intersegmental mixing of non-crystalline hard and soft segments. They called this the Microphase Separation Transition (MST). The final endotherm observed at temperatures of 200°C and greater was attributed to a combination of an order-disorder transition and microcrystalline domain melting in the hard segment rich phase. Their model is widely accepted for polyurethanes which show 3 endotherms.

Seymour [122, 123] proposed a theory for TPUs exhibiting 2 endotherms. For the 1st endotherm, like Koberstein, he found the 1st endotherm could be improved by annealing resulting in an increase in the peak temperature with increasing temperature and time up to a point in which it merged with the higher endotherm. They concluded that the 1st endotherm represents disruption of short range order of short poorly ordered hard segments within the hard microdomain. The 2nd endotherm was attributed to disruption of long range order and melting of the microcrystalline domains. This theory supports the observed changes in the T90A thermograms presented in Figure 75.

4.3: Compounded TPU/C60 Polymer and Webs

DSC thermograms of the neat and compounded TPU/C60 melt blown webs are shown in Figure 76. No change in the peak temperatures of the 1st and 2nd endotherms in the neat and 0.1% C60 webs are observed. The 1st endotherm peak temperature of the 0.3% C60 web decreases to 91°C. Using the theory by Seymour for occurrence of the 1st endotherm, this indicates the greater concentration of C60 creates a higher degree of disorder of shorter hard segments in the hard domain. The enthalpy of the 2nd endotherm decreases with increasing concentration of C60 indicating the C60 inhibits the amount of

crystallinity obtained in the webs. As with the 1ˢᵗ endotherm, the C60 creates a higher degree of disorder, preventing the hard segments from aligning and crystallizing into microcrystalline domains. The cooling curves in Figure 76 show very little change in the crystallization kinetics.
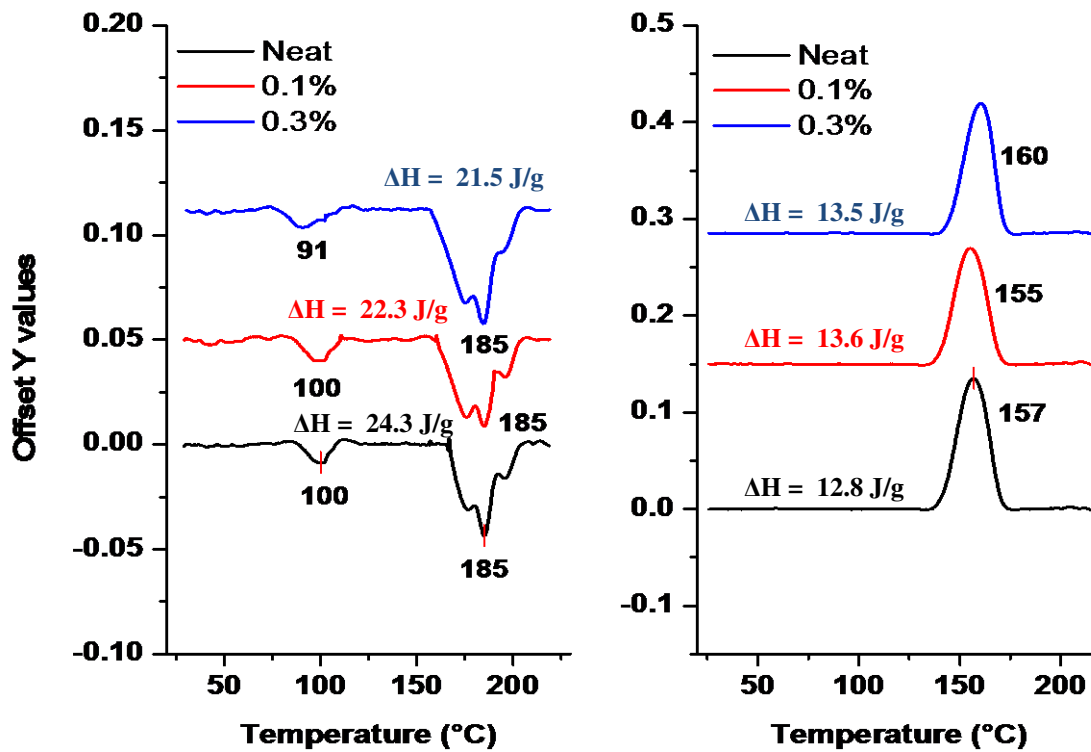
Figure 76. Melting and cooling curves of T90A/C60 compounded webs.

SEM Imaging

Scanning electron images of the neat and TPU/C60 at 0.1% wt loading collected at 20, 30, and 40 cm die-to-collector distances are shown in Figure 77. The degree of fiber entanglement and roping in the webs is seen to increase with increasing DCD. Total fiber adhesion is seen to occur to a greater extent in the TPU/C60 at 0.1% wt loading at 40 cm DCD compared to the neat webs.
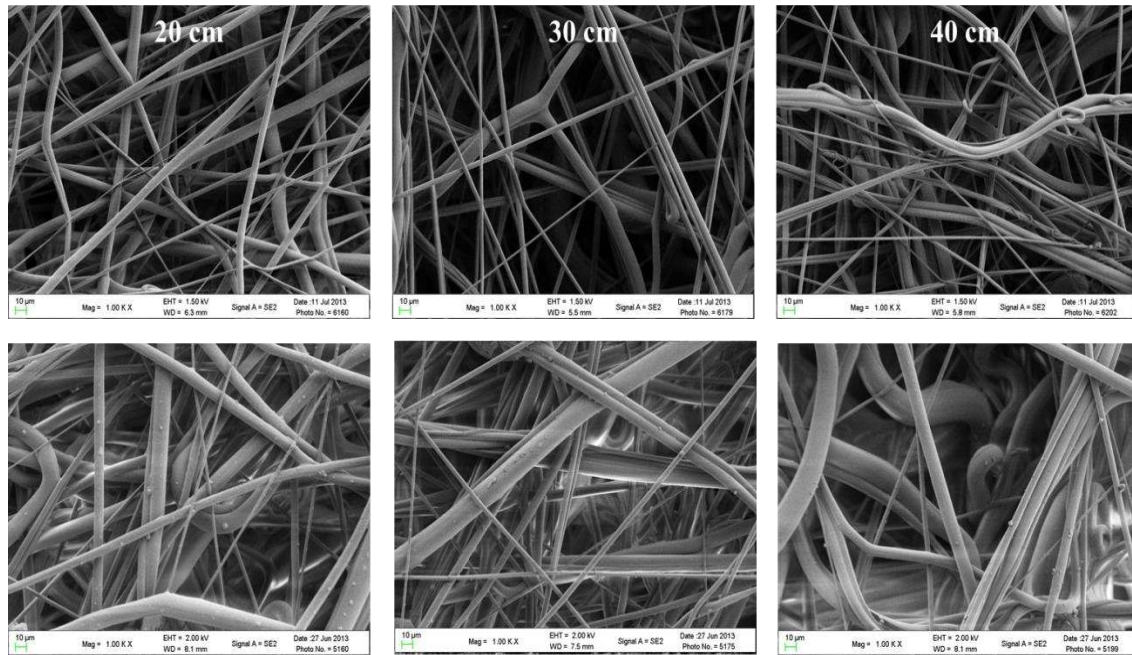
Figure 77. Neat (top) and TPU/C60 at 0.1% wt loading (bottom) at 20, 30, and 40 cm DCD.

Figures 78 and 79 show images of the TPU/C60 webs at 0.1% wt and 0.3% wt loading collected at 30 cm DCD respectively. The C60 is clearly seen embedded in the surface of the 0.1% wt webs but not the 0.3% wt webs. Close examination of the 0.3% wt web

images shows the fibers are larger and there is a much greater degree of total fiber-to-fiber adhesion. This could be due to differences in the rheological properties of the resins with addition of C60 nanoparticles at different loadings. With larger fiber diameters, it is possible the C60 is able to remain embedded in the fibers.
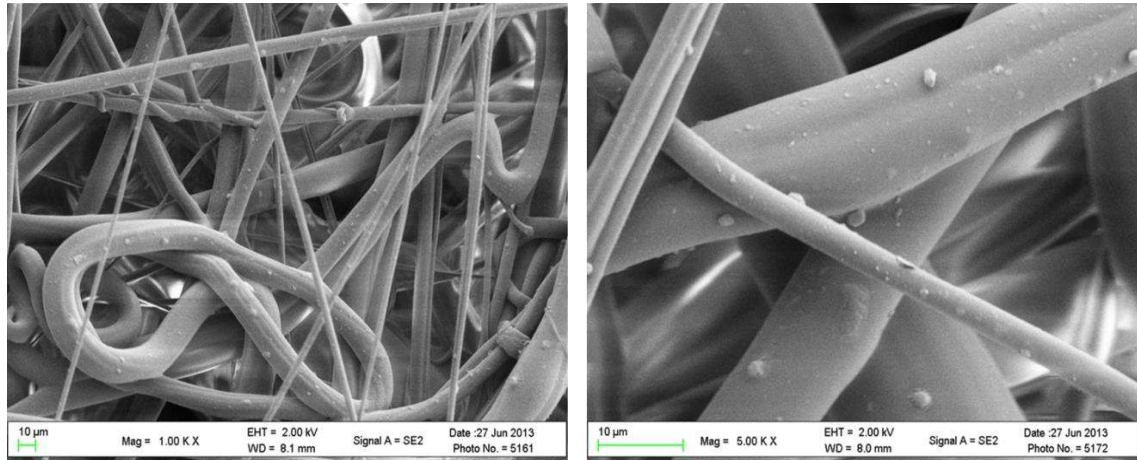
Figure 78. Melt blown TPU/C60 webs at 0.1% wt. C60 loading collected at 30 cm DCD.
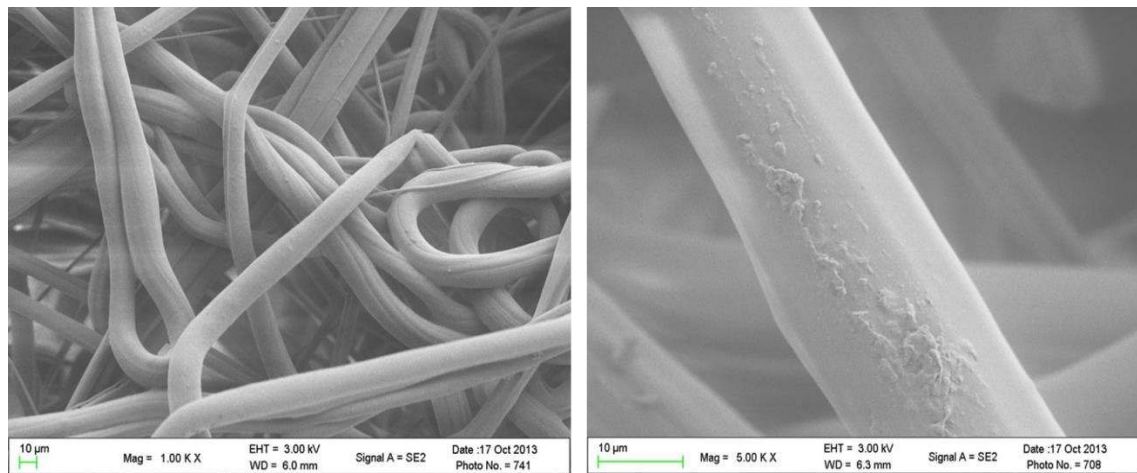
Figure 79. Melt blown TPU/C60 webs at 0.1% wt. C60 loading collected at 30 cm DCD.

Fiber Diameter and Distribution

The average fiber diameters of the webs collected at increasing DCDs are shown in Figure 80. The average fiber diameter increases with increased C60 loading. The control webs show a slight decrease in average fiber diameter with increasing DCD from 5.3 um at 20 cm to 3.9 um at 40 cm. This is likely due to the fibers chosen for measurement as it is known that DCD has little to no effect on fiber diameter past 10 cm. Fibers which show adhesion to other fibers are not measured and there is a greater degree of total fiber adhesion with increasing DCD leaving fewer fibers to measure. Air turbulence in melt blowing becomes uneven with increasing distance from the die and fibers come into contact with neighboring fibers and consequently adhere to one another. The TPU/C60 webs at 0.1% wt loading maintain an average fiber diameter of ~6.5 um with increasing DCD while the 0.3% wt loaded web has an average fiber diameter of ~ 7 um. The error (standard deviation) is also seen to increase with C60 loading. The fiber diameter histograms in Figure 81 show this clearly. The control webs show a decreasing distribution as the DCD is increased. The TPU/C60 webs with 0.1% wt loading show a larger distribution but the web collected at 30 cm DCD shows optimal collection with the narrowest distribution at that loading. The TPU/C60 web a 0.3% wt loading shows a large distribution with fiber diameters up to 18 um measured. Note the larger scale of the 0.3 % wt graph while the control and 0.1% wt loading graphs have equal scales.
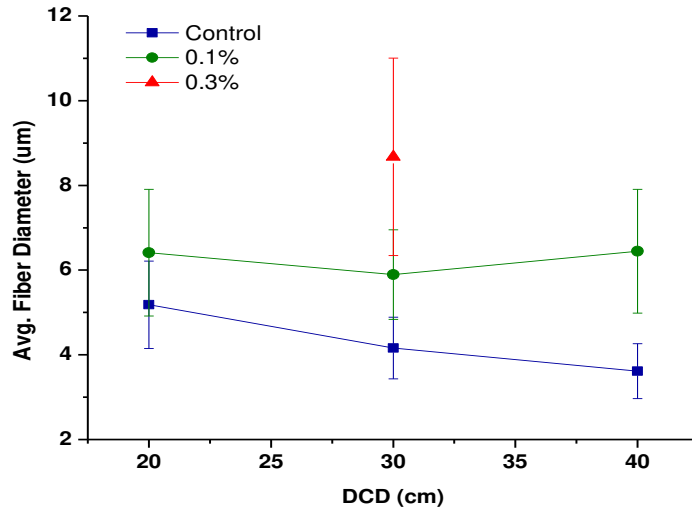
Figure 80. Average fiber diameter of T90A/C60 webs as function of DCD.
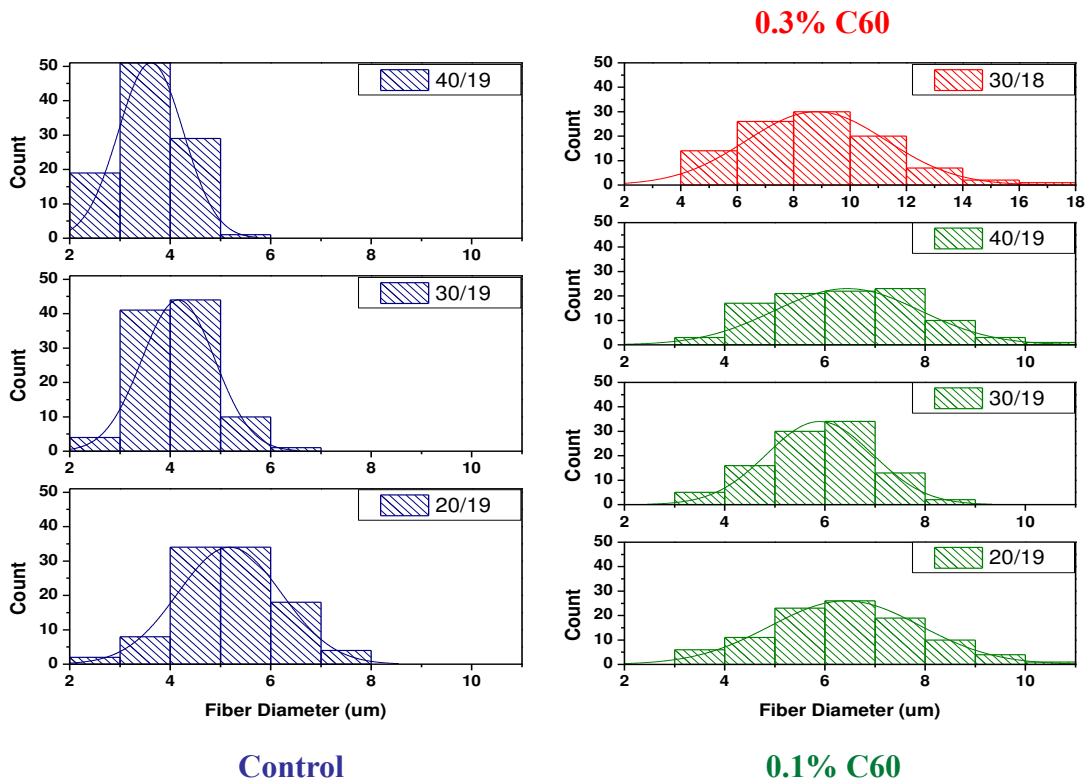
Figure 81. Fiber distributions of T90A/C60 webs.

Break Strength and Elongation

Break strength and elongation as a function of DCD are shown in Figure 82. Break strength decreases with increased C60 loading. The web strength is approximately equal with increasing DCD from 10 to 30 cm DCD. With further increase to 40 cm the neat and 0.1% webs show approximately equal drops in strength. A discussed previously, this is due to a lower degree of fiber-to-fiber bonding. The elongation at break increases with C60 loading however the 0.3% falls between the neat and 0.1% C60 webs.

Typically, addition of high modulus nanoparticle to polymers increases their strength and decreases the elongation properties. The opposite effects are observed in these materials. This is likely due to the fact that nonwoven mechanical properties are dominated by the web properties involving fiber-to-fiber bonding, entanglements, and roping. However, as shown in Figure 76, these webs crystallized at approximately the same temperature so they should have approximately the same degree of fiber-to-fiber contacts at the respective DCDs. Therefore, it is likely that the differences in the mechanical properties are due to the degree of fiber entanglement, roping and fiber diameter. It is well known that fibers with smaller diameter are show greater strength than larger fibers. It was observed in Figures 80 and 81that fiber diameter in these webs increased with increased C60 loading.
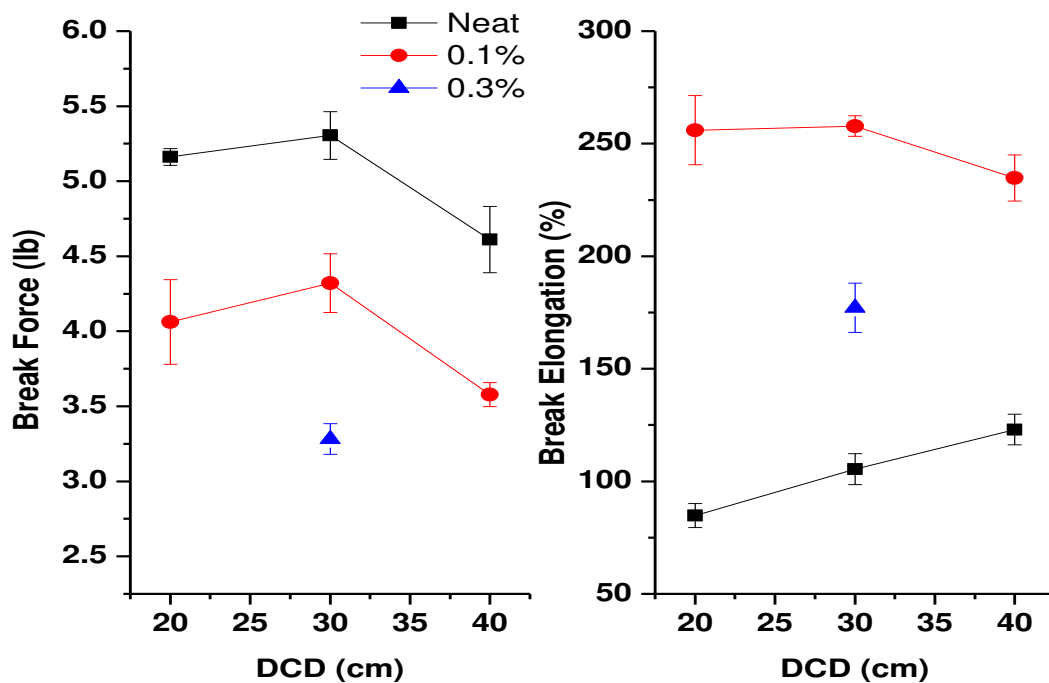
Figure 82. Break force and elongation of T90A/C60 webs in the machine direction.

Pore Size

The average pore diameter was found to show a large increase with loading of C60. (Figure 83). The neat and 0.1% samples show similar trends with increasing DCD. There was little change in average pore diameter from 20 to 30 cm DCD and an increase in diameter at the 50 cm DCD due to a high degree of total fiber adhesion.

Air Permeability and Pore Size

The air permeability is presented in Figure 83. As expected after analysis of the average pore sizes, the loaded samples had higher permeability values. The permeability of the

0.1% shows a steeper increase with increasing DCD compared to the neat samples. The 0.3% shows a much larger increase in air permeability when compared to the average pore size increase from 0.1% to 0.3% C60. This indicates a broader distribution of pore sizes with larger pores having a greater influence on the air permeability.
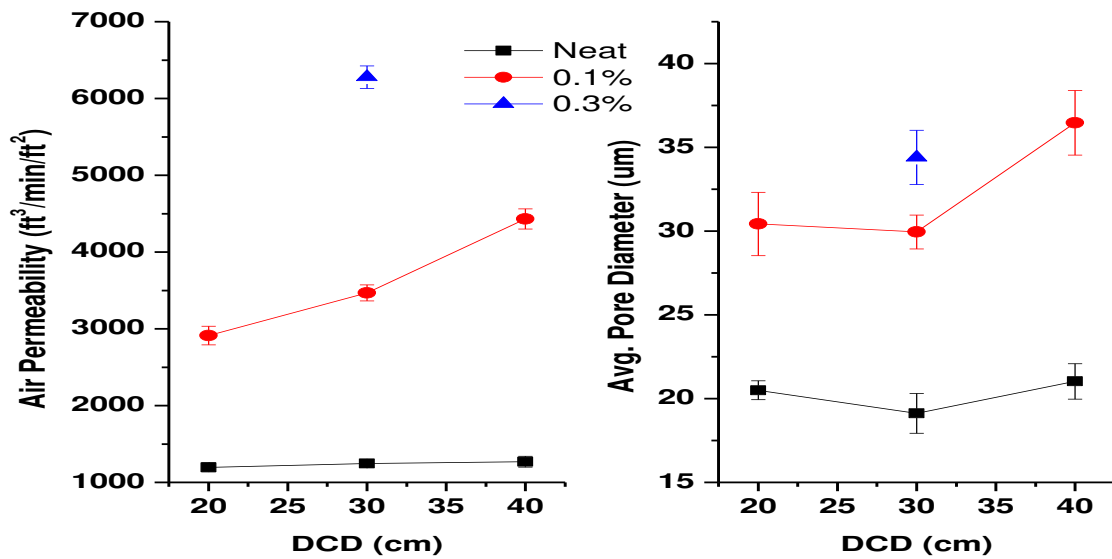
Figure 83. Air permeability and avg. pore diameter of TPU/C60 webs.

CHAPTER 5: Nano-reinforced Sandwich Composite Results

5.1: Dip Coating

Continuous Dip Coating

SEM images of continuously coated Estane/30B webs of 1 and 5% are shown in Figure 84. It is clear that the 5% sample contains more nanoclay than the 1%. This was observed in numerous samples. The dispersion of the clay however is not uniform. While some smaller clay particles are seen, most are agglomerated in patches spread about.
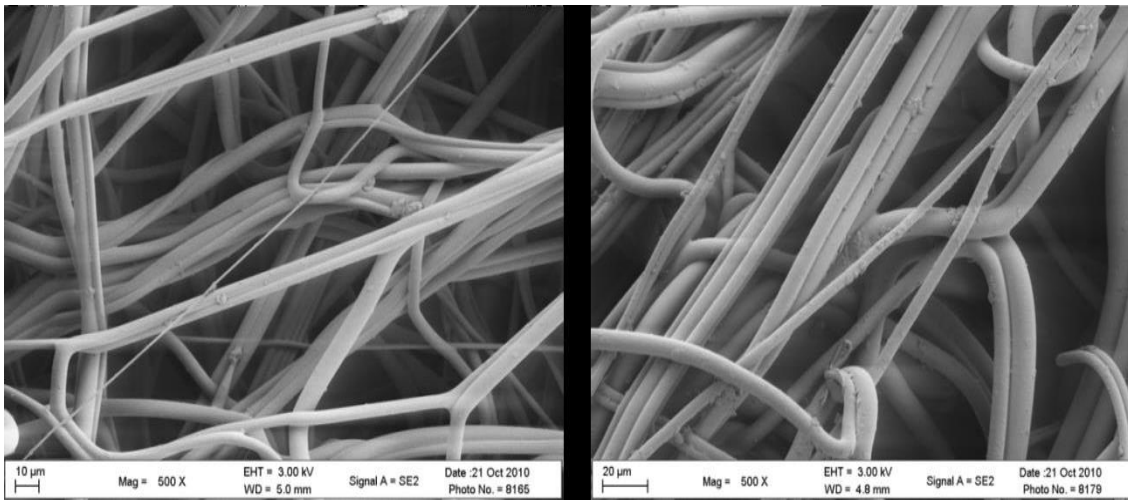
Figure 84. Estane TPU continuously coated with Cloisite 30B nanoclay. a.) 1%, b.) 5%

DMA results are presented in Figure 85. These 30 gsm webs were hot pressed into 16 layer sandwiches with 115°C heat at 120 seconds under 11 tons of pressure. Both E' and E" are reduced with loading of nanoclay. It was noticed during the coating process that the webs were heavily saturated with solvent. With this heavy saturation, the dryer had

to be set at 130°C to dry the webs before winding. The combination heavy solvent saturation and high drying conditions is believed to be the cause for the observed decreases in E' and E". The poor nanoclay dispersion is likely to have also contributed to the observed decrease.
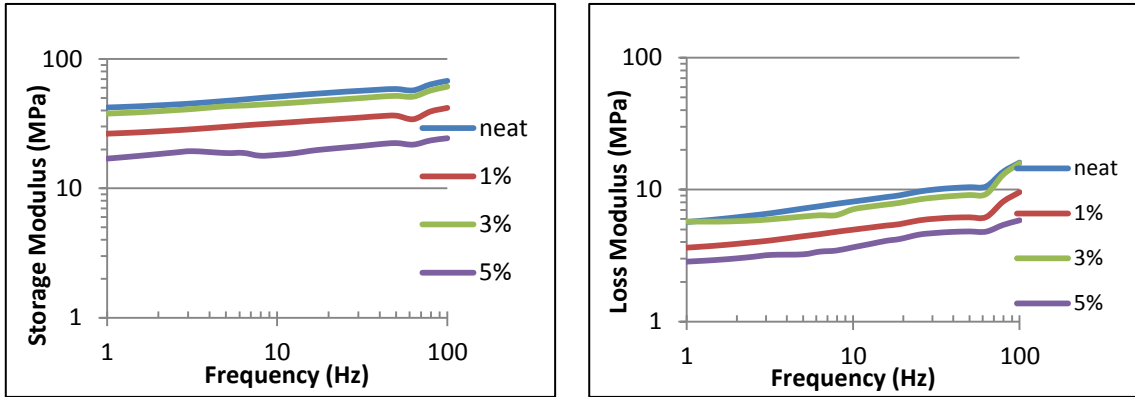
Figure 85. DMA of 16 layer continuously coated webs with Cloisite 30B nanoclay.

Individual Dip Coating

DMA scans of the Cloisite 30B nanoclay single coated webs is shown in Figure 86. These 100 gsm webs were hot pressed into 4 layer sandwiches at a temperature of 90°C for 55 seconds and 11 tons of pressure. E' shows a slight increase for the 5% loaded sample while the 3% and 1% loaded sandwiches decreased E'. The 1% loaded sandwich showed an extremely large decrease. E" showed an increase with 3% and 5% loadings.
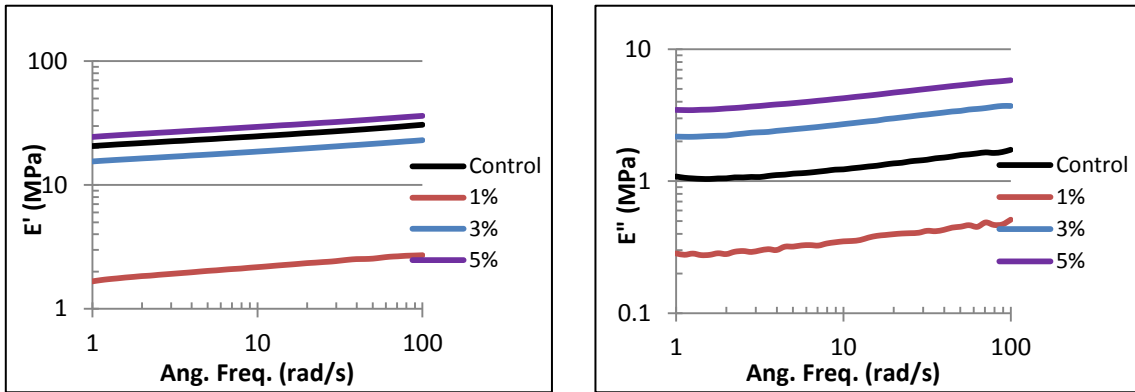
Figure 86. DMA of 4 lay individual coated Cloisite 30B nanoclay samples.

The DMA results of the frequency sweeps on the C60 4 layer single coated sandwiches are shown in Figure 87. These sandwiches were pressed under the same conditions as the 4 layer nanoclay coated sandwiches. No increase in E' or E" was observed. The control sample in the E' graph is overlaid with the 3% loading curve. The SEM images of the C60 single coated webs at 1 and 5% are presented in Figure 88. Aggregation and agglomeration is clearly visible and likely the cause of decreased E' and E". The degree of aggregation and agglomeration increases with increased loading.
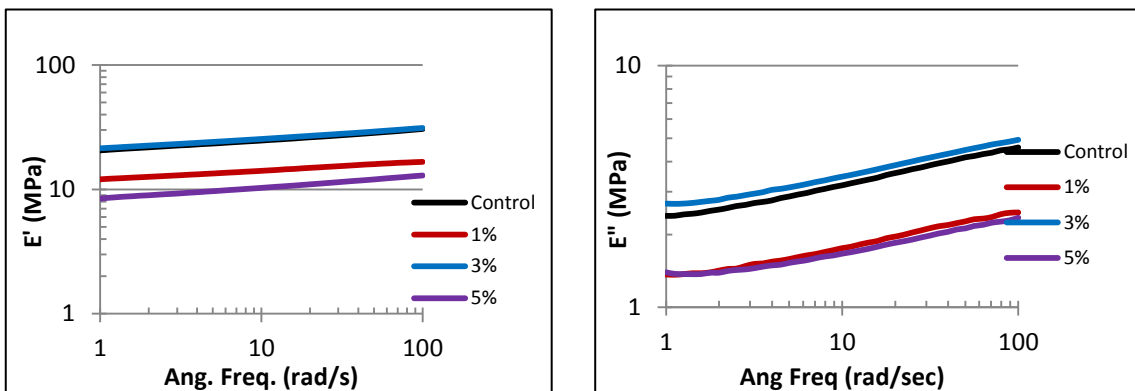
Figure 87. DMA of 4 layer single dip coated C60 composites.

128
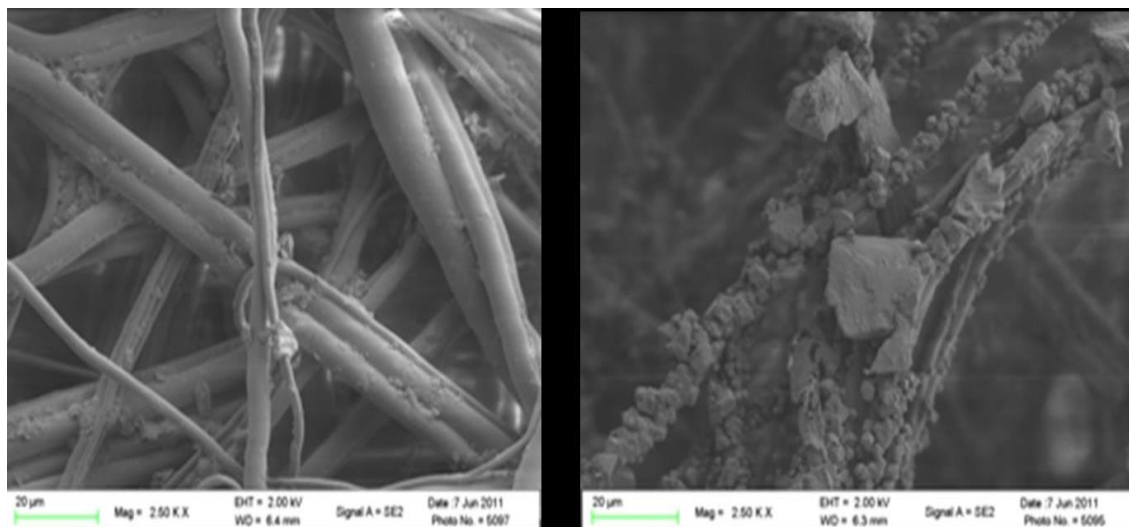
Figure 88. Single dip coated C60 webs. a.) 1%, b.) 5%

5.2: Continuous Ultrasonic Spray Coating

Trial 1

SEM images of the webs from Trial 1 are presented in Figure 89. As the POSS is a clear gel at room temperature, it is difficult to see on the fiber surface. The C60 webs show even dispersion but the fillers formed small aggregates. Aggregation increased with increased 60 loading.
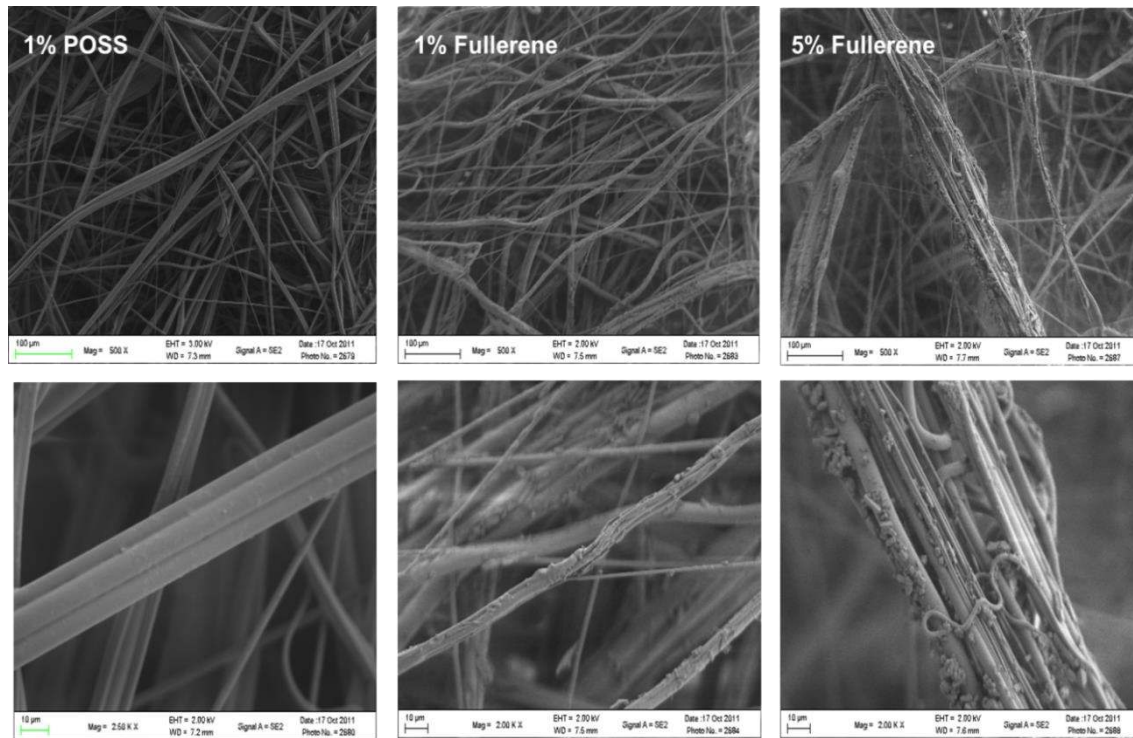
Figure 89. SEM images of Trial 1 sprayed webs.

The 4 layer sandwich composites were hot pressed at 90°C for 55 seconds with 11 tons of pressure. Figure 90 shows the DMA results for the C60 sandwich composites from Trial 1. All wt%'s show clear improvement in E' and E" over the control sample with the 1% having the largest increase and 5% the least. The POSS samples (Figure 91) show the 5 wt% giving a small improvement in E" while E' is reduced with POSS loading. Overall, the 1 % C60 showed the largest increase over the control with E' = ~90 MPa at 100 rad/s from ~ 30 MPa. Some delamination was visible in the samples after testing. This could have generated lower values for E' and E" therefore Trial 2 samples were pressed at longer times and temperatures. Also, observation of the process and SEM images indicated the spray system optimal volume flow rate ranged between 20 and 30 ml/min with belt speed at approximately 0.5 m/min.

130
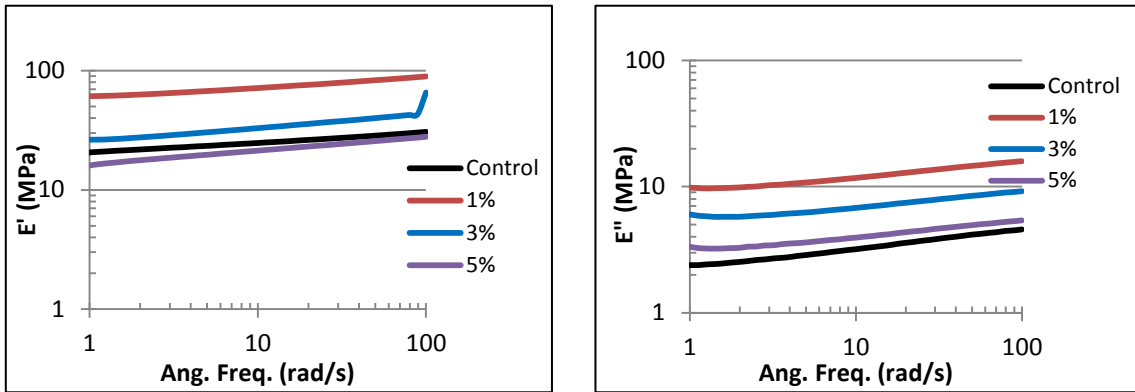
Figure 90. Trial 1 DMA results for C60 sandwich composites.
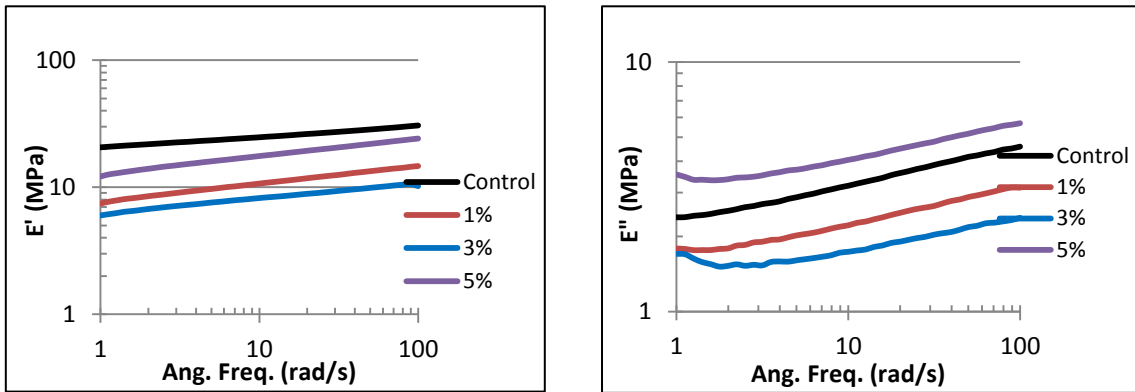
Figure 91. Trial 1 DMA results for POSS.

Trial 2

Figures 92-94 show the sprayed surface of the TPU web with C60, graphite, and INT's respectively. The dispersion of the C60 was much better than that in Trial 1 though some 2-4 micron aggregates can be found in random patches with increaing add on percent (Figure 92).
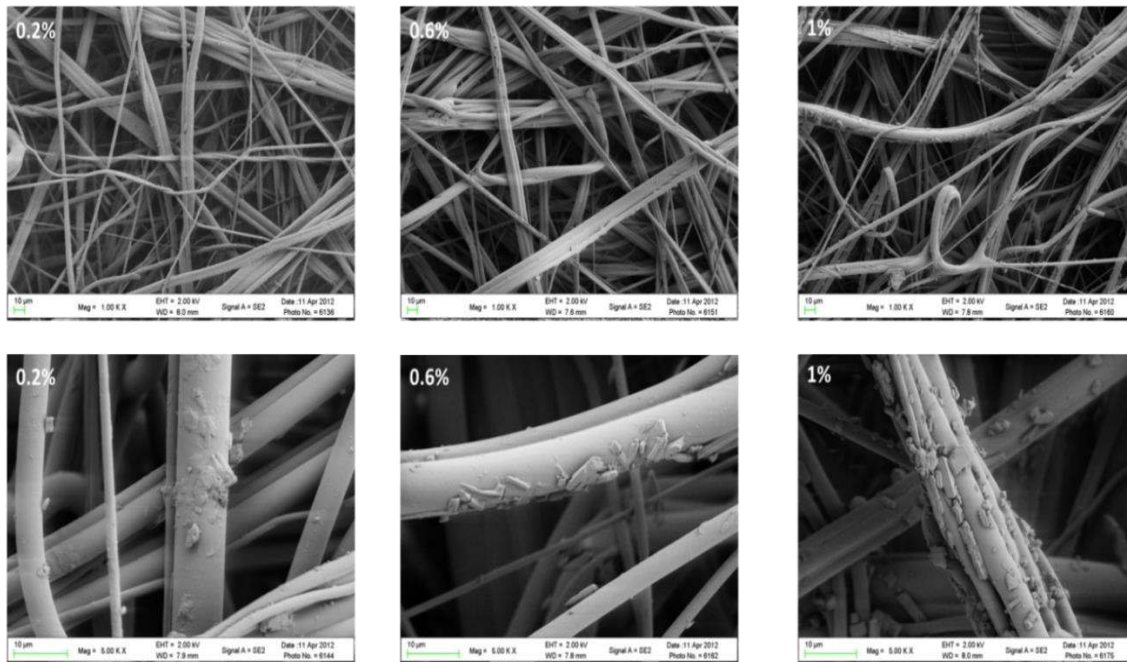
Figure 92. SEM images of C60 sprayed webs form Trial 2. (1000 and 5000 magnification)

The graphite webs show excellent dispersion with only a few very small aggregates visible (Figure 93). The INT's also had good dispersion with very few aggregates (Figure 94). The surfactant is also seen as a film connecting adjacent fibers.   This may have limited the degree to which E' and E" increased with additon of the INTs. The INTs have the greatest strength of all the nanofillers used in this reasearch and

consequently it was expected they would have given the greatest increase in moduli, especially with the good dispersion observed in the SEM images.
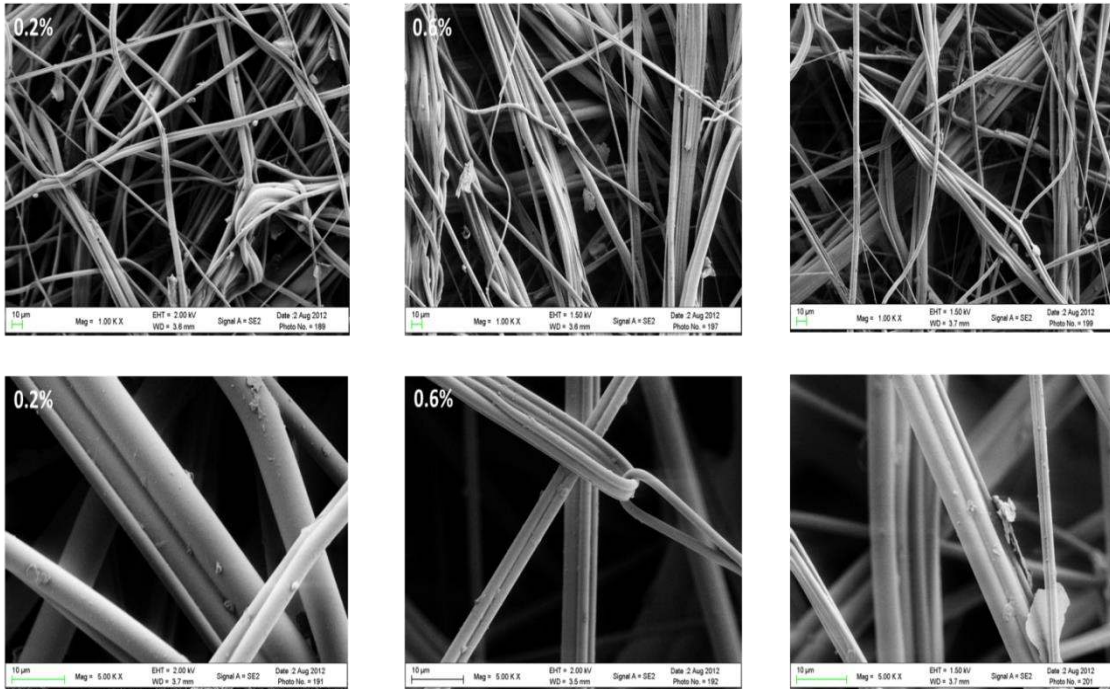
Figure 93. SEM images of graphite sprayed webs from Trial 2. (1000 and 5000X)
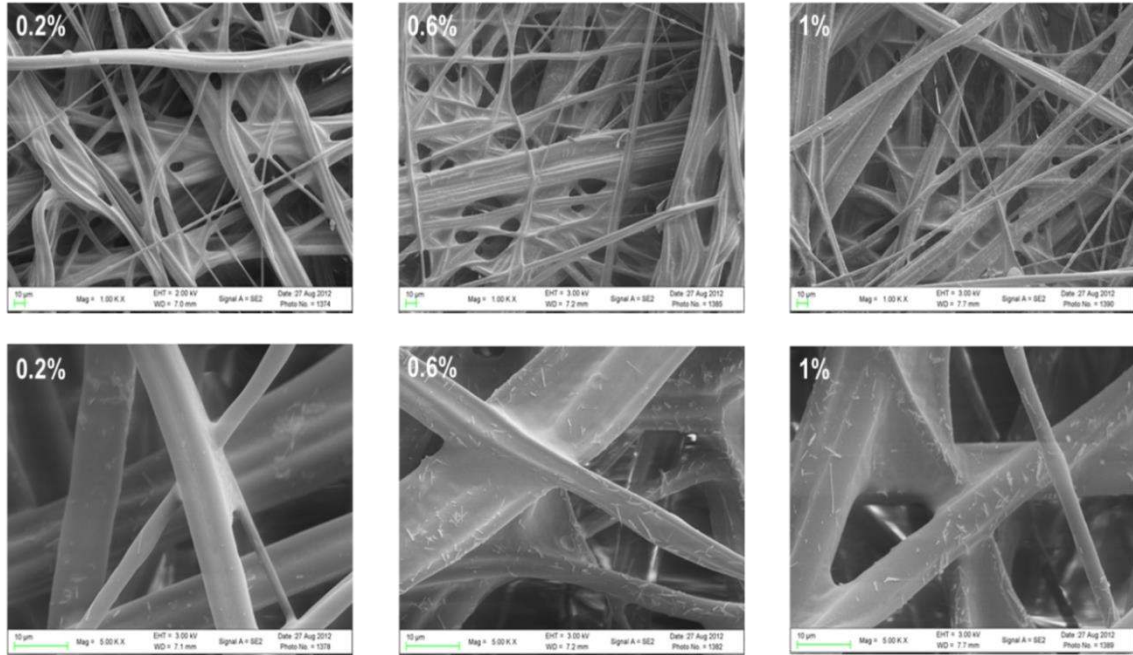
Figure 94. SEM images of INT sprayed webs from Trial 2. (1000 and 5000X)
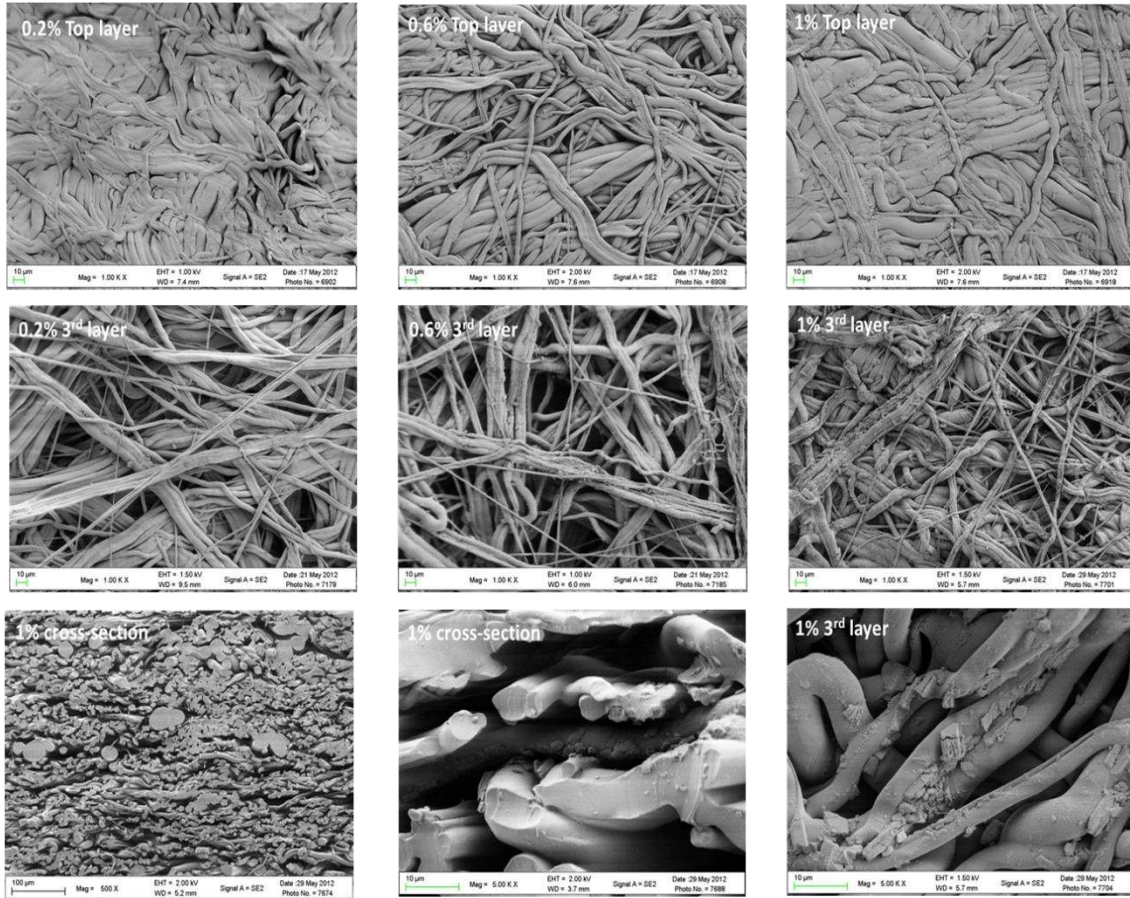
Figure 95. SEM imagers of hot pressed C60 sandwich composites: top layer, 3rd layer, and cross-section.

Figures 95 and 96 show SEM images of the top layer, 3rd layer, and cross-sections of the C60 and graphite sandwich composites. As clearly seen, the fiber structure was maintained with the hot pressing for sandwich composite fabrication.
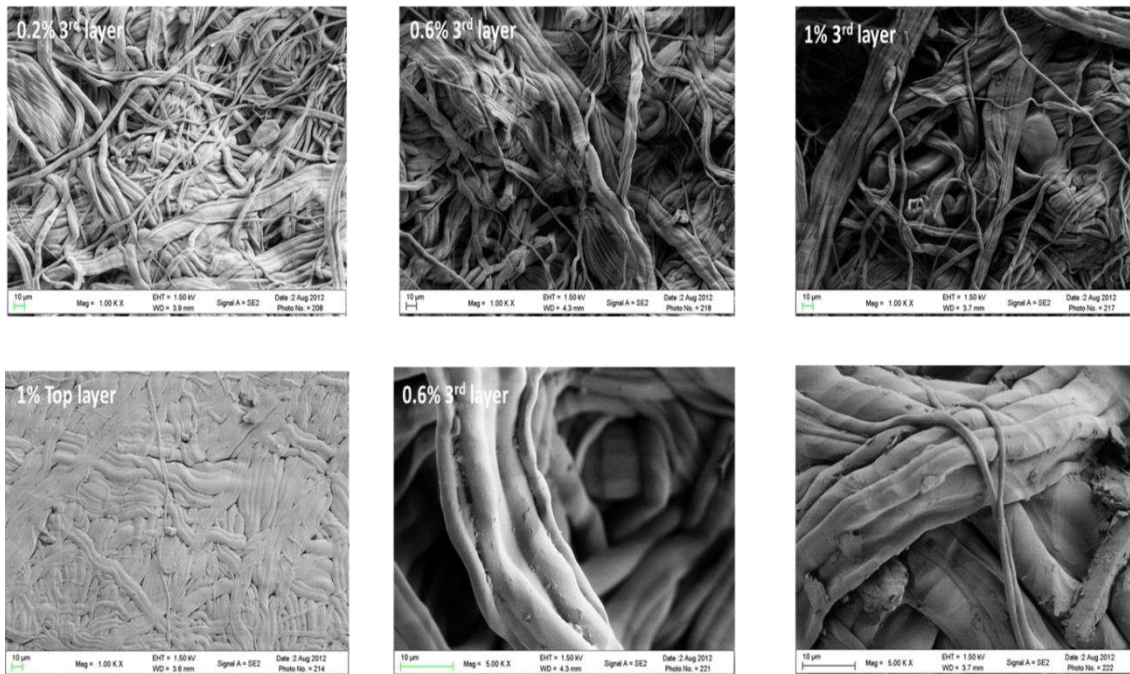
Figure 96. SEM imagers of hot pressed graphite sprayed webs of 3rd and top layer.

The DMA results for Trial 2 are presented in Figures 97-99. As delamination was noticed in Trial 1 ssamples, hot pressing of the Trial 2 4 layer sandwich composites were performed at 95°C for 60 seconds with 11 tons of pressure. No delamination was visible after testing. The 0.2 wt% for all three nanofillers showed the largest improvement in E' and E" due to the better dispersion observed in the respective SEM images.
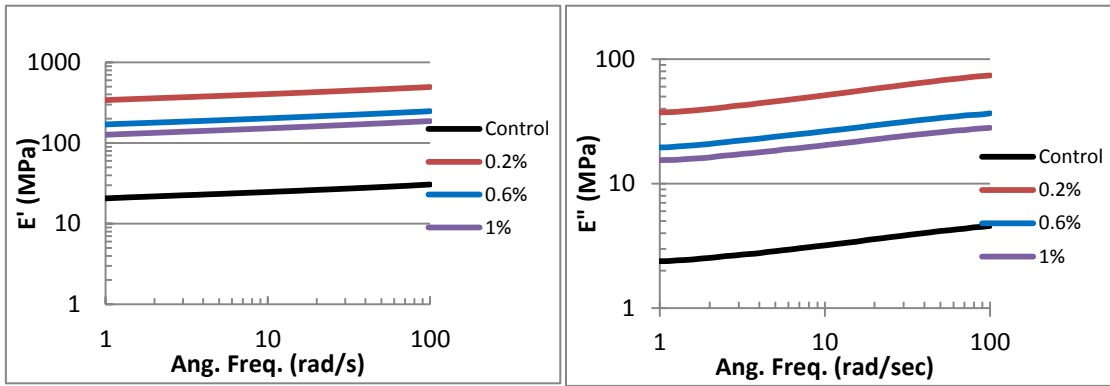
Figure 97. Trial 2 C60 4 layer sandwich composites.
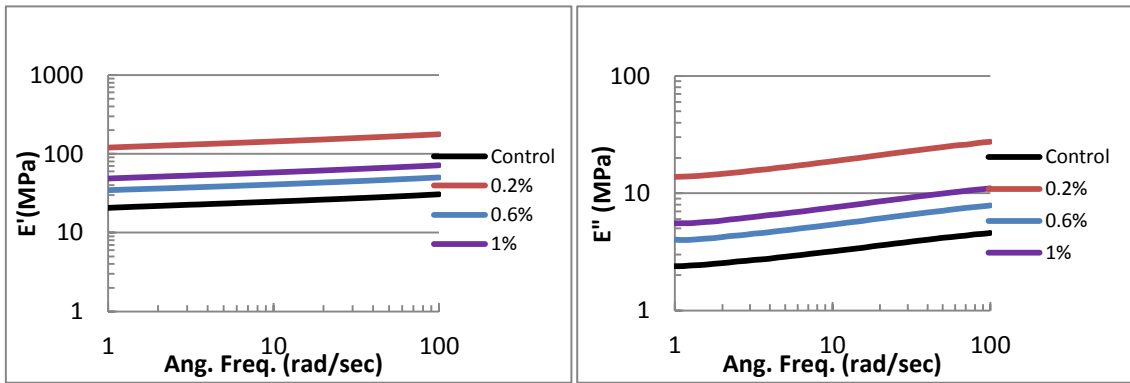
Figure 98. Trial 2 Graphite 4 layer sandwich composites.
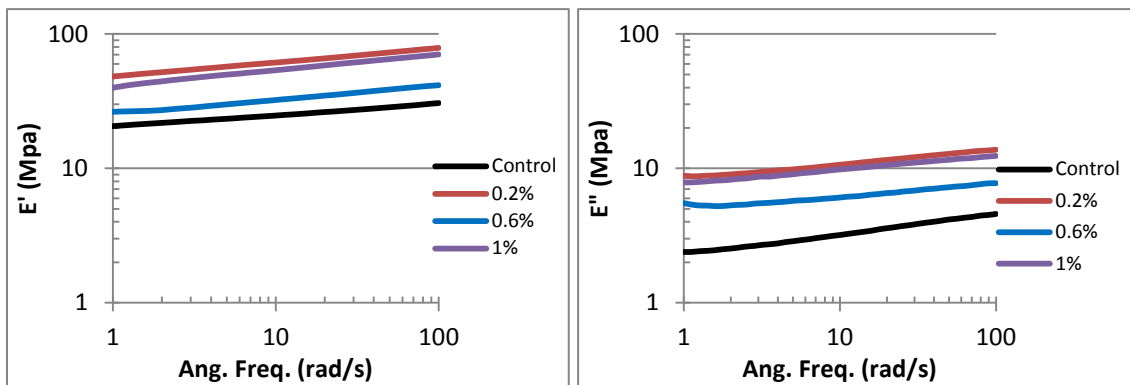
Figure 99. Trail 2 INT 4 layer sandwich composites.

Table 12 summarizes the E' and E" averages at 1 and 100 rad/s of Trial 2. The 0.2 wgt% C60 shows the largest improvement reaching an E' of 495 MPa. This is more than a 15 fold increase over the control, 30.6 MPa. This is also much larger than the 90 MPa of the 0.2 wt% achieved in Trial 1. The 0.2 wt% graphite E' improved to 177 MPa while the 0.2 wt% INT's E' was 78.8 MPa at 100 rad/s. There was not any literature found in which nanoparticles have been sprayed onto nonwoven surfaces or even polymeric materials to reference results of this type of nanocomposite. However, research on nanocomposites in which the nanoparticles are embedded into the matrix have shown improved storage and loss modulus at low concentrations of nanoparticles but not to the levels observed here [99-101].

Table 12. Summary of DMA data at 1 and 100 rad/s for Trial 2.

wt%	E' (MPa)		E" (MPa)	
C60	1	100	1	100
0	20.6	30.6	2.39	4.58
0.2	340	495	37.4	73.9
0.6	170	249	19.6	36.7
1	127	187	15.4	28.1
Graphite				
0.2	120	177	13.8	27.5
0.6	34.6	50.2	4.02	7.86
1	48.6	71.5	5.54	11.1
INT				
0.2	48.2	78.8	8.81	13.8
0.6	26.4	41.6	5.52	7.75
1	39.8	70.4	7.86	12.4

5.3: TPU/C60 Compounded Sandwich Composites

Figure 100 shows a frequency sweep of the 4 layer TPU/C60 compounded sandwich composites and the neat sample. The samples were hot pressed at 95°C for 45 seconds with 11 tons of pressure. The 0.3% loaded sample shows a clear improvement of ~ 20 MPa or 25% across the frequency range for E' and E". The 0.1% sample shows only a very small improvement and is essentially overlaid on the neat sample. All samples show an increasing slope over the frequency range tested.
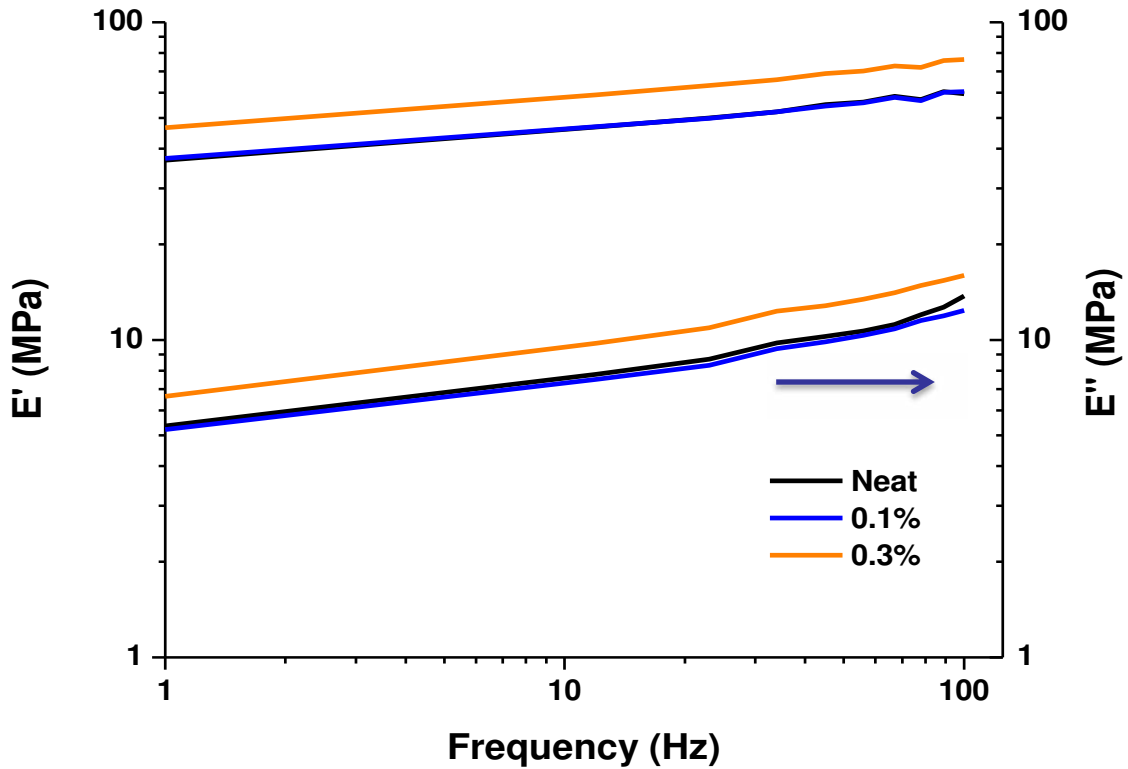
Figure 100. Frequency sweep of 4 layer neat and TPU/C60 compounded sandwich composites.

Temperature scans of are shown in Figure 101 for 10 and 100 Hz. The 0.3% sample shows a good improvement in E' and E" over the entire temperature range while the 0.1% sample is overlaid on the neat sample data showing no improvement. The tan delta curve shows no improvement in dampening with addition of C60 at the loadings investigated however, there is a clear improvement in the E" curve with 0.3% loading. The lack of improvement in the tan delta is due to the equal improvement in the E' and E" curves as the ratio for tan delta stays the same. The 100 Hz scan shows an increased Tg to 16.8°C from 8.43°C at 10 Hz. All samples show the same Tg for both scans indicating addition of C60 at the loadings investigated had no effect on the soft segment mobility.

The DMA results presented in Figures 100 and 101 show similar improvements in storage and loss moduli observed by other researchers for addition of carbon nanotubes to polyurea [41] and polyurethane [94-98]. Similar results were also found for addition of cellulose nanocrystals and silica nanoparticles to polyurethane [100, 101].
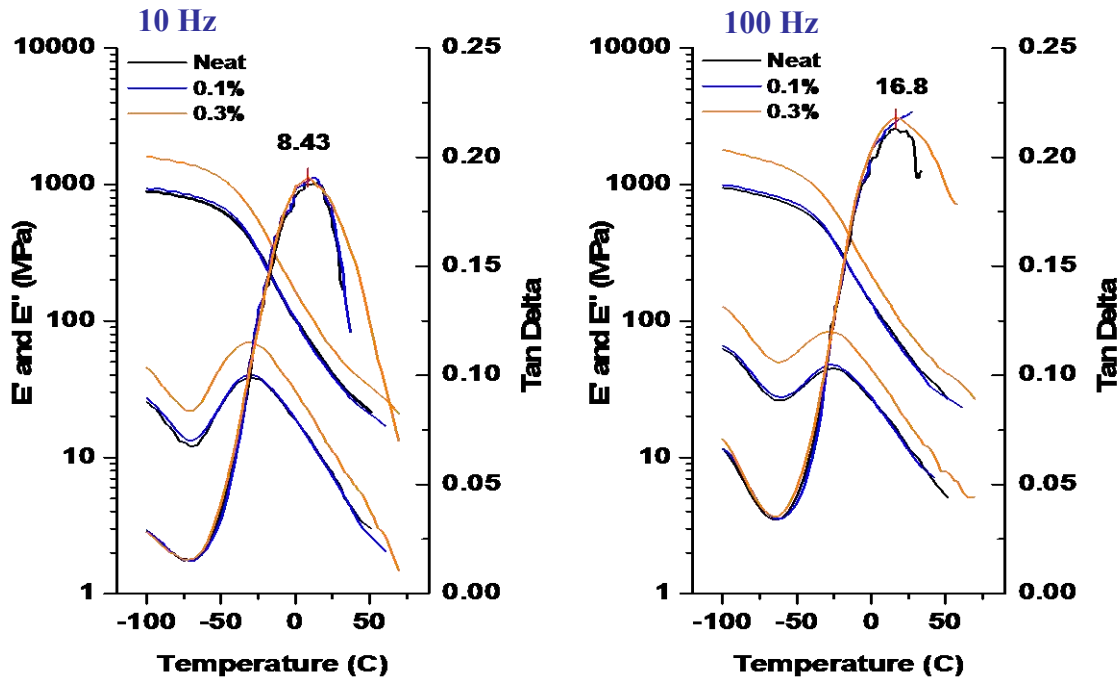
Figure 101. Temperature scan of 4 layer neat and T90A/C60 compounded sandwich composites at 10 and 100 Hz.

5.4: Spray and Compounded C60 sandwich Composite Comparison

Figure 102 shows bulk density of the T90A polymer, T90A single layer web, T90A (Control) 4 layer sandwich composite, C60 sprayed 4 layer sandwich composites, and C60 compounded 4 layer sandwich composites. The sprayed webs are abbreviated a S*yy* and compounded webs as C*yy* where S and C stand for sprayed and compounded while *yy* is the % C60 loading. The T90A polymer has a density of 1.14 g/cc and the T90A single layer web has a bulk density of 0.221 g/cc. Therefore the T90A single layer web has ~ 80% porosity. The C60 sprayed 4 layer sandwich composites show a gradual increase in bulk density with increase C60 % wt add on from the T90A control, indicating less porosity with increasing sprayed C60 content. The compounded C60 4 layer sandwich composites both show a lower bulk density than the control x4 sandwich,

141

indicating greater porosity. This coincides with the air permeability and pore size data of the melt blown C60 compounded web data in Figure 83.
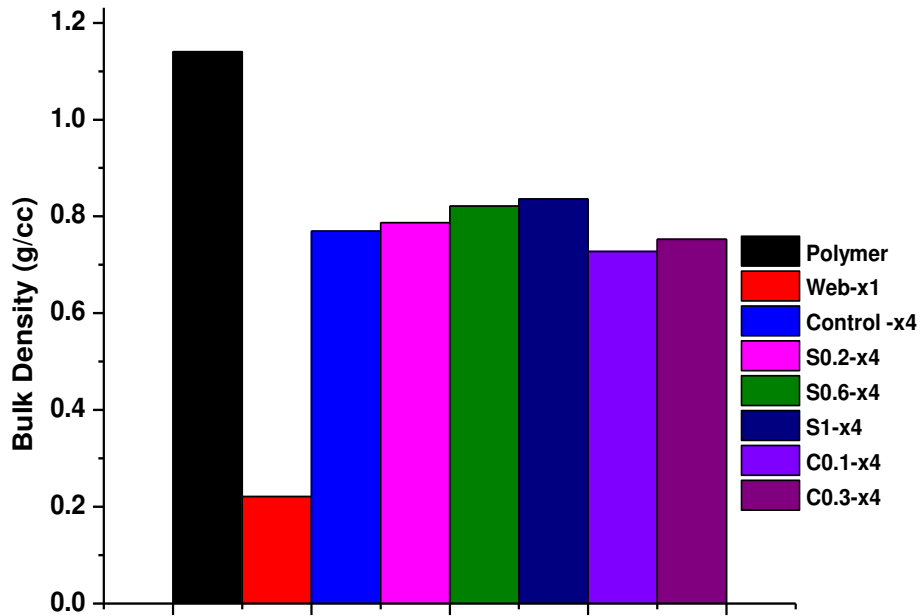
Figure 102. Bulk Density

An estimate of the storage modulus (E') of the compounded and sprayed sandwich composites may be theoretically found using the rule of mixtures for upper (Eq. 24) and lower (Eq. 24) cases and compared with the experimental results [119 – 121]

$$E_c = E_M \phi_M + E_{C60} \phi_{C60} \qquad (24)$$

$$\frac{1}{E_c} = \frac{\phi_M}{E_M} + \frac{\phi_{C60}}{E_{C60}} \qquad (25)$$

Here, E_c is the storage modulus of the sandwich composite, E_M is the storage modulus of the sandwich composite without C60 loading (59.5 MPa for the compounded and 30.6 for the sprayed control sandwich composites at 100 Hz). The difference in the compounded and sprayed sandwich composite moduli arises from the different web structures developed with the different process conditions and equipment used in melt blowing the webs. E_{C60} is the modulus of the C60 nanoparticles (14 GPa [89]), while ϕ_M and ϕ_{C60} are the volume fractions of the sandwich composite and C60 which sum to unity. Mass fraction was related to volume fraction by $\phi_{C60} = M_f * \rho_M/\rho_{C60}$, where ρ_M (1.14 g/cc [126]) and ρ_{C60} (1.72 g/cc [89]) are the sandwich composite and C60 densities respectively. The theoretical and experimental storage moduli for the C60 compounded and sprayed sandwich composites are sown in Table 13.

Table 13. Theoretical and experimental storage moduli.

Reinforcement Method	Weight %	Volume Fraction	Theoretical E' (MPa)		Measured E' at 100 Hz(MPa)
			Upper Bound	Lower Bound	
Compounded	0.1	0.0007	69.3	58.8	60.4
	0.3	0.0020	87.4	59.6	76.4
Sprayed	0.2	0.0013	32.4	30.6	495
	0.6	0.0040	86.5	30.7	249
	1.0	0.0070	123	30.8	187

The experimental values of E' for the compounded samples fall between the calculated theoretical upper and lower bound values for both weight percent's. For the sprayed samples, the model severely underestimates the measured moduli. This could be due to a discrepancy of the loading of C60 produced during spraying. The system pumps the nanoparticle solution from the bottom of the reservoir and if the C60 settles during the process, the solution at the bottom of the reservoir will have a greater concentration than

expected. For instance, for the 0.2% sprayed composite, if the volume fraction is actually 0.04 instead of 0.0013, the theoretical E' is 589 MPa. More sophisticated models such as the Paul [141], Counto [142], Takayanagi [143], and Guth [144] all give similar results when compared to the rule of mixtures employed here.

Figure 103 shows SEM images of the cross-sections for liquid nitrogen fractured surfaces of the neat, C60 1% sprayed, and C60 0.3% compounded 4 layer sandwich composites. The neat and 1% sprayed sandwich composites show similar fractured surfaces sowing wave-like fracture steps. The 0.3% compounded composite show a jagged surface indicating the C60 nanoparticles resist fracture. This is due to the fact that they are in the polymer matrix while the sprayed C60 is on the web surface. With C60 embedded in the polymer of the compounded composites, loading is transferred to the C60 and the composites respond with higher fracture toughness.
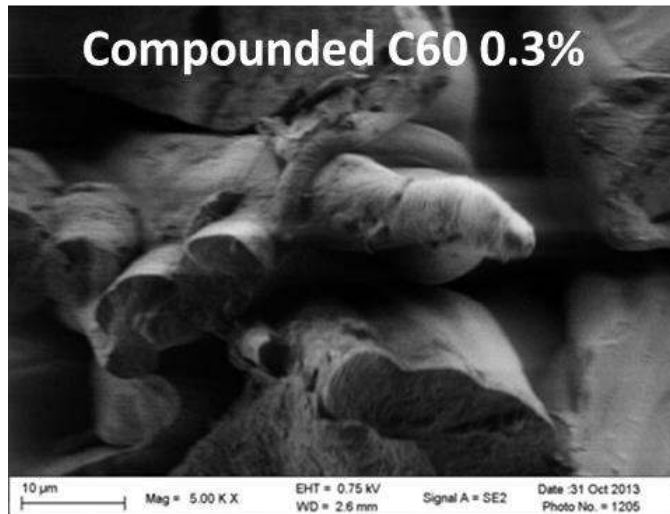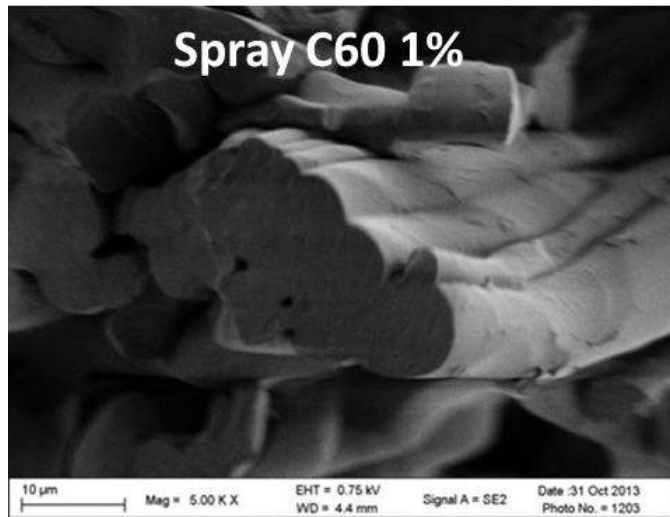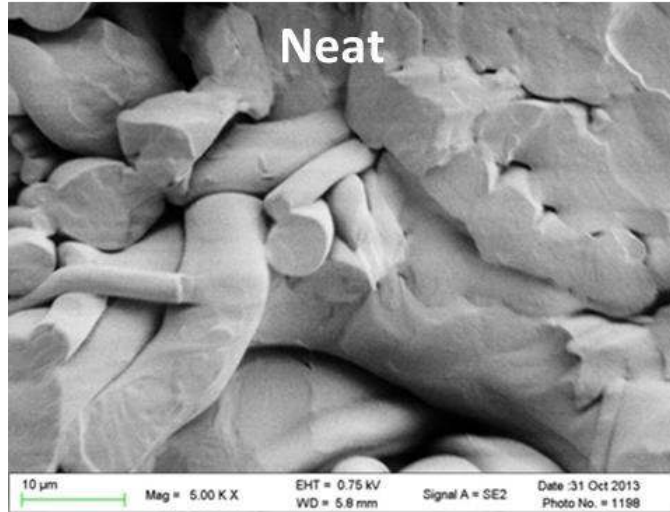
Figure 103. Cross-section of liquid nitrogen fractured samples.

5.5. High Frequency Response

Figure 104 shows the resonance (natural) frequencies of the materials tested for high frequency response with the mini-shaker. The 4 layer composites tested were the C60 spray samples (abbreviated SC followed by the add on wt% without the decimal) and the compounded C60 samples (CC followed by the add on wt% without the decimal). The control and Teflon which the samples were mounted on for support are also presented. All samples tested showed 4 resonant frequencies in similar frequency ranges. The 3rd and 4th modes are in the high frequency range of interest.
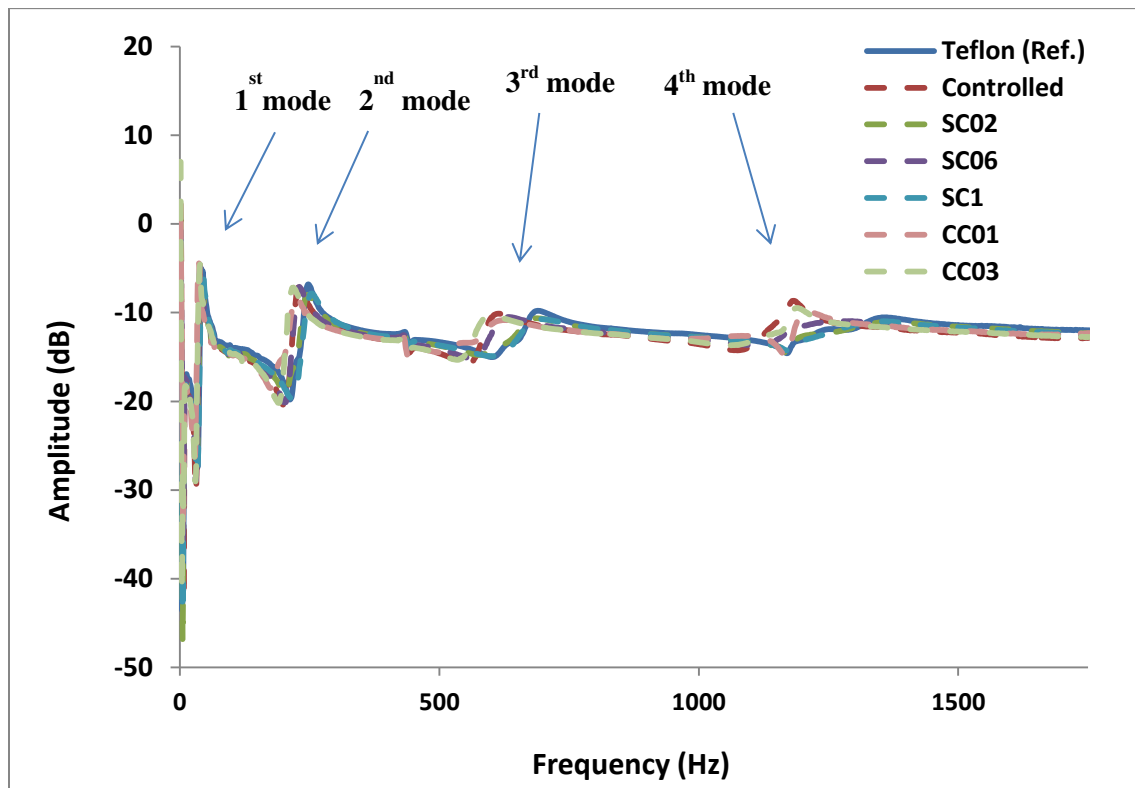
Figure 104. Frequency response curves

The damping ratio was calculated using the equation in Figure 53 for the four modes or natural frequencies shown in Figure 104. The peak frequency and corresponding damping ratio are presented in Table 14 for each sample. The data in Table 14 was used to plot the damping ratio as a function of frequency and is presented in Figure 105.

Table 14. Peak frequency and damping ratio for each mode.

Sample	Mode	Freq. (Hz)	Damping Ratio	Sample	Mode	Freq. (Hz)	Damping Ratio
Control	1	39	0.08	Teflon	1	41	0.11
	2	231	0.07		2	248	0.07
	3	614	0.29		3	690	0.29
	4	1183	0.09		4	1354	0.31
SC02	1	40	0.09	CC01	1	36	0.07
	2	246	0.11		2	224	0.12
	3	690	0.31		3	624	0.31
	4	1364	0.27		4	1211	0.21
SC06	1	39	0.06	CC03	1	39	0.06
	2	230	0.08		2	219	0.09
	3	634	0.35		3	593	0.37
	4	1300	0.26		4	1189	0.20
SC1	1	45	0.11				
	2	254	0.11				
	3	698	0.30				
	4	1346	0.27				
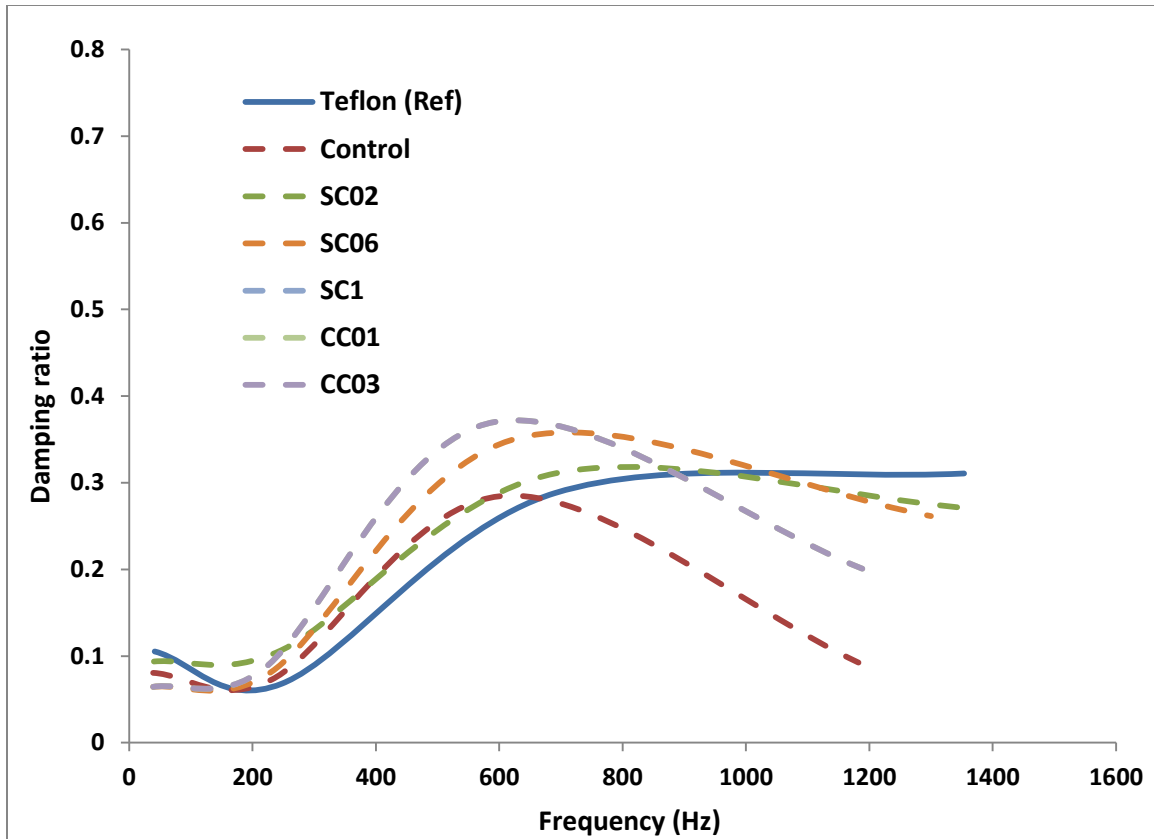
Figure 105. Damping Curves for 3rd mode

The 3rd mode of the materials shows the highest damping with the peaks of the different samples occurring between 600 and 700 Hz. It is clear that addition of the C60 nanoparticles increased damping over the control alone. Also, at the peak frequencies, the Teflon shows lower damping than the sandwich composites. Figure 106 shows the peak damping ratio for each sandwich composite at the 3rd (600 – 700 Hz) and 4th (1200 – 1350 Hz) modes. For the 3rd mode, the compounded 0.3% C60 sample has the highest damping ability at 0.37 over 0.29 of the control. This is contrast to the DMA results at lower frequencies. This is could arise due to the higher frequency engaging the C60 contracting and expanding action of its structure as the C60 may also resonate at this frequency range. This may not occur at the lower frequencies used in DMA. The E' and E" improvements in DMA are likely due to a reinforcing action of the C60, making the materials stiffer. These sandwich composites fabricated here show much higher damping

when compared to E-glass/Polyurethane foam sandwich composites tested on the same equipment by Vaidya [146]. In a similar frequency range, his highest damping material had a damping ratio of 0.007, which is 98% lower than what was observed for the 0.3% compounded composite here.

 At frequencies ranging from 1200 to 1340 Hz, the sprayed sandwich composites show higher damping ability than the compounded C60 composites. This indicates the materials response at higher frequencies is dominated by stiffness as the sprayed samples showed higher moduli in DMA testing. Vaidya also tested carbon-carbon composites and metal foam composites in this frequency range [147, 148]. The carbon-carbon composites showed similar damping ratios to what was observed here, however those materials possessed much greater stiffness. The metal foam composites had damping ratios ranging from 0.005 to 0.07.
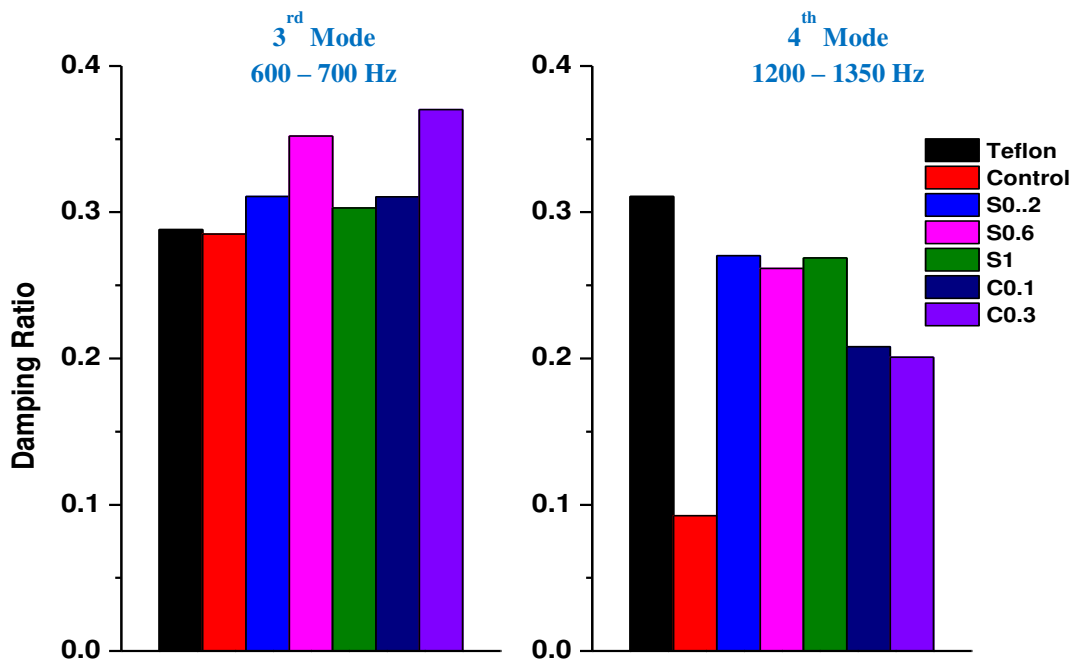
Figure 106. Damping of 3rd and 4th modes

CHAPTER 6: CONCLUSIONS

6.1: TPU Screening

Melt Blown TPU webs

Thermoplastic polyurethane polymers with aromatic based hard segments and ether or ester based soft segments with shore hardness ranging from 60D to 85A were melt blown into nonwoven microfiber webs. The webs were collected at multiple die-to-collector distances (DCD) and air pressures to analyze the changes in web structure and properties. Web strength at break was found to decrease with shore hardness while elongation at break increased with decreasing shore hardness. Ester based webs possessed greater strength due to a higher degree of hydrogen bonding and lower degree of phase separation [30]. Web strength and elongation at break decreased with increasing DCD while higher air pressure increased both. Web mechanical properties were found to be largely dependent on the degree of fiber-to-fiber bonding in the webs which decreases with increasing DCD due to the fibers being cooler once landing on the collection belt. At low DCDs, the fibers are close to the melt temperature and are able to form a high degree of fiber-to-fiber bonding points. The average fiber diameter of the S92A and T85A webs decreased with increasing air pressure while the S60D, T55D, and T92A webs showed very little change. The average pore size and air permeability were both found to increase with increasing DCD and decrease with increasing air pressure. At higher air pressure, the fibers travel at a faster rate to the collection belt and consequently, they are at a higher temperature and form a more consolidated web with greater fiber-to-fiber bonding. The shore hardness D polymers required high processing temperatures in order to prevent overheating of the extruder and consequently lost over 50% if the polymer intrinsic viscosity. The shore hardness 85A polymers were difficult to collect and exhibited low stiffness which would create difficulties in coating experiments.

150

Dynamic mechanical analysis temperature scans indicate the storage modulus increases with increasing shore hardness while the magnitude of tan delta decreases with increasing shore hardness. The glass transition was found to increase with shore hardness and frequency. In order to exploit the transition from rubber to glass phase at high velocity impact, a ether based soft segment TPU of 90A shore hardness was chosen. Its glass transition was found to be in the range of expected use temperature and its predicted glass transition also fell within the range of high frequencies associated with high velocity impacts. It also had the best processability of the polymers.

6.2: Nanoparticle Reinforced Sandwich Composites

Coated Sandwich Composites

The dip coating methods provided little to no improvement in storage and loss moduli of the sandwich composites at 1, 3, and 5 add on weight percent for nanoclay and C60. The continuous coating method over-saturated the webs and required high drying temperatures. Dispersion of the nanoclay was also poor with random aggregation. The individual dip coating with nanoclay and C60 had very poor dispersion of the nanoparticles. A high degree of aggregation and agglomerates were observed with SEM imaging.

The continuous spray coating with the Sono-Tek system was conducted with two trials. In trial 1, the concentration of the nanoparticle solutions was maintained while the volume flow rate and belt speed were changed to achieve the desired add on weight percent of nanoparticles. The webs had to be coated on both sides with half of the desired add on weight percent to achieve 1, 3, and 5% by weight add on. This was done to stay under the solubility limit of the nanoparticles in their respective solvent. Good improvements in storage and loss moduli were observed at C60 loadings of 1 and 3

percent by weight. The 5 wt% C60 loading had no improvement. SEM analysis showed good dispersion at the 1% add on level with some aggregation of the nanoparticles. Dispersion decreased and the degree of aggregation increased with increased loading. The POSS nanoparticles showed no improvement in moduli.

In trial two, the volume flow rate and belt speed were held constant while the nanoparticle solution concentration was changed to achieve the desired add on weight percent of nanoparticles. Add on weight percent of 0.2, 0.6, and 1 were investigated with C60, graphite, and tungsten disulfide inorganic nanotubes (INT). These lower percent's gave much higher improvements in the storage and loss moduli. A uniform dispersion was found at all 0.2% loadings. Aggregation and some non-uniform dispersion were observed with increased loading and some agglomerations were found at the 1% loading. The 0.2 wt% showed the greatest improvement for all the nanoparticles investigated. The 0.2 wt% C60 shows the largest improvement reaching an E' of 495 MPa. This is more than a 15 fold increase over the control, 30.6 MPa. The 0.2 wt% graphite improved to 177 MPa while the 0.2 wt% INT's E' was 78.8 MPa at 100 rad/s.

Compounded TPU/C60 Sandwich Composites

TPU/C60 blends were melt blown at loadings of 0.1 and 0.3 weight percent and fabricated into sandwich composites. The 0.3% composites showed 25% improvement in storage and loss moduli over the control. The 0.1% loading gave no improvement. The level of improvement of the 0.3% C60 compounded sandwich composite was found to be six times less than that of the 0.2% sprayed composite.

6.3: High Frequency Testing

All sandwich composites with C60 loading showed improved damping over the control. At the third resonant mode for the TPU where frequencies ranged between 600 and 700 Hz, the compounded 0.3% C60 composite showed the greatest damping ability with a

damping ratio of 0.37 compared to 0.29 for the control. At the fourth resonant mode with frequencies between 1200 to 1350 Hz, the sprayed composites showed greater damping ability than the compounded with the 0.6% composite having the greatest damping ratio at 0.26 while the control dropped to 0.09. In all cases, the damping ratios were more than an order of magnitude higher than those reported in literature for E-glass/polyurethane foams and metal composite foams [146, 148].

6.4: Overall Conclusions

This study has shown that one can produce flexible composite structures suitable for energy absorption by reinforcing polyurethane nonwoven webs with high strength and high modulus nanoparticles.   To determine the appropriate TPU for the application, a series of TPUs with different shore hardness were melt blown to investigate processability, web structure, mechanical, and thermal properties. It was determined that a TPU of 90A shore hardness was most suitable and possessed a glass transition in the ideal range to exploit the transition from rubber to glass phase to allow for large amounts of energy dissipation upon high velocity impact. The ultra-sonic spray coating method produced the most uniform dispersion of nanoparticles and greatest improvement in the dynamic mechanical properties of the reinforcement methods investigated. A high degree and quality of dispersion was obtained at the lowest add on weight percent of nanoparticles investigated, 0.2%, which consequently gave the greatest property improvement. Of the multiple nanoparticles used for reinforcement, C60 provided the greatest improvement in damping ability. With optimized spray coating parameters, the storage and loss moduli of the C60 reinforced sandwich composite at 0.2% by weight loading showed and improvement of 15 times over the control sample.

6.5: Recommendations for further work

- High Strain rate testing with a Split-Hopkinson Pressure Bar or similar high strain rate testing technique should be utilized to determine the sandwich composite response.
- Firearm or gas gun impact testing with the sandwich composites as a backing on traditional sacrificial armor such as Kevlar vest and hard ceramic plates to analyze the quantity of energy dissipated when the remaining energy of a ballistic impact is passed to the underlying sandwich composite.
- Further analysis on the sprayed sandwich composites to determine the exact mechanisms giving it greater dynamic properties when compared to the compounded composites at low strain rates.
- Investigations of increasing the number of layers or plies in the sandwich composites.

REFERENCES

155

1. Rubin Michael, Asymmetric Threat Concept and its Reflections on International Security, Strategic Research and Study Center (SAREM), Instanbul, May 31, 2007.

2. Kolodzie M.L., The Asymmetric Threat, www.almc.army.mil/……/MS628.htm

3. Okie, S. "Traumatic Brain Injury in the War Zone." The New England Journal of Medicine. 352.20 (2005): 2043-2047.

4. Moulton, J. "Rethinking IED Strategies: From Iraq to Afghanistan." Military Review. July-Aug (2009): 26-33.

5. Meyers, M. A. (1994). Dynamic behavior of materials. New York: Wiley.

6. Cooper, A. "Training for a Mission in an IED Threat Environment." Military Technology. 12 (2008): 68.

7. Improvised Explosive Devices (IEDs) – Iraq. 1 Nov 2005. Globalsecurity.org. 14 Apr 2009. http://www.globalsecurity.org/military/intro/ied-iraq.htm

8. "We will defeat the IED." Military Technology. 10 (2008): 20-27.

9. "Department of Defense Dictionary of Military and Associative Terms." Joint Armed Forces. 17 Oct 2008. http://www.dtic.mil/doctrine/jel/new_pubs/jp1_02.pdf

10. "Shockwave." Columbia Electronic Encyclopedia. 6th ed. 1 Jan 2009.

11. Eshel, D. "IED Blast related Brain Injuries: The silent killer." 2009. Defense Update, Online Holdings International. 21 Aug 2009. http://defense-update.com/analysis/analysis_270507_blast.htm

12. R. Lane, B. Craig, W. Babcock, "Materials for blast and penetration resistance", The AMPTIAC Quartely, 6(4), pp.39-45, 2002.

13. Agrawal, B. J. (2011). High performance textiles for ballistic protection. Defense Science Research Conference and Expo (DSR), 2011.

14. K.H. Taber, D.L. Warden, and R.A. Hurley, Blast-Related Traumatic Brain Injury: What Is Known?, J. Neuropsychiatry Clin. Neurosci., 2006, 18, p 141−145

15. Meyer, K. et al. "Severe and Penetrating Traumatic Brain Injury in the Context of War." Journal of Trauma Nursing. 15.4 (2008): 185-191.

16. Chafi, M. S., G. Karami, et al. (2010). "Biomechanical Assessment of Brain Dynamic Responses Due to Blast Pressure Waves." Annals of Biomedical Engineering 38(2): 490-504.

17. Ruff, R.L. et al. "Headaches among Operation Iraqi Freedom/Operation Enduring Freedom veterans with mild traumatic brain injury associated with exposure to explosions." Journal of Rehabilitation Research & Development. 45.7 (2008): 941-952.

18. Przekwas, A., Tan, X. G., Harrand, V., Reeves, D., Chen, Z. J., Sedberry, K., et al. (2011). "Integrated experimental and computational framework for the development and validation of blast wave brain biomechanics and helmet protection," in Proc. HFM-207 NATO Symposium on a Survey of Blast Injury Across the Full Landscape of Military Science (Halifax, NS).

19. Prat, N., F. Rongieras, et al. (2012). "Contemporary body armor: technical data, injuries, and limits." European Journal of Trauma and Emergency Surgery 38(2): 95-105.

20. Cheeseman, B. A. and T. A. Bogetti (2003). "Ballistic impact into fabric and compliant composite laminates." Composite Structures 61(1–2): 161-173.

21. Duan, Y., Keefe, M., Bogetti, T.A., and Powers, B., 2006. 'Finite element modeling of transverse impact on a ballistic fabric', International Journal of Mechanical Sciences, 48, pp 33-43.

22. F. Ko and A. Geshury, Textile Preforms for Composite Materials Processing, Advanced Materials and Processes Information Analysis Center, AMPT-19, August 2002

23. Orange. (n.d.). usmc-collectors. Retrieved August 12, 2013, from http://usmc-collectors.pagesperso-orange.fr/fichiers%20listes%20et%20divers/body%20armor.htmhttp://

24. Carey, M. E., M. Herz, et al. (2000). "Ballistic Helmets and Aspects of Their Design." Neurosurgery 47(3): 678-689.

25. Drobny, J. G. (2007). Handbook of thermoplastic elastomers. Norwich, NY: William Andrew Pub..

26. Harper, C. A. (1996). Handbook of plastics, elastomers, and composites (3rd ed.). New York: McGraw-Hill.

27. Holden, G. (1996). Thermoplastic elastomers (2nd ed.). Munich: Hanser Publishers ;.

28. Polymers and plastics: a chemical introduction. (n.d.). Steve Lower stuff. Retrieved August 12, 2013, from http://www.chem1.com/acad/webtext/states/polymers.html#PageTophttp://

29. Holden, G. (2000). Understanding thermoplastic elastomers. Munich: Hanser ;.

30. Prisacariu, C. (2011). Polyurethane elastomers from morphology to mechanical aspects. Wien: Springer.

31. Gu, X. and P. T. Mather (2012). "Entanglement-based shape memory polyurethanes: Synthesis and characterization." Polymer 53(25): 5924-5934.

32. Strength stress strain curve gallery. (n.d.). this pic.com. Retrieved August 12, 2013, from pics1.this-pic.com/key/%20strength%20stress%20strain%20curveh

33. Molded Dimensions - Engineered Elastomer Solutions to help you win!. (n.d.). Molded Rubber Part Molded Rubber Custom Molded Rubber Molded Rubber Product Molded Rubbers. Retrieved August 12, 2013, from http://www.moldeddimensions.com/stressstrain.htm

34. Yi, J., M. C. Boyce, et al. (2006). "Large deformation rate-dependent stress–strain behavior of polyurea and polyurethanes." Polymer 47(1): 319-329.

35. Heijboer, J. (1969). "Modulus and damping of polymers in relation to their structure." British Polymer Journal 1(1): 3-14.

36. Boyer, R. F. (1968). "Dependence of mechanical properties on molecular motion in polymers." Polymer Engineering & Science 8(3): 161-185.

37. Vincent, P. I. (1974). "Impact strength and mechanical losses in thermoplastics." Polymer 15(2): 111-116.

38. Roland, C. M. and R. Casalini (2007). "Effect of hydrostatic pressure on the viscoelastic response of polyurea." Polymer 48(19): 5747-5752.

39. Bogoslovov, R. B., C. M. Roland, et al. (2007). "Impact-induced glass transition in elastomeric coatings." Applied Physics Letters 90(22): 221910-221910-221913.

40. Roland, C. M., D. Fragiadakis, et al. (2010). "Elastomer–steel laminate armor." Composite Structures 92(5): 1059-1064.

41. Casalini, R., R. Bogoslovov, et al. (2012). "Nanofiller reinforcement of elastomeric polyurea." Polymer 53(6): 1282-1287.

42. Roland, C. M. (2012). "GLASS TRANSITION IN RUBBERY MATERIALS." Rubber Chemistry and Technology 85(3): 313-326.

43. Choi, T., D. Fragiadakis, et al. (2012). "Microstructure and Segmental Dynamics of Polyurea under Uniaxial Deformation." Macromolecules 45(8): 3581-3589.

44. Pathak, J. A.; Twigg, J. N.; Nugent, K. E.; Ho, D. L.; Lin, E. K.; Mott, P. H.; Robertson, C. G.; Vukmir, M. K.; Epps, T. H. III; Roland, C. M. Macromolecules 2008, 41, 7543−7548.

45. Fragiadakis, D.; Gamache, R.; Bogoslovov, R. B.; Roland, C. M. Polymer 2010, 51, 178−184.

46. Shim, J.; Mohr, D. Int. J. Impact Eng. 2009, 36, 1116−1127.

47. Sarva, S. S.; Deschanel, S.; Boyce, M. C.; Chen, W. Polymer 2007, 48, 2208−2213.

48. Xue, L.; Mock, W. Jr.; Belytschko, T. Mech. Mater. 2010, 42, 981−1003.

49. Davidson, J. S.; Fisher, J. W.; Hammons, M. I.; Porter, J. R.; Dinan, R. J. J. Struct. Eng.・ASCE 2005, 131, 1194−1205.

50. Jiao, T.; Clifton, R. J.; Grunschel, S. E. High strain rate response of an elastomer. In Shock Compression of Condensed Matter・2005, Parts 1 and 2; 2006; Vol. 845, pp 809−812.

51. Amirkhizi, A. V.; Isaacs, J.; McGee, J.; Nemat-Nasser, S. Philos. Mag. 2006, 86, 5847−5866.

52. Tekalur, S. A., A. Shukla, et al. (2008). "Blast resistance of polyurea based layered composite materials." Composite Structures 84(3): 271-281.

53. Grujicic, M., W. C. Bell, et al. (2010). "Blast-wave impact-mitigation capability of polyurea when used as helmet suspension-pad material." Materials & Design 31(9): 4050-4065.

54. Grujicic, M., B. Pandurangan, et al. (2010). "Computational investigation of impact energy absorption capability of polyurea coatings via deformation-induced glass transition." Materials Science and Engineering: A 527(29–30): 7741-7751.

55. Grujicic, M., R. Yavari, et al. (2012). "Molecular-level computational investigation of shock-wave mitigation capability of polyurea." Journal of Materials Science 47(23): 8197-8215.

56. Wente, V. A. (1956). "Superfine Thermoplastic Fibers." Industrial & Engineering Chemistry 48(8): 1342-1346.

57. Ellison, C. J., A. Phatak, et al. (2007). "Melt blown nanofibers: Fiber diameter distributions and onset of fiber breakup." Polymer 48(11): 3306-3316.

58. R.R. Breese, W. Ko, Fiber formation during melt blowing, Int. Nonwovens J. (2003).

59. Lee, Y. E. and L. C. Wadsworth, "Process Property Studies of Melt Blown Thermoplastic Polyurethane Polymers for Protective Apparel," International Nonwovens Journal, 2-9, Winter 2005.

60. Deniz Duran (2012). Investigation of the Physical Characteristics of Polypropylene Meltblown Nonwovens Under Varying Production Parameters, Thermoplastic Elastomers, Prof. Adel El-Sonbati (Ed.), ISBN: 978-953-51-0346-2, InTech, DOI: 10.5772/36798.

61. Batra, S. K., & Pourdeyhimi, B. (2012). Introduction to nonwovens technology. Lancaster, PA: Destech Publications.

62. Krutka, H. M., R. L. Shambaugh, et al. (2002). "Analysis of a Melt-Blowing Die: Comparison of CFD and Experiments." Industrial & Engineering Chemistry Research 41(20): 5125-5138.

63. Tate, B. D. and R. L. Shambaugh (2004). "Temperature Fields below Melt-Blowing Dies of Various Geometries." Industrial & Engineering Chemistry Research 43(17): 5405-5410.

64. Krutka, H. M., R. L. Shambaugh, et al. (2003). "Effects of Die Geometry on the Flow Field of the Melt-Blowing Process." Industrial & Engineering Chemistry Research 42(22): 5541-5553.

65. Krutka, H. M., R. L. Shambaugh, et al. (2004). "Effects of Temperature and Geometry on the Flow Field of the Melt Blowing Process." Industrial & Engineering Chemistry Research 43(15): 4199-4210.

66. Marla, V. T. and R. L. Shambaugh (2004). "Modeling of the Melt Blowing Performance of Slot Dies." Industrial & Engineering Chemistry Research 43(11): 2789-2797.

67. Shambaugh, B. R., D. V. Papavassiliou, et al. (2012). "Modifying Air Fields To Improve Melt Blowing." Industrial & Engineering Chemistry Research 51(8): 3472-3482.

68. Shambaugh, B. R., D. V. Papavassiliou, et al. (2011). "Next-Generation Modeling of Melt Blowing." Industrial & Engineering Chemistry Research 50(21): 12233-12245.

69. Sun, Y., Y. Zeng, et al. (2010). "Three-Dimensional Model of Whipping Motion in the Processing of Microfibers." Industrial & Engineering Chemistry Research 50(2): 1099-1109.

70. Xin, S. and X. Wang (2012). "Mechanism of Fiber Formation in Melt Blowing." Industrial & Engineering Chemistry Research 51(32): 10621-10628.

71. Tan, D. H., C. Zhou, et al. (2010). "Meltblown fibers: Influence of viscosity and elasticity on diameter distribution." Journal of Non-Newtonian Fluid Mechanics 165(15–16): 892-900.

72. Zhou, C., D. H. Tan, et al. (2011). "Modeling the melt blowing of viscoelastic materials." Chemical Engineering Science 66(18): 4172-4183.

73. Lee, Y. and L. C. Wadsworth (1990). "Structure and filtration properties of melt blown polypropylene webs." Polymer Engineering & Science 30(22): 1413-1419.

74. Lee, Y. and L. C. Wadsworth (1992). "Effects of melt-blowing process conditions on morphological and mechanical properties of polypropylene webs." Polymer 33(6): 1200-1209.

75. Bresee, R. R., & Qureshi, U. A. (2004). Influence of Processing Conditions on Melt Blown Web Structure. Part 1–DCD. International Nonwovens Journal, 13(1), 49-55.

76. Lee, Y. E. and L. C. Wadsworth (2007). "Fiber and web formation of melt-blown thermoplastic polyurethane polymers." Journal of Applied Polymer Science 105(6): 3724-3727.

77. Zapletalova, T., Michielsen, S., & Pourdeyhimi, B. (2006). Polyether based thermoplastic polyurethane melt blown nonwovens. J. of Engineered Fibers and Fabrics, 1(1), 62-72.

78. Begenir, A., S. Michielsen, et al. (2009). "Crystallization behavior of elastomeric block copolymers: Thermoplastic polyurethane and polyether-block-amide." Journal of Applied Polymer Science 111(3): 1246-1256.

79. Begenir, A., S. Michielsen, et al. (2009). "Melt-blowing thermoplastic polyurethane and polyether-block-amide elastomers: Effect of processing conditions and crystallization on web properties." Polymer Engineering & Science 49(7): 1340-1349.

80. Gazzola, William Horst, "Melt Blown Poly(lactic acid) for Application as a Tissue Engineering Scaffold. " Master's Thesis, University of Tennessee, 2012. http://trace.tennessee.edu/utk_gradthes/1379

81. Ya Liu, Bowen Cheng, et al. (2010). "Development and Filtration Performance of Polylactic Acid Meltblowns." Textile Research Journal 80(9): 771-779.

82. Chen, T., L. Li, et al. (2005). "Fiber diameter of polybutylene terephthalate melt-blown nonwovens." Journal of Applied Polymer Science 97(4): 1750-1752.

83. Bianchi, M., F. Scarpa, et al. (2008). "Stiffness and energy dissipation in polyurethane auxetic foams." Journal of Materials Science 43(17): 5851-5860.

84. Peleg, K. (1980). "Cushioning energy dissipation in foam polymers." Polymer Engineering & Science 20(11): 738-740.

85. Lutter, H. D., Leppkes, R., Horn, P., Decker, W., Haase, V., & Hinz, W. (1995). U.S. Patent No. 5,420,170. Washington, DC: U.S. Patent and Trademark Office.

86. Hager, S. L., Jividen, V. C., Triouleyre, S. P., & Joulak, F. (2002). U.S. Patent No. 6,391,935. Washington, DC: U.S. Patent and Trademark Office.

87. Johnson, G. G., Landin, D. T., Jung, M. A., & McCutcheon, J. W. (2001). U.S. Patent No. 6,251,493. Washington, DC: U.S. Patent and Trademark Office.

88. "Polyurethane Foams." SAE International. N.p., n.d. Web. 18 Nov. 2013. <http://www.sae.org/search/?authors=%28%22Peter%20Gansen%22%29

89. Mendelsohn, M. A., F. W. Navish, et al. (1985). "Characteristics of a Series of Energy-Absorbing Polyurethane Elastomers." Rubber Chemistry and Technology 58(5): 997-1013.

90. Yoon, K., J. Kim, et al. (2003). "Damping properties and transmission loss of polyurethane. II. PU layer and copolymer effect." Fibers and Polymers 4(2): 49-53.

91. ZHU Jin hua, YAO Shu ren (Naval Academy of Engineering, Wuhan 430033, China);Study of the Morphology and Dynamic Mechanical Properties of Polyurethane Elastomers; Polymeric Materials Science and Engineering, 2000-05

92. Wang Jianhua, Luo Chenlei (Institute of Chemical Materials, Advances in the Research of Polyurethane Damping Materials; Engineering Plastics Application;2002-10

93. Bilal Khan, M. (2010). "Intelligent Viscoelastic Polyurethane Intrinsic Nanocomposites." Metallurgical and Materials Transactions A 41(4): 876-880.

94. Hwang, G. L., Y. T. Shieh, et al. (2004). "Efficient Load Transfer to Polymer-Grafted Multiwalled Carbon Nanotubes in Polymer Composites." Advanced Functional Materials 14(5): 487-491.

95. Mackintosh, A.R. and Pethrick, R.A. and Banks, W.M. (2011) Dynamic characteristics and processing of fillers in polyurethane elastomers for vibration damping applications. Proceedings of the Institution of Mechanical Engineers, Part L: Journal of Materials: Design and Applications, 225 (3). pp. 113-122. ISSN 1464-4207

96. Xia, H. and M. Song (2005). "Preparation and characterization of polyurethane-carbon nanotube composites." Soft Matter 1(5): 386-394.

97. Tzong-Liu Wang, Chin-Chung Yu, Chien-Hsin Yang, Yeong-Tarng Shieh, Yu-Zen Tsai, and Na-Fu Wang, "Preparation, Characterization, and Properties of Polyurethane-Grafted Multiwalled Carbon Nanotubes and Derived Polyurethane Nanocomposites," Journal of Nanomaterials, vol. 2011, Article ID 814903, 9 pages, 2011. doi:10.1155/2011/814903

98. Chen, W., X. Tao, et al. (2006). "Carbon nanotube-reinforced polyurethane composite fibers." Composites Science and Technology 66(15): 3029-3034.

99. Khan, U., P. May, et al. (2010). "Development of stiff, strong, yet tough composites by the addition of solvent exfoliated graphene to polyurethane." Carbon 48(14): 4035-4041.

100. Pei, A., J.-M. Malho, et al. (2011). "Strong Nanocomposite Reinforcement Effects in Polyurethane Elastomer with Low Volume Fraction of Cellulose Nanocrystals." Macromolecules 44(11): 4422-4427.

101. Nunes, R. C. R., J. L. C. Fonseca, et al. (2000). "Polymer–filler interactions and mechanical properties of a polyurethane elastomer." Polymer Testing 19(1): 93-103

102. A. C. D. Newman, Chemistry of Clays and Clay Minerals, John Wiley & Sons, New York (1987).

103. B. K. G. Theng, The Chemistry of Clay-Organic Reactions, John Wiley & Sons, New York (1974).

104. P. C. LeBaron, Z. Wang, and T. J. Pinnavaia, Appl. Clay Sci., 15, 29 (1999).

105. Lee, K. Y. and L. A. Goettler (2004). "Structure-property relationships in polymer blend nanocomposites." Polymer Engineering & Science 44(6): 1103-1111.

106. M. R. Kamal; N. K. Borse; A. Garcia-Rejon. Polymer Engineering & Science 2002, 42, (9), 1883-1896.

107. Organoclays Nanoclay Additives for Reinforced Plastics. (n.d.). Organoclays Nanoclay Additives for Reinforced Plastics. Retrieved August 13, 2013, from http://www.nanoclay.com/

108. "SES Research." Fullerene. N.p., n.d. Web. 11 Aug. 2013. <https://sesres.com/>.

109. "Hybrid Plastics®: Nanostructured® POSS® Chemicals." Hybrid Plastics®. N.p., n.d. Web. 13 Aug. 2013. <http://www.hybridplastics.com/products/catalog.htm#acryl>.

110. "NanoMaterials." Polymer Applications. N.p., n.d. Web. 11 Aug. 2013. <www.apnano.com/http://>.

111. Menard, K. P. (2008). Dynamic mechanical analysis: a practical introduction. Boca Raton, Fla. [u.a.: CRC Press.

112. "Viscoelastic Damping." Roush Industries. N.p., n.d. Web. 1 Nov. 2013. <http://www.roush.com/Portals/1/Downloads/Articles/Insight.pdfFind a website by URL or keyword...>.

113. Brinson, H. F., & Brinson, L. C. (2008). Polymer engineering science and viscoelasticity: an introduction. Springer.

164

114. Gennes, P. (1979). Scaling concepts in polymer physics. Ithaca, N.Y.: Cornell University Press.

115. Doi, M., & Edwards, S. F. (1987). The theory of polymer dynamics. Oxford [Oxfordshire: Clarendon Press ;.

116. Ferry, J. D. (1980). Viscoelastic properties of polymers (3d ed.). New York: Wiley.

117. Flory, P. J. (1978). Principles of polymer chemistry (10. print. ed.). Ithaca, N.Y.: Cornell Univ. Pr..

118. Velankar, S. and S. L. Cooper (1999). "Microphase Separation and Rheological Properties of Polyurethane Melts. 2. Effect of Block Incompatibility on the Microstructure." Macromolecules 33(2): 382-394.

119. Speckhard, T. A., P. E. Gibson, et al. (1985). "Properties of polyisobutylene polyurethane block copolymers: 2. Macroglycols produced by the 'inifer' technique." Polymer 26(1): 55-69.

120. Velankar, S. and S. L. Cooper (1998). "Microphase Separation and Rheological Properties of Polyurethane Melts. 1. Effect of Block Length." Macromolecules 31(26): 9181-9192.

121. Van Bogart, J. W. C., D. A. Bluemke, et al. (1981). "Annealing-induced morphological changes in segmented elastomers." Polymer 22(10): 1428-1438.

122. Seymour, R. W. and S. L. Cooper (1973). "Thermal Analysis of Polyurethane Block Polymers." Macromolecules 6(1): 48-53.

123. Ng, H. N., Allegrezza, A. E., Seymour, R. W., & Cooper, S. L. (1973). Effect of segment size and polydispersity on the properties of polyurethane block polymers. Polymer, 14(6), 255-261.

124. Hu, W. and J. T. Koberstein (1994). "The effect of thermal annealing on the thermal properties and molecular weight of a segmented polyurethane copolymer." Journal of Polymer Science Part B: Polymer Physics 32(3): 437-446.

125. Koberstein, J. T. and L. M. Leung (1992). "Compression-molded polyurethane block copolymers. 2. Evaluation of microphase compositions." Macromolecules 25(23): 6205-6213.

126. Koberstein, J. T., A. F. Galambos, et al. (1992). "Compression-molded polyurethane block copolymers. 1. Microdomain morphology and thermomechanical properties." Macromolecules 25(23): 6195-6204.

127. Koberstein, J. T. and A. F. Galambos (1992). "Multiple melting in segmented polyurethane block copolymers." Macromolecules 25(21): 5618-5624.

128. Koberstein, J. T. and T. P. Russell (1986). "Simultaneous SAXS-DSC study of multiple endothermic behavior in polyether-based polyurethane block copolymers." Macromolecules 19(3): 714-720.

129. Leung, L. M. and J. T. Koberstein (1986). "DSC annealing study of microphase separation and multiple endothermic behavior in polyether-based polyurethane block copolymers." Macromolecules 19(3): 706-713.

130. Martin, D. J., G. F. Meijs, et al. (1999). "The influence of composition ratio on the morphology of biomedical polyurethanes." Journal of Applied Polymer Science 71(6): 937-952.

131. Martin, D. J., G. F. Meijs, et al. (1997). "The effect of average soft segment length on morphology and properties of a series of polyurethane elastomers. II. SAXS-DSC annealing study." Journal of Applied Polymer Science 64(4): 803-817.

132. Martin, D. J., G. F. Meijs, et al. (1996). "The effect of average soft segment length on morphology and properties of a series of polyurethane elastomers. I. Characterization of the series." Journal of Applied Polymer Science 62(9): 1377-1386.

133. Martin, D. J., G. F. Meijs, et al. (1996). "Effect of soft-segment CH2/O ratio on morphology and properties of a series of polyurethane elastomers." Journal of Applied Polymer Science 60(4): 557-571.

134. Chen, T. K., T. S. Shieh, et al. (1998). "Studies on the First DSC Endotherm of Polyurethane Hard Segment Based on 4,4'-Diphenylmethane Diisocyanate and 1,4-Butanediol." Macromolecules 31(4): 1312-1320.

135. Chen, T. K., J. Y. Chui, et al. (1997). "Glass Transition Behaviors of a Polyurethane Hard Segment based on 4,4'-Diisocyanatodiphenylmethane and 1,4-Butanediol and

the Calculation of Microdomain Composition." Macromolecules 30(17): 5068-5074.

136. Li, Y., T. Gao, et al. (1992). "Multiphase structure of a segmented polyurethane: effects of temperature and annealing." Macromolecules 25(26): 7365-7372.

137. Ryan, A. J., C. W. Macosko, et al. (1992). "Order-disorder transition in a block copolyurethane." Macromolecules 25(23): 6277-6283.

138. Chan, C.-M., J. Wu, et al. (2002). "Polypropylene/calcium carbonate nanocomposites." Polymer 43(10): 2981-2992.

139. Zhang, Q.-X., Z.-Z. Yu, et al. (2004). "Crystallization and impact energy of polypropylene/CaCO3 nanocomposites with nonionic modifier." Polymer 45(17): 5985-5994.

140. Nielsen, L. E. (1974). Mechanical properties of polymers and composites. New York: Dekker.

141. Paul, B.; Amer. Inst Mech Eng 1960, 36, 218.

142. Counto, U. J. Mag Concr Res 1964, 16, 129.

143. Takayanagi, M.; Uemura, S.; Minami, S. J Polym Sci Part: C 1964, 5, 113.

144. Guth, E. (1945). "Theory of Filler Reinforcement." Journal of Applied Physics 16(1): 20-25.

145. Lubrizol, Inc. (n.d.). Untitled Page. Retrieved November 18, 2013, from http://www.lubrizol.com/Engineered-Polymers/Products/Estane58000.html

146. A. S. Vaidya, N. Uddin, U. K. Vaidya: Vibration response of 3D space accessible sandwich composite, J. Reinf. Plas. and Compos. 28 (2009), pp. 1587–1599

147. Vaidya, U. K., P. K. Raju, et al. (1992). "Material damping studies on carbon-carbon composites." Carbon 30(6): 925-929.

148. Vaidya, U. K., S. Pillay, et al. (2006). "Impact and post-impact vibration response of protective metal foam composite sandwich plates." Materials Science and Engineering: A 428(1–2): 59-66.

Vita

Josh G. Fogle was born on February 14, 1979 in Orangeburg, South Carolina. He completed his undergraduate studies at Clemson University, SC earning a bachelor's degree in Ceramics and Materials Engineering in May of 2010. In the Fall of 2010, he joined the University of Tennessee, Knoxville as a graduate research assistant to pursue a PhD. in Polymer Engineering under the guidance of Dr. Gajanan Bhat.